Georgia State University

ScholarWorks @ Georgia State University

Physics and Astronomy Dissertations

Department of Physics and Astronomy

Fall 12-12-2022

Prediction of Space Weather Events using Solar Filaments and Sound waves as Precursors

Aparna Venkataramanasastry

Follow this and additional works at: https://scholarworks.gsu.edu/phy_astr_diss

Recommended Citation

Venkataramanasastry, Aparna, "Prediction of Space Weather Events using Solar Filaments and Sound waves as Precursors." Dissertation, Georgia State University, 2022.
doi: https://doi.org/10.57709/32630667

This Dissertation is brought to you for free and open access by the Department of Physics and Astronomy at ScholarWorks @ Georgia State University. It has been accepted for inclusion in Physics and Astronomy Dissertations by an authorized administrator of ScholarWorks @ Georgia State University. For more information, please contact scholarworks@gsu.edu.

Prediction of Space Weather Events using Solar Filaments and Sound waves as Precursors

by

V. Aparna

Under the Direction of Petrus C. Martens, PhD

A Dissertation Submitted in Partial Fulfillment of the Requirements of

Doctor of Philosophy

in the College of Arts and Sciences

Georgia State University

2022

ABSTRACT

This dissertation is an effort in adding to existing methods of predictive capability for space weather events such as coronal mass ejections (CMEs) and solar flares and to predict if these events will cause a geo-magnetic storm well in advance. I use solar observational features – filaments and sigmoids, and atmospheric helioseismology - as tools to identify if CMEs will cause disturbances in the magnetosphere, and when a solar flare might occur, respectively. The main elements of this dissertation are as follows.

First, I study the relation between axial field directions of filaments on the Sun to that of their interplanetary CME (ICME) counterparts near Earth. Filaments are plasma fibrils aligned along local magnetic fields and always form over polarity inversion lines. These features often erupt as CMEs and filament material have been observed in CMEs. I show, using an analysis of about two solar cycle filaments and ICME data, that the magnetic orientation of the filament in a CME is retained during its traversal of interplanetary space. I find that for solar cycle 23 and 24, the field orientation is retained 85% and 65% of the times, respectively.

Second, I compare chiralities of filaments associated with their X-ray sigmoid counterparts to identify if there is consistency between the two. Non-linear force-free field surface calculations are performed using vector-magnetograms to compare the calculated helicity sign of sigmoids with that of the observed signs of filaments and the handedness of sigmoids. I find that the sigmoids for which the signs from the three modalities do not match, produce 3.5 times as many flares as that when they do match.

Third, I use Magneto-Optical filters at Two Heights (MOTH) Dopplergrams in KI and Na-D2 lines with continuous observations of the Sun covering non-flaring and flaring times. Using Fourier cross-correlation and phase-difference techniques, I observe changes in travel-time for waves close to the acoustic cut-off frequency. At 6.5mHz frequency, large travel-time deviations from the mean, almost 3-15 hours prior to the occurrence of flares are observed.

The results suggest that the methods utilized in this work have a potential in improving space weather predictions.

INDEX WORDS: Solar Filaments, Coronal Mass Ejections, Solar Flares, Interplanetary Magnetic Field, Sigmoids, Chirality, Helioseismology, Acoustic Oscillations, Magnetic Fields.

Copyright by
V. Aparna
2022

Prediction of Space Weather Events using Solar Filaments and Sound waves as Precursors

by

V. Aparna

Committee Chair:	Petrus C. Martens
Committee:	Stuart M. Jefferies
	Manolis K. Georgoulis
	Valentin M. Pillet

Electronic Version Approved:

Office of Graduate Studies

College of Arts and Sciences

Georgia State University

December 2022

DEDICATION

This thesis is dedicated to Sara Martin, Helio Research, La Crescenta, CA.

ACKNOWLEDGEMENTS

It has been quite a winding journey since pink and grey colorful circular patches appeared in the sky that evening when I was a kid playing outside in Kolar Gold Fields (KGF), India (12.96°N,78.27°E), to studying space weather effects. The year was 1989, the same year the Quebec blackout occurred and possibly was also responsible for the color patches in the sky that evening.

It has also been quite a journey from being wait-listed to being accepted for graduate school at GSU. There has been struggle, doubts, helplessness, and often self implicated misleading hopes. There have also been achievements and sweet moments. Through all of these moments, there have been some constants in my life that have been greatly kind, helpful, and supportive. Dr. Caroline Roberts, my first AstroPal mentor in Astronomy took good care of me during my initial days when I was still figuring out the whats and whens. And to this day, she has been a pillar of support in this journey. Friday 12PM Group led by Dr. Shirley Chancey from the Counseling & Testing Center and all the group members have been greatly helpful in knowing myself better and healing me.

My advisors, Drs. Piet Martens and Stuart Jefferies have immensely contributed to my learning, writing better, and conducting better analysis. Dr. Manolis Georgoulis has been immensely helpful in helping me with the Sigmoids work. I thank Piet, Stuart, Manolis, and Dr. Valentin Pillet (NSO) for serving on my committee and carefully reading my dissertation, and giving me useful comments and suggestions. I also like to thank the Department of Astronomy & Physics for the computer hardware and the team for maintaining them even during outages. I am thankful to the faculty in both Astronomy and Physics sides of the department, for their support and confidence in my work during coursework. I acknowledge Drs. Russel White, Sebastien Lepine, Douglas Gies, Mike Crenshaw, Todd Henry, Jane Pratt and Fabien Baron from the Astronomy side and Dr. Xiaochun

He and late Drs. Nikolaus Dietz and Mark Stockman, from the Physics side, for I have immensely benefited from each of them in not only the courses but in their teaching methods, life experiences and their general temperament towards science and polity. I am thankful to Felicia Watts and her team for always helping with the logistics and timely reimbursements.

I am extremely grateful to my colleagues in India, Dr. Durgesh Tripathi for giving me an opportunity to learn from him. Drs. Sherry Chhabra, Girjesh Gupta, Pradeep Kayshap have all been dearly kind whenever I had any doubts regarding data processing or concepts.

I am extremely thankful to the solar community at large which is unbelievably helpful and active in getting whatever the students need. The numerous summer schools that they have conducted, student-friendly conferences, and meetings, all have contributed to my overall growth as a scientist as well as a person. I am thankful to the organizers of the CISM Space Weather Summer School, Heliophysics Summer School, Spectropolarimetry School, and the SHINE conference and for all their support.

Sara Martin was one of my first mentors that initiated me into solar astronomy. She has been a rock of a role model in how she conducts her day-to-day activities, her health, work, etc. It has been very inspiring interacting with her and knowing her all these years. I am firstly thankful for the internship opportunity that lead me to where I am now. In addition, I thank her for being open to sharing the data that HelioResearch has obtained so far, for research purposes. I thank her for also flying across the continent to come support me at me my dissertation defense.

I thank my friends in GSU, who have extended unequivocal support in different ways at different times. Caroline, Dr. Alex Yep, Shawn Reagin, Sumanth Rotti and Varun Chaturmutha have all been supportive with reviewing my chapters, bringing me soup, resolving doubts, and generally having a ear. I thank Alex and Caleb for helping me with formatting the dissertation.

This would not have been possible without the unequivocal support of my shoulder to rest, my husband, Krishna Kumar and my baby cat Pawndy. Pawndy came into our lives after my qualifier exams and she has brought about a change in me that I didn't think was possible. There are no words that can express everything that Krishna has done for me over all this time and I am very

grateful and thankful to him. I also acknowledge Dr. Vana Prasad whose support in the past years has meant that I am able to reach the finish line. I am also grateful to my parents for supporting me in this journey even though I am so far away.

- The work presented in Chapter 2 has been published as “Solar filaments and Interplanetary Magnetic Field Bz" in The Astrophysical Journal, Volume 897, Issue 68 (Aparna & Martens, 2020) and I acknowledge the following.

  H-alpha data were provided by the Kanzelhohe Observatory, University of Graz, Austria and the National Solar Observatory (NSO) Global Oscillations Network Group (GONG). We are grateful to them and to J.H. King and N. Papatashvilli of Adnet Systems, NASA GSFC and CDAWeb for providing the interplanetary plasma data. I thank OMNIWeb for their effort in creating a database for such parameters. I thank the ACE instrument team and the ACE Science Center for providing the ACE data. This work was supported by NASA grants, NNX15AF39G and NNX15AQ61G S004-05-07-2019. I thank the CDAW team for putting together the CME and Halo-CME database and providing it online.

- The work presented in Chapter 3 has been published as “Using CME Progenitors to Assess CME Geoeffectiveness" in The Astrophysical Journal, Volume 257, Issue 33 (Mundra et al., 2021) and I acknowledge the following.

  I heartily thank the anonymous referee for their critical analysis and useful comments that has lead to the betterment of the manuscript. I would like to thank the CDAW team for providing the CME and Halo-CME list on their website, without which this research would not have been possible. I thank OMNIWeb for their effort in creating a common database with data from various spacecrafts. I thank the ACE instrument team and the ACE Science Center for providing the ACE data. I also extend our thanks to the SOHO/MDI and the EIT consortia for the data. SOHO is a project of international cooperation between ESA and NASA. Kanzelhöhe Observatory (KSO), from University of Graz, Austria and the Big Bear Solar Observatory (BBSO) provided the Hα data. BBSO operation is supported by NJIT and

US NSF AGS-1821294 grant. I am also grateful to J.H. King and N. Papatashvilli of Adnet Systems, NASA GSFC and CDAWeb for providing the interplanetary plasma data. This work was supported by NASA grants NNX15AQ61G S004-05-07-2019 and 80NSSC19K1437. I was supported through the NASA FINESST grant 80NSSC19K1437 and acknowledge it.

- I acknowledge using GONG, KSO, MDI, HMI, and Hinode XRT data and thank the teams for curating the data and making them available for use. I also thank Manolis for sharing the ENHEL code used for analysis in Chapter 4 and willing to resolve any related and other doubts.

- I acknowledge using GONG, MDI magnetograms and MOTH data for the analysis in Chapter 5. I would like to thank Stuart and his team at the South Pole Station for obtaining the data.

I acknowledge NASA FINESST (grant #80NSSC19K1437) for supporting me through stipend, travel funds, computer hardware and journal publications between 2019 and now. I also acknowledge Georgia State University's Second Century Initiative (2CI) in supporting me during the first three years of graduate school. I would like also like to acknowledge the National Solar Observatory DKIST ambassador matching funds program.

The second publication mentioned above was conducted in collaboration with Kashvi Mundra, a high school student at the time seeking scientific projects. I thank Piet for trusting me to train Kashvi, and I thank Kashvi for willing to learn with me and conduct the analysis, which fruitfully lead to the journal article.

It is without a doubt that Deborah Gulledge, my fellow dissertation writer has been a wealth of support in the process of writing this document and I thank her for being there and giving me wise suggestions that helped me immensely through this time.

Finally, I acknowledge myself for wanting to do something in astronomy, taking the step to do it, coming this far and learning all along the way. The universe has a way of bringing one closer to oneself; it has indeed, in more than just one way and I couldn't have been more happier doing anything else. The journey continues...

TABLE OF CONTENTS

LIST OF TABLES

LIST OF FIGURES

LIST OF ABBREVIATIONS

Abbreviation	Description
ACE	Advanced Composition Explorer
AR	Active Region
BBSO	Big Bear Solar Observatory
CCD	Charged Coupled Device
CCMC	Community Coordinated Modeling Center
CDAW	Coordinated Data Analysis Workshop
CEA	Cylindrical Equal Area
CIR	Co-rotating Interacting Regions
CME	Coronal Mass Ejections
DKIST	Daniel K. Inouye Solar Telescope
Dst	Disturbance storm-time
EH	Energy-Helicity
EIT	Extreme-ultraviolet Imaging Telescope
ETT	Evolution of Travel-Time
EUV	Extreme Ultra-Violet
FLARECAST	Flare Likelihood and Region Eruption Forecasting
FFT	Fast Fourier Transform
FINESST	Future Investigators in NASA Earth and Space Science and Technology
GIC	Geomagnetic Induced Current

Abbreviation	Description
GOES	Geostationary Operational Environmental Satellite
GONG	Global Oscillations Network Group
GSE	Geocentric Solar Ecliptic
GST	Goode Solar Telescope
HMI	Helioseismic Magnetic Imager
HSP	HemiSpheric Preference
ICME	Interplanetary Coronal Mass Ejections
IMF	Interplanetary Magnetic Field
IRIS	Interface Region Imaging Spectrograph
ISS	International Space Station
KSO	Kanzelhöhe Solar Observatory
LASCO	Large Angle and Spectrometric Coronagraph
LOS	line-of-sight
MC	Magnetic Clouds
MHD	Magneto-Hydro-Dynamics
ML	Machine Learning
MDI	Michelson Doppler Imager
MOF	Magneto-Optical Filters
MOTH	Magneto Optical filters at Two Heights
MPA	Measurement Position Angle
NASA	National Aeronautics and Space Administration
NICT	National Institute of Information and Communications Technology
NLFF	Non-Linear Force Free
NLFFF	Non-Linear Force Free Field
NOAA	National Oceanic and Atmospheric Administration

Abbreviation	Description
NSO	National Solar Observatory
PIL	Polarity Inversion Line
PSP	Parker Solar Probe
PTT	Phase Travel-Time
SDO	Solar Dynamics Observatory
SEP	Solar Energetic Particles
SHARP	Space-Weather HMI Active Region Patch
SIDC	Solar Influences Data Analysis Center
SOHO	Solar and Heliospheric Observatory
SolO	Solar Orbiter
SWEPAM	Solar Wind Electron Proton and Alpha Monitor
SWORM	Space Weather Operations, Research and Mitigation
SWPC	Space Weather Prediction Center
TTF	Travel-Time against Frequency
UV	Ultra-Violet

Chapter 1

INTRODUCTION

The Sun plays the most important role in the lives of terrestrial and most oceanic organisms on Earth. The evolution from simple celled organisms to complex brained primates would not have been possible if there was no Sun. Hence, obviously it has been the most worshipped in several ancient cultures such as the Pharonics, Taoism, Aztec, Mayan and Vedic Hinduism. Today, we worship the Sun for similar reasons but unlike the ancient civilizations, we know the reason why we are afraid of the Sun - the high energy particles and the large magnetic structures that can disrupt the most essential organization for the day-today functioning of our society, the established technological and economic structure. It can also damage living tissues and cells.

Exploration is intrinsic to human character and so is space exploration. Humans have been continuously present in space since the 1990s first with the Mir Space Station and then the International Space Station since 2010. Future human missions to the Moon and Mars are already being planned with a target year of 2030. Travel to Mars can be as long as six months at a time and the astronauts and the electronics of the spacecraft must be protected from the harmful radiation in space due to high-energy solar activities such as solar flares and coronal mass ejections (CMEs). Solar flares potentially stream high energy protons via open magnetic field lines connected on one end to the Sun. These particles can interact with the genetic material in the cells to cause cancerous mutations or damage them leading to other diseases. High energy particles from the Sun can damage satellite electronics by ionizing the electrons in the circuits and shorting them. Such damages can sometimes cause significant changes to satellite attitude and control. For example, two Canadian telecommunication satellites Anik E1 and E2 lost altitude due to an increase in the

electron fluxes that caused an electrostatic discharge in the onboard electronics in early 1994 (Lam et al., 2012). Several districts in the state of Ontario lost telephone and television services for a few days and millions of dollars loss to the Telesat company that owned the uninsured satellites (Howell & Whalen, 2015). More recently, a CME which arrived at Earth on Feb 2, 2022, just before the launch of SpaceX's StarLink satellites[1] caused 40 of the 49 satellites to burn up in the atmosphere post launch. The CME had caused the upper atmosphere to heat and expand, which increased the atmospheric drag. The satellites failed to switch out of safe-mode to raise their orbits in time because the atmospheric drag was high[2].

CMEs can cause ground level damage as well. CME magnetic field compresses the Earth's magnetosphere which induces current (Geomagnetically Induced Currents or GICs) in oil pipelines causing them to rust prematurely and in electric grids by overloading the transformers. The March 1989 blackout incident is infamous for the electric grid overload and the power surge it caused in Quebec, Canada and parts of New York, New Jersey and North Dakota. A complete review of the incident from a current perspective is given by Boteler (2019).

As pointed out, the above effects majorly concern the health of space travellers, the economic hazards on the ground and the daily functioning of institutions and homes that depend on modern technology. These effects can be minimized to an extent by keeping a watchful eye on the Sun so that in case of solar flares, particle events or a CME, we can be prepared and if an event as strong as the Quebec event occurs, the electric grids can be shut down to prevent power surges and the cascade effect to other grids and switch the satellites into safe-mode so that no spurious currents are generated along the onboard circuitry.

A vast amount of effort has been put into continuous monitoring of the Sun. Most of this effort is space-based using satellites like SOHO, SDO, Hinode, GOES and IRIS, and monitoring the space environment near the Earth with ACE, WIND etc at the L1 Lagrangian point (see abbreviations page for acronyms). SOHO with its LASCO instrument monitors CMEs, SDO images the Sun at high cadence in nine extreme-ultra violet wavelengths (EUV) and also takes EUV spectra along

[1] www.starlink.com/

[2] https://www.space.com/spacex-starlink-satellites-lost-geomagnetic-storm

with measuring the surface magnetic field at the photosphere. Xray and EUV images have acted as a pivotal modality since the historical Spacelab, in understanding the physical phenomena responsible for the occurrence of flares and CMEs and the study of small scale features such as spicules that are thought to play a significant role in heating the corona (Shetye et al., 2016). CMEs and the X-ray features called sigmoids were first observed through the Skylab mission (Vaiana et al., 1973; MacQueen et al., 1980; Webb & Howard, 2012). CMEs were first speculated to be associated with space weather phenomena in as early as 1876 during the Carrington event (Carrington, 1859) where Richard Carrington had recorded large sunspots a few hours before observing a white-light flare. About 17 hours later, there were indications of a geomagnetic storm with induced currents along telegraph lines and spurious messages sent across continents without anybody initiating them, and Aurora Borealis were recorded to have been observed in latitudes as low as Cuba.

A modern day Carrington event is expected to cause an economic damage of 1.6 ± 1 trillion United States Dollars (USD) in just the US[3]. In order to protect space-based instruments, ground based electric and computer networks and a smooth functioning of the society, it is essential that effective prediction and forecasting mechanisms for these events be in place. One of the goals of the Heliophysics Division of NASA's Science Mission Directorate is to "develop knowledge and capability to detect and predict extreme conditions in space to protect life and society and to safeguard human and robotic explorers beyond Earth". To this end, the US government has appointed task forces that established the working group for Space Weather Operations, Research and Mitigation (SWORM) in 2019.

This dissertation work is a humble attempt to contribute to and improve the existing methods of space weather forecasting. Most common of the existing methods include empirical based models using past data as well as models based on numerical simulations. There are several models from all across the world and are in practice today, some of the standard ones being NOAA[4]/ SWPC's[5] lookup table method, SIDC[6] by creating a daily probabilistic forecast based using the McIntosh

[3]https://www.space.com/the-carrington-event
[4]National Oceanic and Atmospheric Administration
[5]Spaace Weather Prediction Center
[6]Solar Influence Data Analysis Centre of the Royal Observatory of Belgium

sunspot group classification method (McIntosh, 1990) and Japan's NICT[7](Kubo et al., 2017), etc. Most of these methods give a one hour warning ahead of the flare.

Recently, machine learning (ML) is rampant in every field starting from most commonly used in face detection to detect defects in 3D printing[8]. ML is gaining popularity in solar astrophysics as well. Particularly with the amount of data that is produced in the field of solar physics, it is one of the necessary ways to programmatically conduct analysis of huge sets of data. With the incorporation of ML into solar physics, there have been many novel flare-forecasting methods using algorithms such as decision trees and random forest; some of these are implemented using vector magnetograms (see Alipour et al. 2019 and references therein). A detailed comparison of these and several other methods are given in Leka et al. (2019). The effectiveness of the models is measured with a quantity known as the true skill score which ranges between 0.53 to 0.80 for 24 hour predictions for different methods from different authors they have provided (Krista & Chih, 2021), where 1.0 denotes a perfect prediction and 0.0 a totally random one.

Some forecasting efforts utilize in-situ data of CMEs collected by satellites and/ or use them in models to predict such events by applying to near-Sun and near-Earth measurements (Temmer, 2021). Some of these models forecast CME and SEP (Solar Energetic Particles) arrival times. Among the CME arrival prediction ones, there are drag based models and the shock time of arrival and WSA-ENLIL Cone Model that predict the arrival of CMEs and CME shocks, respectively (Riley et al., 2018). There are several other models with variations of these and their summaries are available on the CCMC's CME scoreboard website[9]. The average accuracy for forecast lead-time for CMEs is about ± 10 hours with the most accurate shock arrival time of ± 1 hour (Riley et al., 2018). Some projects such as FLARECAST (Georgoulis et al., 2021) are used for studying the evolution of solar surface magnetic field, active regions in particular, to predict solar flares and SEPs. A detailed review of SEP models is given in Whitman et al. (2022).

[7]National Institute of Information and Communications Technology
[8]https://tinyurl.com/yvadw9kv
[9]https://kauai.ccmc.gsfc.nasa.gov/CMEscoreboard/

This disseration work has been conducted on the topics that are thought to provide some level of addition to existing predictive capabilities and to improve forecast lead times. The thesis is mainly divided into two sections. The first section consisting of Chapter 2, 3 and 4 analyses the information from features such as Hα filaments and X-ray sigmoids on the Sun and in-situ measurements of magnetic-fields and plasma properties in the space near-Earth to do space weather predictions. Chapter 5 performs phase travel-time analysis of p-mode acoustic waves using Doppler measurements of active regions to predict the occurrence of solar flares.

These topics of predictive capabilities based on solar features and acoustic oscillations in the Sun converge under the common umbrella of space-weather predictions. While the former helps predict if CMEs have the configuration that can induce damage to the Earth's magnetosphere and hence affect our technological systems, the latter helps predict solar flares to protect satellites and astronauts from radiation. Here, I first give a broad introduction of the solar features - filaments and sigmoids that I am using in this work, followed by an introduction to solar acoustic oscillations. Each of these features are adapted into a project and presented in Chapters following this introduction. More relevant details about the projects and background is given at the beginning of each chapter.

1.1 Chromospheric Filaments

Filaments are of interest and are widely studied because they are magnetic structures often erupting into CMEs causing space weather events. They are called as filaments when observed on the disk where they are seen as photon absorbing features and prominences when they are observed above the limb where they are seen as photon emitting features. Historically, ground based observations of filaments have been in chromospheric wavelengths - $H\alpha$ (6563.8 Å), Ca II H (3968.5 Å), He I (10830 Å) and He I D3 (5876 Å) and hence are often called chromospheric filaments although they are known to be situated at coronal heights in limb observations. Thus, filaments are cool plasma suspended in magnetic structures at coronal heights. They are also seen as absorption features in Ultraviolet (UV) and extreme ultraviolet (EUV) wavelengths such as Lyα (912Å), He I (304Å), Fe I 171Å etc. In all these wavelengths, filaments are seen to contain mainly a long spine from which

leg-like extensions called barbs arise and end in the chromosphere, along with two end points where they are rooted on the solar surface. High resolution images of filaments show that the spine and barbs contain long and thin hair like strands containing plasma. Figure 1.1 shows a high resolution filament that shows the strands that make the filament body and barbs. The plasma in the strands is observed to be moving in and out of the filament body along these structures that are thought to be aligned with the local magnetic field. When the positions of filaments are observed over photospheric magnetograms, they are always seen to be formed over polarity inversion lines (PIL), the regions where opposite polarities are adjacent to each other.

Filaments are categorized as quiescent, active region and intermediate (Martin, 1998b). Quiescent filaments dwell in quiet regions of the Sun with magnetic fields not exceeding $\sim$30 G; active region filaments are seen in strong magnetic field regions; and intermediate filaments are seen with one end rooted in an active region and the other in the quiet Sun. Filaments are normally about 60 to 600 Mm long. Quiescent filaments tend to be longer (Kuckein et al., 2016) and long lasting compared to active region filaments. An example of a long filament is shown in Fig 1.2 and its corresponding magnetogram is given next to it to show the filament location with respect to the positive and negative polarities. The image of the filament also shows barb like extensions from the spine and the filament endpoints. These features are relatively easily observed in quiescent filaments as they are relatively large compared to active region filaments which are thin and short and usually do not show barbs (see Fig 1.1). Intermediate filaments are similar to quiescent filaments in that they show barb features.

The prominence material is supported against gravity via the Lorentz force and usually contains a winding or twisted magnetic field surrounding it called as a flux-rope and an overlying arcade system above it (Mackay et al. 2010 & references therein). An example is shown in Fig. 1.3. The shaded portion is the filament residing in the flux rope represented as ovals around the filament, and an overlying arcade of magnetic field that plays the role of stabilising the underlying flux rope. Another popular prominence support system is the sheared arcade configuration wherein the plasma near the PIL undergoes shear due to footpoint motions in opposite directions on either side of the

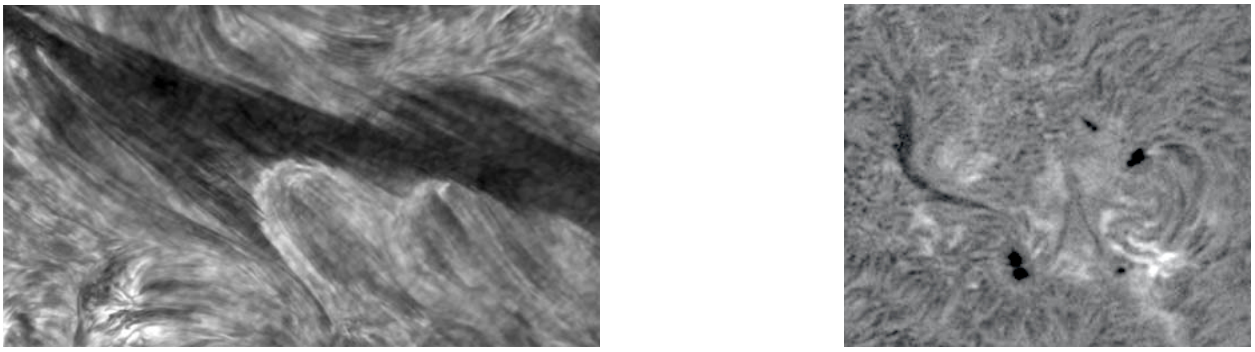

Figure 1.1: High resolution quiescent filament showing thin plasma structures (left). The image has been adapted from Lin et al. (2005). The image on the right is a GONG Hα image showing an active region filament.

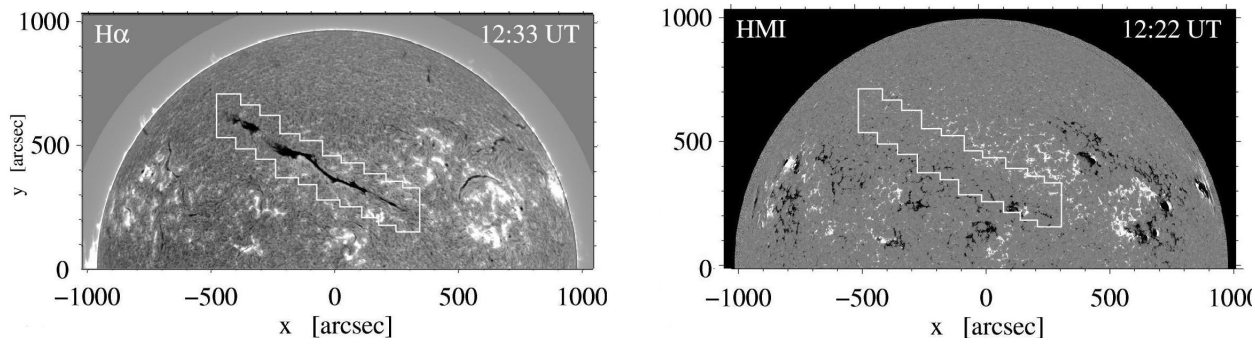

Figure 1.2: An example of quiescent filament (left) and corresponding magnetic polarities (right). The images have been adapted from Kuckein et al. (2016).

PIL. As shear increases, the field lines get elongated and form dips to help contain the prominence material. In the flux rope model, the arcade and the flux ropes are independent magnetic systems and in the sheared arcade case, there is one flux system (Mackay et al. 2010 & references therein). Processes such as energy accumulation (and other complex phenomena) often disturb the stability due to the magnetic tension from the overlying arcade field and filaments get ejected out of the solar corona into the interplanetary space, and are called Coronal Mass Ejections (CMEs). Figure 1.3 shows the structure of the magnetic field just before a CME occurs; the structure can be divided into three parts containing the filament, flux rope which is depicted as cavity in coronal limb images, and the bright front which is the overlying arcade field. In contrast to the above two models wherein prominence is supported by dips of field lines, Martin & Echols (1994) suggested that prominences are non-static and do not need dips to support the cool material, but the plasma along the field lines are continuously moving and hence do not collapse under gravity.

The CME after ejection can interact with other magnetized bodies in the solar system such as the magnetospheres of Earth and Jupiter and cause beautiful Auroras seen commonly in places beyond the Arctic and the Antarctic circles on Earth. It also causes disturbances in the magnetosphere that gives rise to geomagnetic storms when the magnetic configuration is right. The Earth's magnetic field points North-South starting from the geographical South-North. Whenever a CME magnetic field is pointing southward, it can reconnect with the Earth's magnetic field to cause geomagnetic storms. The structure of the CME that interacts with the magnetosphere is the flux rope with the filament in its axis. Flux ropes are hardly observed on the Sun because they don't contain dense plasma and are only seen in EUV wavelengths when they are hot, just before an eruption (Joshi et al., 2014). Filaments are easily observed and are part of the three-part flux rope configuration of CMEs, so the axial field direction of the flux rope is readily obtained by observing the filaments on the Sun. I utilize these concepts and on-disk filament observations to understand CME magnetic field directions to predict if a CME from a filament will affect the Earth's magnetosphere. The related work is presented in Chapters 2 and 3.

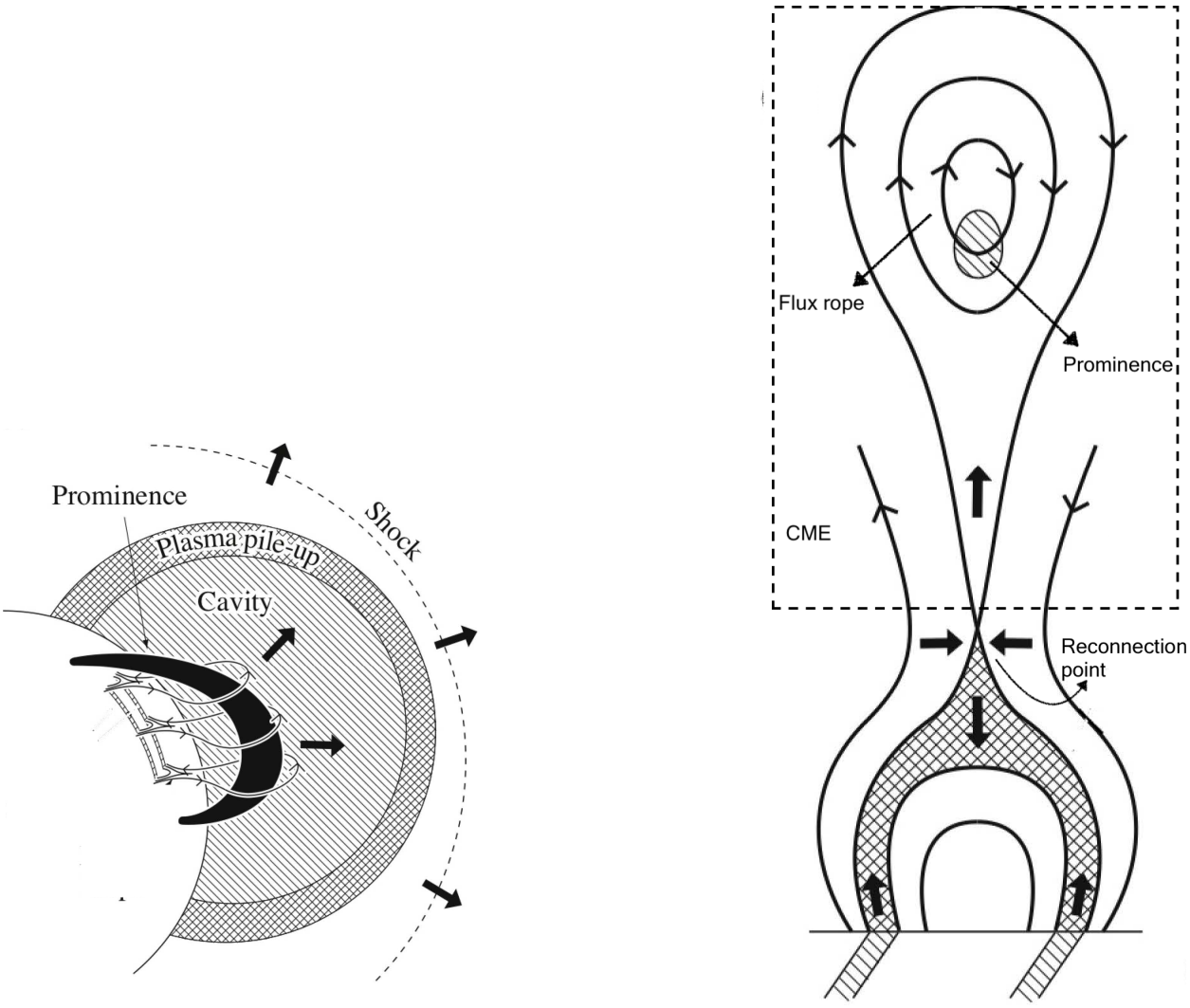

Figure 1.3: Cartoon on the left shows the three-part CME structure on the Sun with prominence in the flux rope. The right image shows the magnetic configuration of an erupting CME reconstructed from the standard flare model. Images have been adapted from Priest (2017).

1.2 X-ray Sigmoids

Sigmoids are large forward-S or inverse-S (Z) shaped magnetic structures on the Sun usually seen in X-ray images. They are significantly active and produce multiple eruptive events during their lifetimes. S-shaped sigmoids are normally found in the southern hemisphere and Z-shaped ones in the northern hemisphere and are thought to assume their shape due to the development of twists via reconnecting field lines between groups of active regions or at the time of flux-tube emergence from below the photosphere (Fan & Gibson, 2003). Their magnetic regions are complex with many new emerging fluxes and a long and winding PIL. The S or inverse-S shaped structures may not be continuous in all sigmoids, although they are seen as continuous S shapes in low resolution X-ray observations and are depicted so in simulations. Some observations have identified them to be made of J shaped structures, with opposite J shaped structures meeting each other at the center of the sigmoid close to the PIL; some of these structures may indeed reconnect to form continuous S shaped loops.

Figure 1.4 shows an image of a sigmoid taken in soft X-rays by Hinode spacecraft (Kosugi et al., 2007). The bright arcs that form the J shapes are hot plasma emitting in X-rays, tracing the magnetic field lines. The plasma in these regions is heated to high temperatures due to the formation of current layers as a result of newly emerging flux at different locations in the sigmoid region reconnecting with the already existing complex fields. Thus, each of the J shaped structures is made of several magnetic loops and fragmented current layers (Archontis et al., 2009).

Depending on the lifetime of their shapes, sigmoids are categorized into transient and persistent ones. Transient sigmoids are small, exist for a few minutes to a few hours and are also seen with J shaped structures that transform into continuous S or inverse-S shaped fields (Huang et al., 2019). Persistent sigmoids exist for several days and are large (distinct on a full Sun image). Transient sigmoids often take their sigmoidal shape prior to eruptions and then losing it upon erupting, but may regain it prior to another eruption. Sigmoid arcades are also seen to form a pointed cusp shaped structure just before eruptions.

The topology of the magnetic field in the sigmoids can be measured using magnetic Helicity, which quantifies the linkage or winding of multiple field lines between each other (mutual helicity) and around its own axis (writhe). The helicity sign or the sign of the twist is predominantly negative in the northern hemisphere and positive in the southern hemisphere. The field lines are approximated to be force-free in the corona and the twist in the field lines can be represented as $\alpha = J_z/B_z$, the ratio of the local vertical electric current to the magnetic field measured over an active region. α is called the force-free parameter in the force-free approximation,

$$\Delta \times B = \alpha B. \tag{1.1}$$

When α is constant, the field is a linear force-free field wherein the twist is constant throughout the volume of an active region along all field lines. α is in reality not a constant over a magnetic region and is different for different field lines. This treatment of α is called the non-linear force-free field (NLFFF) approximation. One sees, from the above equation that an increase in the twist increases current in the plasma along the field lines leading to energy accumulation which is then released explosively in the form of an eruption. An increase in the twist also increases helicity, which is a conserved quantity in environments of high magnetic Reynolds number (fraction of the characteristic speed of the plasma to the characteristic length over the magnetic diffusivity) and is thought to be “removed" from the Sun via CMEs. We use helicity, energy, and α values and signs, calculated over sigmoid regions by using the Energy-Helicity (EnHel) code developed by Georgoulis et al. (2012) that use NLFFF approximations, to understand the threshold of these quantities above which eruptive activities occur, how these quantities evolve during the life of a sigmoid and also compare the calculated and observed signs of α with that of their filament counterpart. This work is presented in chapter 4.

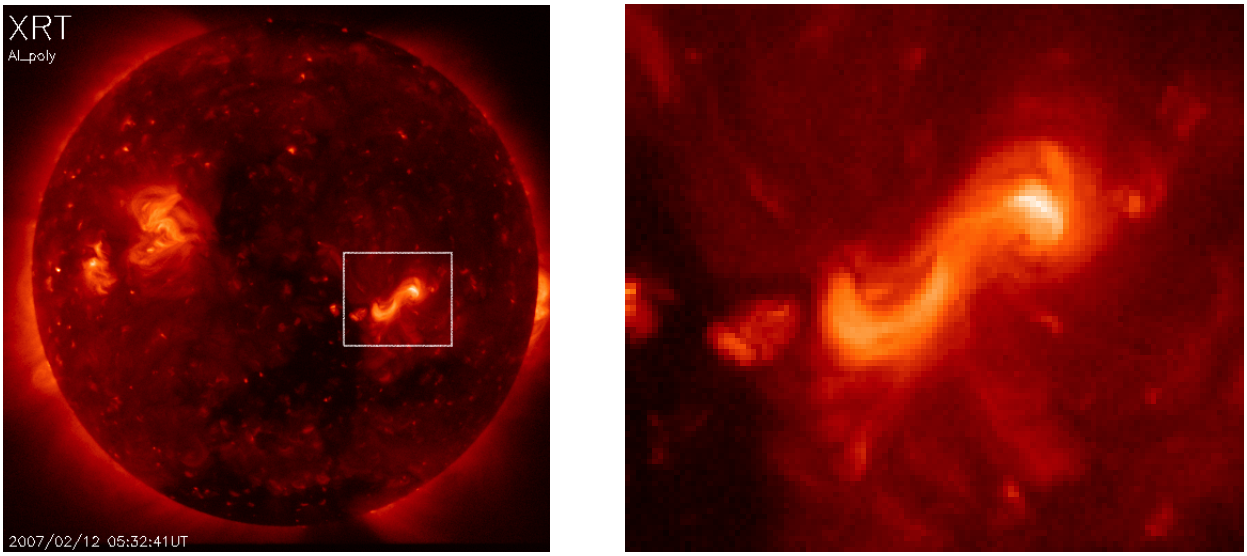

Figure 1.4: Left: S-shaped sigmoid in the southern hemisphere. Right: Zoomed in to show the J and S structures. Image courtesy of Hinode.

1.3 Acoustic Oscillations

High luminosity Cepheid variable stars were some of the first observed pulsating stars because of the dramatic changes in their brightness with time. The main reason for variability in stars on the instability strip of the Hertzsprung-Russell Diagram (Russell, 1914) is that they have not achieved hydrostatic equilibrium which causes the outward gas pressure to exceed the inward gravitational force making the outer layers expand, and then collapse back as the pressure drops. This oscillatory motion reflects in the light curve of these stars with them becoming more and less luminous when they expand and contract, respectively. Such stars pulsate with mainly one mode of oscillation, the fundamental radial mode (Kurtz, 2022), and can be readily observed because of the changes in their light output. Other stars on the instability strip have been observed to oscillate in more than one mode (Dziembowski & Soszyński, 2010).

All stars with an outer convection zone are known to exhibit oscillation, albeit not dramatic but with amplitudes so low they cannot be detected from far except for that of a few modes. However, the proximity to our Sun allows the observations of several modes and about 10^7 modes of vibrations have been found with observations. These vibrations are mainly caused by stochastic excitation

due to turbulence in the convection zone. The most ubiquitous of these vibrations are the 5-minute and 3-minutes oscillations at the photosphere and chromosphere, respectively. These oscillations correspond to the p-mode or pressure-mode oscillations where gas pressure acts as the restoring force (Gough & Toomre, 1991). There are also fundamental and gravity modes, I use the properties of p-mode oscillations in this work.

Just like ripples on the surface of water in a pond, excited waves on the Sun travel in all directions, on the surface, and into the interior. A schematic of this process for p-mode oscillations is shown in Fig 1.5. Different degree modes are shown with different line-styles with the dotted circles representing the acoustic cavity where depending on the mode of vibration, the waves penetrate to a shallow or a deeper depth. Different frequencies of these modes can be observed at the surface and "inverted" to obtain the sound speed at different depths in the interior of the Sun. Using such inversions, the Sun's interior has been mapped precisely to know where the base of the convection zone lies, the rate of differential rotation with depth, temperature structure etc.

Low frequency waves are trapped in the acoustic cavity and form standing waves, only their evanescent signatures can be seen in the solar atmosphere. These waves are trapped mainly because of the abrupt discontinuity of density at the photosphere. However, high frequency waves can escape into the atmosphere and they are observed as travelling waves. Furthermore, waves in the atmosphere are modulated by magnetic fields and make them faster or slower. We study the travel-time of p-mode waves in the vicinity of active magnetic regions to understand how they behave and if they can be used as solar flare predictors. This work is presented in Chapter 5.

1.4 Preview of Results

From the first project (Chapters 2 & 3), I find that obtaining filament axial magnetic fields with the aid of Hα images and magnetograms which are both readily available, the effect of CMEs on the Earth's magnetosphere can be predicted several days in advance. False alarms can be avoided in cases of filaments with a northward component of the axial fields giving rise to CMEs. Using sigmoid features (Chapter 4), I find that monitoring those sigmoids which exhibit opposite signs

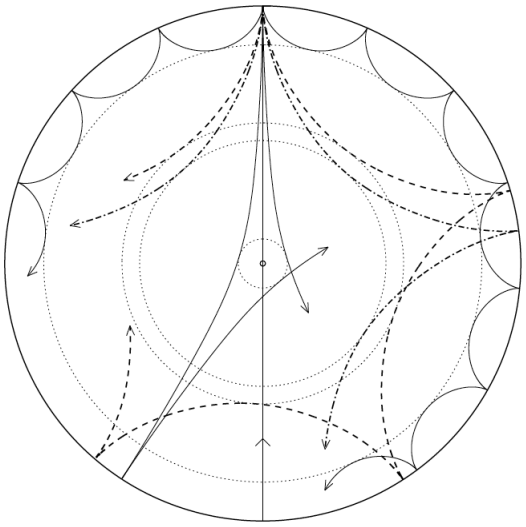

Figure 1.5: Ray paths in the interior of the Sun for different modes represented by the solid and dahsed lines. Dotted lines represent the acoustic cavity in which the respective modes are trapped. Adapted from Kurtz (2022).

of helicities from their filament counterparts are useful because they tend to produce $\sim$3.5 times as many flares and 1.5 times as many CMEs as when the signs between them are the same. Using acoustic waves (Chapter 5), I find that there are possible flare precursors in waves of 6.5 mHz frequency up to 3-15 hours prior to their occurrence, and can potentially be used for predicting flares. This result is alo helpful for pointing small field-of-view telescopes to observe the initial stages of solar flares.

Chapter 2

ANALYSIS OF SOLAR FILAMENTS AND INTER-PLANETARY MAGNETIC FIELD BZ

This work has been published as “Solar filaments and Interplanetary Magnetic Field Bz" in The Astrophysical Journal, Volume 897, Issue 68 (Aparna & Martens, 2020).

2.1 Introduction

Monitoring space weather becomes increasingly important as human activities in space become routine. Effective measures must be taken to mitigate the impact due to explosive events from the Sun to protect power grids, spacecraft, satellites and future astronauts to and from the Moon and on interplanetary voyages. The solar and space weather community uses various techniques to predict the effects of solar explosive events. Coronal Mass Ejections (CMEs) are monitored using coronagraphs such as the SOHO/ LASCO (Solar and Heliospheric Observatory/ Large Angle and Spectrometric Coronagraph; Brueckner et al. 1995). Modeling efforts like WSA-Enlil (Pizzo et al., 2011) strive to obtain precise arrival times of Earth-bound CMEs and/or Co-rotating Interacting Regions (CIRs). While it is important to know when a CME occurs and how soon it will arrive at Earth, it is equally important to know if it will actually affect Earth and cause a geo-magnetic storm. In this work we attempt to understand if the orientation of the axial magnetic field component (B_z) of interplanetary CMEs (ICMEs) near Earth can be predicted by monitoring solar source regions of the CMEs.

Several studies have been conducted in order to obtain the magnetic configuration of the CME source regions on the Sun. Yurchyshyn et al. (2001) used potential field modeling for two active regions that produced Earth-affecting CMEs and determined their helicities. They also calculated

the helicities of the Interplanetary Magnetic Field (IMF) at L1 corresponding to these eruptions using the Advanced Composition Explorer (ACE; Stone et al. 1998). Marubashi (1997) studied 12 magnetic clouds (MC) to infer their axial field directions and compared them with the orientations of nine associated disappearing filaments on the Sun. In both the above studies, the authors find that the orientations of the MC axis match with the orientations of the axes of the associated active region or, the disappearing filaments, respectively on the Sun. Bothmer & Schwenn (1998) found that 8 out of 9 ICMEs retained the helicities of their source regions. Marubashi et al. (2015) conducted an analysis on the relation between the orientation of the filaments on the disk of the Sun and the corresponding storm-causing flux ropes at L1 using flux rope fitting models. Yurchyshyn (2008) performed a comparison of the MC axis for 25 cases using ACE data and the orientation of the post flare arcades at the solar source using EIT images. Palmerio et al. (2018) have analyzed 20 CME-ICME pairs between 2010 and 2015 using chirality to find the flux rope type of the source region and coronal dimmings to find the axis direction of the flux rope.

It is well known that long periods of southward-pointing axial field of MCs or the IMF (B_z) will produce a significantly effective geomagnetic storm (Dungey 1962; Marubashi 1997; Gopalswamy et al. 2008). Because CMEs are known to have flux ropes in interplanetary space (Vourlidas et al., 2013), they must have definite magnetic structure which can be utilized for the predictions of the field orientation (Gopalswamy et al., 2009). Knowing the axis direction of the source region on the Sun and hence the direction of the vertical component, is useful in estimating whether a CME event from the region will cause a geo-magnetic storm. In the current work, we focus on determining the axial field direction of the CME source regions by observationally determining their chirality and correlating it with their ICME counterparts at L1.

Chirality is traditionally determined for Hα filaments using the orientation of the filament barbs with reference to the magnetic polarity inversion line, the direction in which the tail of the fibrils adjacent to the filament or the filament channel point, or by using the skew of post-flare arcade loops (Martin, 1998b). Once the handedness is determined, the direction of the filament axial field can be found with the aid of line-of-sight (LOS) magnetograms. For a list of halo-CMEs in this

study, the enhancement in the IMF $\mathbf{B}_z$ direction is compared with the axis direction of the CME source region on the Sun.

While there have been several studies relating filaments and IMF such as the ones referenced above, the present study is more extensive, relating the two by using a simpler, straightforward method of finding chromospheric filament chirality to get the axial magnetic field direction and the sign of IMF $\mathbf{B}_z$. More importantly, we show that observables such as chirality of chromospheric filaments can be used for determining the geo-effectiveness of solar eruptions which is important in order to avoid taking precautionary measures when not required. Further, training machine learning models to detect the chirality can help automate this process. Feature tracking algorithms that are already in use for tracking filaments and identifying sigmoids (Martens et al., 2012) can be developed for automatically detecting chirality. This will prove beneficial, as will be shown in this paper, for doing the predictions.

We give a brief account of the data and the methods we use in the next section. Section 2.3 describes the methodology of correlating source regions with IMF data. The results are given in section 2.4. In section 2.5, we compare our results with some of the studies mentioned above and give the conclusions.

2.2 Data and Methods

Halo-CMEs from 2007-2017 are analyzed for this study to find correlations between the axial magnetic field direction of eruptive regions on the Sun and the IMF. The list of CMEs during this period has been obtained from the Coordinated Data Analysis Workshop (CDAW)[1] list of halo-CMEs (Gopalswamy et al., 2009). Chiralities of filaments in the source location of eruptive regions on the Sun are obtained using solar images in Hα from the Global Oscillations Network Group (GONG; Harvey et al. 2011) and Kanzelhöhe Observatory (KSO; Pötzi et al. 2015). Chirality is determined mainly using the rules established by Martin (1998b), Martin et al. (2008) and Martin (2015). For quiescent filaments the spatial resolution of GONG which is two arcsec per pixel in

[1] cdaw.gsfc.nasa.gov/CME_list/halo/halo.html

a 2048×2048 frame or 1.02 arcsec in KSO, is quite enough to visually distinguish between a left handed (i.e., sinistral) or right handed (i.e., dextral) chirality filament, either by using barbs or by using fibrils adjacent to the filament. For active region filaments, neither barbs nor fibrils can be resolved using GONG or KSO. Where barbs or fibrils cannot be used for identifying the chirality, the orientation of the overlying potential arcade magnetic field is used for obtaining the direction of the axial magnetic field along the polarity inversion line (see Fig 1. in Martin 1998b).

An example of each of the three methods discussed above for determining chirality is shown in Fig. 2.1. Fig. 2.1a shows a filament whose chirality can be found using the orientation of its barbs. Although filament barbs are used commonly to find the chirality, on some occasions barbs are not visible or are not present (common in active region filaments). In such cases, fibrils in the filament channel (Fig. 2.1c) or post-flare arcades (Fig. 2.1e) can be used effectively to determine the chirality. Fibrils adjacent to the filament spine have similar directionality as the barbs. Looking from the positive polarity, the tails of the fibrils of a dextral filament point away from the viewer. Images of active regions can get easily saturated in ground based images due to high activity and so neither barbs nor fibrils can be used to find their chiralities. These regions may or may not have Hα filaments but they do always have a polarity inversion line (PIL). In most of these cases, the skew of the overlying arcade loops, usually clearly seen in the 171 Å channel of SDO (Solar Dynamics Observatory)/AIA (Atmospheric Imaging Assembly; Lemen et al. 2012), after the flare can be used to obtain the axial field direction of the PIL (see Fig. 1e). Because the post-flare arcade loops are almost potential in nature, they can be used to understand the orientation of the ejecta. In all the above cases, magnetic polarity information (shown in Fig. 2.1b, d and f corresponding to a, c and e) using at least line-of-sight magnetograms is required to determine the direction of the axis. For the CME sources prior to 2010, SOHO EIT (Extreme ultraviolet Imaging Telescope; Delaboudinière et al. 1995) 171Å images along with MDI (Michelson Doppler Imager; Scherrer et al. (1995)) magnetograms are used, while SDO/AIA data and HMI (Helioseismic Magnetic Imager; Scherrer et al. 2012) magnetograms are used post 2010.

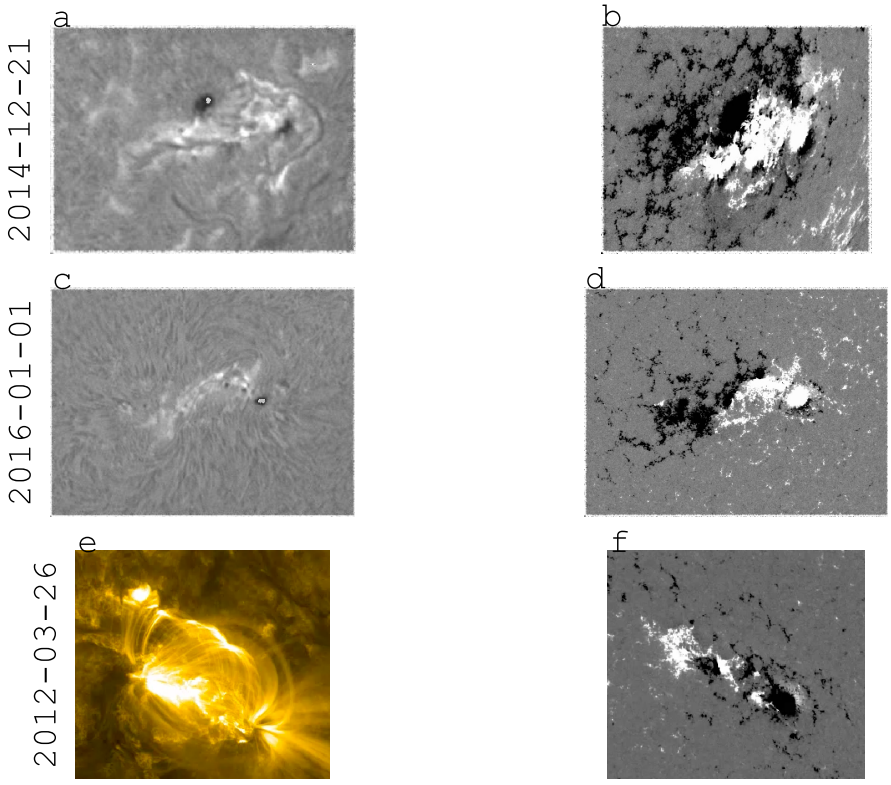

Figure 2.1: Examples for obtaining chirality and axial field of the region using the methods of Martin (1998b). Panels a and b show GONG Hα and the corresponding HMI LOS magnetogram (NOAA AR #12242). The example is used to depict the orientation of barbs with respect to the polarity inversion line that can be identified in panel b. Panel c has visible barbs that are pointing to the right making it a dextral filament, using the polarities from panel d (NOAA AR #12473), the northwest pointing filament axis. Panel e shows post-flare arcade loops whose footpoint polarities are shown in panel f (N18W29).

The near Earth IMF is detected using magnetic field parameters from the ACE magnetometer and plasma parameters from the SWEPAM (Solar Wind Electron Proton and Alpha Monitor; McComas et al. 1998) aboard ACE. These parameters are selected and plotted using the CDAWeb Data Explorer (NASA CDAWeb Development Team, 2019). The details about deriving the various parameters in the CME catalog are given in Gopalswamy et al. (2009). The first two columns of this catalog denote the date and time at which the CME first appears in the LASCO C2 Coronagraph. The third and fourth columns give the apparent and space speed or the actual speed. The space speed is considered for our expected arrival time calculations with buffer time to account for accelerating and decelerating CMEs. Most CMEs take one to six days to reach Earth after the eruption. The CME travel time is calculated linearly for a rough estimate of the expected arrival time. However, we use the acceleration information in the fifth column of the catalog to qualitatively assess the actual speed of the CME and its arrival time.

We conduct our study using the north-south component of the axial magnetic field of the filaments in the CME source regions on the Sun. This is compared with the sign of the ICME Bz values recorded by ACE situated at the L1 Lagrangian point using the estimated arrival time of the CME. The analysis is done in the geocentric solar ecliptic (GSE) coordinate system (Hapgood, 1992). Along with a reasonable estimate of the arrival time of the CME, plasma parameters including B-total, B_z, solar wind velocity, proton density, temperature and the Dst (Disturbance storm-time) index are used for evaluating the signatures and effect of the ICME on the Earth's magnetosphere.

CME occurrences, their onset times and nature (halo, partial halo etc.) are visually confirmed with the help of JHelioviewer (Muller et al., 2009) by simultaneously observing the events in SDO/AIA and HMI channels along with the SOHO LASCO C2/C3 Coronographs. CMEs originating from behind the disk are ignored for this study. In cases of unavailability of magnetogram data or Hα data or when the source is close to the limb, data from a few days earlier or later when the region is on the disk (preferably between -45° and 45° longitude) are used to avoid inaccuracies in estimating the chirality due to the viewing angle projection effects. This is based on a reasonable assumption that the filament chirality does not change with time.

The onset times of the CMEs are important for obtaining reasonable arrival time estimates at Earth. About one to ten CMEs occur per day. However, unless it is a CME with a wide angular width and sufficient speed, it is unlikely to impact the Earth's magnetosphere. Hence, analyzing CMEs from the Halo-CME list, which is a subset of all the CMEs, is deemed sufficient. However, in certain cases, as will be discussed in the next section, the CME arrival time does not match with time of the ICME signatures near Earth, and in some cases there are several CME signatures in the IMF. In these cases the CME catalog consisting of all the CMEs is consulted for one or two days before and after the day of interest in order to assess if those signatures result from other CMEs. Furthermore, the flare class, MPA (Measurement Position Angle) and acceleration columns are left as such in our catalog for making them all available in one place for possible future studies. This study contributes to this database the 10th, 11th and 12th columns that give the IMF B_z obtained by the analysis of the ACE plots, the axial magnetic field direction and the chirality of the source region derived from the analysis of observed filaments, respectively. The list of ICMEs used for this study including our results are available at Harvard Dataverse (Aparna, 2019).The following section explores in detail some of the events.

2.3 Analysis

CMEs originate as singular eruptions on the Sun but as they travel through the interplanetary space they may interact with other disturbances (CMEs or CIRs). There may be one or multiple CME signatures near Earth (e.g. Fig. 2.2), signatures of CIRs (e.g. Fig. 2.3) caused by the interaction between fast and slow solar wind regions or a combination of these making it a challenge to correctly identify what caused which structure and relate them to their source regions on the Sun. In order to consistently identify the features we adhere to certain criteria that have been previously adapted by Burlaga et al. (1981), Forsyth & Marsch (1999), Gopalswamy (2009), etc. We briefly discuss these criteria below.

Depending on the viewing angle of the spacecraft, it may or may not see a magnetic cloud (i.e., a flux rope) in the three-part CME structure. The most common features for identifying a CME near

the Earth, commonly called ICME (Interplanetary CME), are the enhancement in the total magnetic field and an abrupt increase in the solar wind speed indicating a fast shock wave, temperature and pressure. The effects of an ICME may last for a few hours up to a few days. In the ICME structure the sheath region between the shock-front and the ICME volume is indicated by rapidly varying magnetic field prior to its enhancement (Kilpua et al. 2017 & references therein). The magnetic cloud is indicated by the enhancement in the total magnetic field that decreases gradually over the time of passage of the CME through the spacecraft (indicated in Fig. 2.2). In cases of CIRs, there are typical mesa (table-like) or inverse mesa like structures (indicated in Fig. 2.3) in the proton density, velocity and alpha-particle-to-proton ratio profiles (not shown in the figure) (Burlaga et al., 1981).

Strong or long-lasting southward-pointing ICME magnetic fields have the largest effects on the Earth's magnetosphere. We observe the enhancement in the B_z component of the ICME magnetic field associated with the CME source region on the Sun. The associated region on the Sun that produced the CME is determined using the time when it was first observed by the LASCO C2 Coronagraph on SOHO and the flare onset time and location as recorded in the CDAW catalog. The ejection is visually confirmed by observing coronal dimming, post-flare arcade loops and/or filament eruptions.

In order to ensure that an Earth-bound CME corresponds to a particular ICME, we check for other CMEs within ± 2 days from that date. Halo-CMEs are more likely to cause fluctuations in the Earth's magnetosphere compared to partial-halo CMEs. Narrow and slow CMEs have very low probability of causing an appreciable impact. In almost all cases in our study, non-halo CMEs were of angular width less than 60 degrees and slow (< 500 km/s) which are reasonably considered as poor events in the CME catalog. Further, arrival estimates for CMEs match with the ICME signatures. We are confident that the above steps strongly ensure that the ICMEs correspond to their designated CME counterpart and no major interaction occurred in the inner heliosphere. Our results are summarized below.

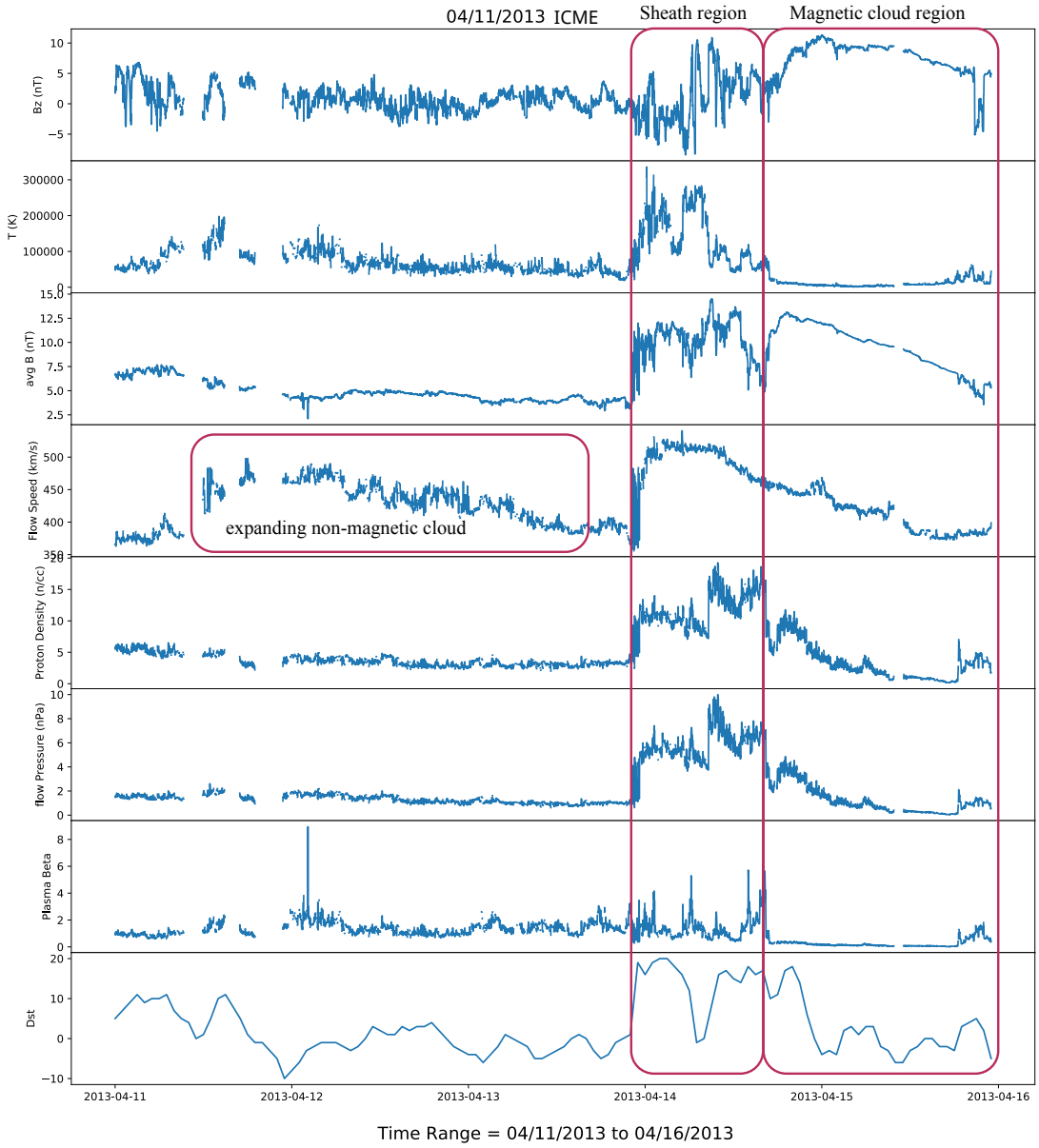

Figure 2.2: Example of solar wind containing at least one ICME structure with a northward enhancement as seen in the Bz panel. Flow speed, density, and pressure show a gradual decrease indicating an expanding ICME. The boxed region on the left shows an example of the signature of a non-MC. The boxed region on the right depicts the duration of the sheath region and the CME at L1.

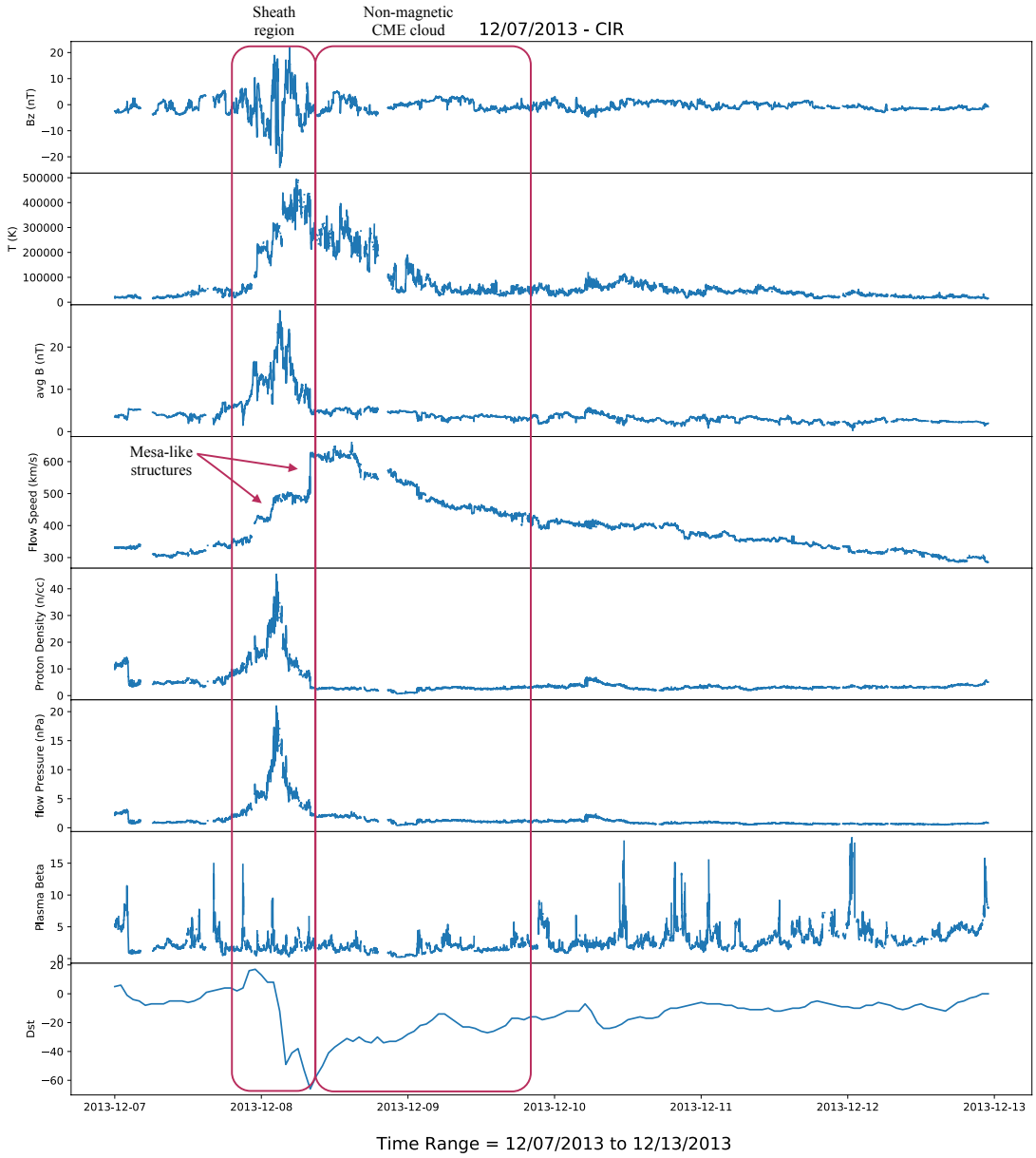

Figure 2.3: Solar wind at L1 indicating a CIR with Bz oscillating between southward (negative) and northward (positive) and flow speed exhibiting a mesa-like structure. There was indeed a CME that launched from the Sun with an initial speed of 1165 km s1 and an expected arrival time of 1.5 days. The CME (nonmagnetic) signature follows the CIR in the flow speed profile as indicated by the arrows. The boxed regions depict the duration and properties of the CIR and CME as seen at L1.

2.4 Results

The total number of CMEs in the 2007-2017 period is more than 30,000. Among these, the number of halo-CMEs in the said time period is 292. Out of the 292 halo-CMEs, 206 occurred on the backside of the Sun or no ICME type signatures were seen near the Earth - these are not considered in our analysis. For all of the remaining 86 ICMEs, the axial magnetic field direction of the CME source on the Sun is determined using the chirality method as described in section 2.2.

Out of the 86 CMEs that occurred from the solar side facing Earth, 63 have the same orientation at L1 as their filament counterpart had on the Sun. Of the remaining 23, 12 ICMEs were such that they couldn't be classified as having a north or south component at L1 or at the Sun due to either low resolution images or ambiguity in ACE data. The remaining 11 events showed opposite configuration at L1 compared to that at the source region.

We summarize the reasons for non-classification of the ambiguous 12 ICMEs as follows:

- There are two ICMEs that are non-magnetic cloud structures (ICMEs #11 and #199 in the catalog), hence their preference for orientation could not be determined.

- Two ICMEs (#91 and #183) were tightly wound regions that produced jet-like features on the Sun; there were no filaments in these regions to identify the chirality and direction of the axis.

- For one event (#43) the ICME signature was not observed at the expected time, perhaps because it did not reach Earth; its corresponding chirality sign and thus the axis direction also could not be determined because the flare occurred when the region was at the limb. The region was rotated to a later day to find the chirality but it was still very active and saturated, so no signatures could be seen.

- #75 did not show any ICME signatures and #110 showed CIR type signatures.

- One event (#121) showed signatures of three ICMEs, two showing negative and one showing positive B_z enhancements. On the Sun, there were three partial halo-CMEs in addition to the

halo-CME within about three hours of each other, two of these regions have a southward and one has a northward pointing axis region.

- Two events (#s 81 & 221) did not show much variation (signal within the solar wind) in B_z but only small variations are seen in B_x and B_y. The source region for #81 was southward pointing, but the CME originated from the west limb. It is possible that only a small portion of the ICMEs (for ex. its flank) was seen by ACE. Also likely, the structure may have rotated in the interplanetary space which may explain the non-detection of the B_z enhancement.

- One ICME (#272) showed short time signatures of southward and northward B_z. On the Sun, there was one halo and three partial halo CMEs that were produced on that day, hence it was not possible to determine the exact correlation for this ICME. In addition, the Dst index did not drop below -30 during this ICME and so it did not have much effect on Earth.

- For ICME #239, the enhancement in Bz was positive at the expected arrival time. However, the corresponding CME originated at the west limb and another halo-CME (#240) occurred on the same day from a heliographic longitude of 40W that has a somewhat higher likelihood of affecting Earth (Gopalswamy et al., 2011). Thus we suspect that the observed signatures of #239 was actually due to #240.

Eleven ICMEs - 12, 22, 94, 95, 112, 146, 147, 159, 257, 266 and 281 show opposite IMF B_z signatures than their filament counterparts. We confirm that no other strong and wide CMEs occurred close to the times of these CMEs. Because of this, we speculate that these ICMEs may have either rotated after the eruption or deflected due to encountering coronal holes or CIRs. Based on the above lists, we have 74 ICMEs out of which 63 show non-rotational behavior and 11 suggest rotational behavior. We present the results in the form of a confusion matrix (Ting, 2017) or a truth table in Table 2.4 showing the number of northward and southward sources correlating with the number of northward and southward ICME B_zs. It is pertinent to give statistical quantities such as recall (a probability of detection or sensitivity) and precision (a success ratio) (Ting, 2011) for a classification such as ours where the same direction of IMF B_z and the CME source region acts

Table 2.1. Distribution of filaments. Number of ICMEs = 71, Recall = 76.9 %, Precision = 96.77%

Filament Field → IMF Bz ↓	North	South
Northward	30	9
Southward	1	31

as the classifier. Considering southward B_z as positive predictions, i.e., anti-alignment of Bz with respect to that of Earth's dipole field in which case geo-magnetic storms will occur, we calculate a recall of 94.3% and a precision of 78.5% suggesting that a model algorithm will be required to improve the precision. This might be possible with more data. The higher recall suggests a lower number of false negative cases and hence the number of times an unnecessary precaution is taken will be very low.

2.5 Discussion & Conclusions

This study has provided a strong observational evidence that the north-south component of the axial field of solar chromospheric filaments and active regions obtained by assessing the chirality can be used effectively for determining the direction of the ICME magnetic fields at L1 and, by extension, for determining the geo-effectiveness of these CMEs. We determine the direction of the axial field of the filaments using chirality, however, we only consider the B_z component of the axial field (and then find whether it agrees with the B_z component of the ICME flux rope at L1). The other studies discussed here focus on the orientation of the axial field and not just B_z.

In their study, Marubashi et al. (2015) obtain the helicity of flux ropes at L1 using flux rope fitting methods and fit the axis of the flux rope on to the source region for filaments between 1996 and 2006 (our data covers from 2007 to 2017). They find that the polarity inversion line of the source region makes a similar angle as the flux rope at L1 within a range of about 25° for all cases in their data. They however do not obtain the direction of the axial field of the source region

separate from the interplanetary flux rope measurements like we do. Similar to the above study, Yurchyshyn (2008) obtains the axis of the CME source using the method described in Yurchyshyn et al. (2001). They then fit ellipses to the shape of the halo-CME (LASCO images) to obtain the CME orientation angle at $2.5R_{sun}$ for 25 cases and find a very good correlation (95%) between the EIT arcade angles and the halo-CME axis but a 77% correlation between the halo-CME orientation and the MC orientation angles at L1; they suggest that the rest of the CMEs have rotated by more than 45°. We note that both of these studies are not inconsistent with our results.

Palmerio et al. (2018) have compared the orientation of the flux rope at L1 and that at the source using the method of chirality for 20 CMEs between 2010 and 2015 that could be observed simultaneously by STEREO, SOHO and SDO. Their analysis results in 55% of the cases being a match between the source and the in-situ measurements of the ICME. Fifteen of their regions are common with ours and we find that we obtain the same filament axial field direction for 12 of the 15 cases. Eleven out of 15 ICME flux rope axial field component directions at L1, which were deduced from their flux rope types, match with our B_z sign. It is difficult to be certain about the mismatches in filament field directions because the methods used by them to find chirality (e.g. EUV sigmoids, magnetic tongues etc.) are different from ours for some of their cases. The axial field direction is sensitive to chirality; if one determines the region is right chirality but is actually left, then the sign of the field direction would be just the opposite. Further, our study on the relation between sigmoid shape and filament chirality (in preparation) suggests that there is no absolute relation between the two. The mismatches in the B_z component at L1 are attributed to the fact that we use the vertical component of the axial field at L1 and they use the total field using flux rope fitting methods. This as suggested in Palmerio et al. (2018) sometimes gives an opposite configuration. To compare the precision and recall metrics of their data, we derived the Bz component using the source 'flux-rope type' for the filaments on the Sun and the 'flux-rope type' was obtained by fitting methods at L1 (e.g. WNE would give a northward axial field direction). We calculate a precision and recall of about 66.6 and 72.7% respectively for their data. Ours is a somewhat better result but we do use a larger sample of events; as Palmerio et al. (2018) studied only 20 filaments, the difference in the

percentages is likely due to the better statistical significance of our sample. Further comparison of the methods is of little meaning at this point as we believe that our method will be of use as a first step for obtaining the quick knowledge of effectiveness and the computational methods (like extrapolations and flux-rope fitting) for further determining the magnitude of the CME impact.

Bothmer & Schwenn (1998) compared the helicity of a set of quiescent filaments using the hemispheric helicity preference (Rust & Kumar, 1994) with their ICME counterparts. They found a significant agreement in quiescent filaments to the rule (89%; total 9 filaments). Savani et al. (2015) also used the hemispheric helicity rule for obtaining the axis orientation for eight events but they warn that extra care must be taken while determining axis orientation of filaments that are between multiple active regions. Several statistical surveys on the hemispheric preference of helicity show varying degrees of compliance (for example, see Xu et al. 2009). In some of these studies (e.g. Martin et al. 1994), quiet regions show a higher degree of preference compared to the active regions. However, none of the studies show a 100% compliance with the hemispheric helicity rule indicating that independently obtaining the field direction at each source region is important. In order to avoid errors arising from exceptions in the hemispheric helicity rule and/ or issues in disambiguation techniques, we have relied solely on filament observations and LOS magnetograms for obtaining the required parameters. We believe our method has performed well and has given reliable results. The human eye performs well in obtaining the chirality with images of reasonable resolution, but it is impractical to have human eyes analyze each and every filament. The advent of computer vision in solar physics is promising: automating filament chirality determination using machine learning techniques (Martens et al., 2012; Aggarwal et al., 2018) will help in preparing computationally efficient and effective measures against severe space weather effects.

Knowing whether there will be a geomagnetic effect or not is of primary importance to start taking precautionary measures. However, precautionary measures during a false alarm and the resulting expenditures can be avoided with the method used in this paper. Further, our method of determining the axial field direction is quick and straightforward than computationally expensive

methods such as force free extrapolations and determining helicity (Yurchyshyn et al. 2001, Bothmer & Schwenn 1998, etc).

In the current study we consider only the north-south component of the axial magnetic field of the filament. This is deemed useful as a first step in omitting ICMEs that will not be geo-effective. However, it is necessary to know the exact, quantitative direction and strength to determine where an ICME might reconnect with the magnetosphere and its severity. Utilizing vector magnetograms to determine the exact orientation and further study the field in the corresponding flux ropes at L1 will be useful in determining their orientations. Active region filaments have fibrils and barbs that are smaller than the resolution limit of most available telescopes. Gosain & Brandenburg (2019) show that small scale magnetic fields emerging in active regions usually have opposite helicity compared to that in the already existing active region. Hence, analysis by looking at small filaments in active regions may lead to an incorrect assessment of their chirality. Ultra-high resolution spectropolarimetric instruments such as those on DKIST (Daniel K. Inouye Solar Telescope; Tritschler et al. 2016) will prove immensely useful in further understanding the filament magnetic field especially in active regions and the orientation of the barbs and fibrils adjacent to the filament spine.

The data-set used for this study to determine ICME geo-effectiveness is by far the largest used, with 86 Earth-bound CMEs between 2007 and 2017. There are a few assumptions that this study has considered that can be improved. In reality, the CME travel time is not linear (acceleration and deceleration are not considered in calculating the expected arrival time, instead initial speed as calculated from LASCO observations is used) because of drag effects due to interaction with the solar wind, other CMEs and CIRs. However, considering a qualitative estimate of the CME arrival time using the speed and acceleration information, almost all of the ICMEs were accounted for. Obtaining chirality with low resolution data is a challenge; we have attempted an unbiased analysis of the filament regions in this study to obtain the chirality. However, it is possible that, due to unavailability of high resolution data, some filaments may have been mistaken to be of opposite

chirality (Martin, 2015). However, we are certain that observationaly a correlation between CME and ICME orientations prevails.

Chapter 3

USING CME PROGENITORS TO ASSESS CME GEOEFFECTIVENESS

This work has been published as “Using CME Progenitors to Assess CME Geoeffectiveness" in The Astrophysical Journal, Volume 257, Issue 33 (Mundra, Aparna, & Martens, 2021).

3.1 Introduction

Establishing an empirical connection between eruptive events on the Sun and their interplanetary magnetic signatures is of prime importance for successful space weather predictions. We analyze relevant solar features that can give substantial clues to predicting devastating geomagnetic storms, some of which are capable of ravaging power supplies on Earth and satellites in space. We do a comparative analysis of axial field directions of coronal mass ejection (CME) progenitor regions on the Sun, namely, filaments and active regions, with that of their CME counterpart in the interplanetary space. This is a follow up analysis of Aparna & Martens (2020), hereafter AM20, who analysed the source locations of halo-CMEs and their Interplanetary Magnetic Field (IMF) counterparts near the Earth from 2007 to 2017. With the largest data-set ever used for such a study, they observationally established that the axial field direction of CME source locations can be used for a yes/no type of prediction for geo-effectiveness due to the CMEs. The current paper includes the halo-CME data-set from the years 1996-2006 and complements the results from AM20, providing a stronger base for their conclusions.

Long period and southward pointing IMFs cause some of the most intense geomagnetic storms. Several studies have been conducted to systematically understand CME structures before eruption and their evolution in the interplanetary space in the context of their Geo-effectiveness. Marubashi

et al. (2015) compare the axial orientation of the interplanetary CMEs (ICMEs) with that of the post eruptive arcades on the Sun, however, they obtain the axial direction of the source region by assuming the same helicity sign as that of the IMF which they obtain via flux rope fitting methods. Similar to our analysis on the solar source regions of halo-CMEs, Palmerio et al. (2018) use observations of features such as filaments, Hα ribbons, post flare arcade loops to obtain the axial direction. Both Marubashi et al. and Palmerio et al. use flux rope fitting for the ICMEs near the Earth. Some studies like Yurchyshyn et al. (2007) have used field extrapolation of source regions to obtain the helicity of the flux rope and compare it with that at L1. All these studies yield (to varying degrees) an overall inclination to understanding that for most CMEs the axial direction is retained. We refer to AM20 for a detailed discussion of these results. Further, we utilize these understandings and suggest a straight forward technique to forecast if a geoeffective event will occur from a chromospheric filament or a CME source region on the Sun.

While several of the previous reports like Marubashi et al., Yurchyshyn et al., Bothmer & Schwenn (1998) etc. have studied in detail the structure of the interplanetary flux ropes due to CMEs in comparison with that of the source locations, we emphasize that knowing the direction of the vertical component of the magnetic field of the axis is sufficient for a first degree estimate of geoeffectiveness for space weather prediction purposes. In doing so, they can be highly effective because the predictions can be made days in advance.

We refer to AM20 for a detailed comparison of the methods used in the above-mentioned studies. Unlike these studies, the focus in AM20 is on Bz, which is used to determine the geo-effectiveness of CMEs. Their data-set covering solar cycle 24 is by far the largest and they classify $\sim$85% of the cases to have a match. This has been a strong result and has the potential to provide effective space-weather predictive capabilities by only observing chromospheric filaments, continuous observations of which are readily available. The current paper explores data over solar cycle 23 to understand whether the result is consistent over time. We discuss the data and the methods used in this paper in the next section, analysis of our results in section 3.3 and conclusions in section 3.4.

3.2 Data and Methods

The methods used in AM20 are followed to conduct the analysis for this work. A brief account on the same is given below. Halo-CMEs from the 1996-2006 time-frame, listed in the Coordinated Data Analysis Workshop (CDAW) catalog[1] (Gopalswamy et al., 2009) are used. The CMEs are analyzed to determine a correlation between the axial field direction of their source events and the IMF orientation after a calculated number of days the CME is due to reach Earth. The IMF data in the Geocentric Solar Ecliptic (GSE) coordinate system is obtained from the NASA CDAWeb site. In addition to the magnetic field, data corresponding to temperature, flow speed, plasma density and plasma-beta are used in order to determine if the magnetic cloud exists in the ICME (Burlaga et al., 1981; Zurbuchen & Richardson, 2006; Kilpua et al., 2017). Furthermore, Dst indices, which give a measure for the disturbance in the Earth's magnetic field, from ground based magnetometers is used to verify if the CME had an impact on the geomagentic field. The number of days for the CME to reach Earth is calculated by taking the distance between Earth and the Sun and dividing it by the space-speed of an incoming CME. An example of the IMF data is shown in Fig. 3.4. Gonzalez & Tsurutani (1987) determined that the causes of large geomagnetic storms are large negative changes in the Bz, exceeding -10 nT. The plots shown in the figure indicate a potential geomagnetic storm. The Dst plot in the last panel of the figure shows a sharp drop to below -100 nT, which indicates a severe disturbance in the Earth's magnetosphere. The Bz and Dst changes occur almost at the same time indicating a causal link (Burton et al., 1975).

We compare the Bz component of the IMF orientation to that of the source region on the Sun by obtaining the axial field of the source region using the method of chirality (Martin, 1998b). In order to analyze the events on the Sun, Hα images from the Kanzelhöhe Solar Observatory (KSO; Pötzi et al. 2015) and the Big Bear Solar Observatory (BBSO) were used; and the SOHO (Solar and Heliospheric Observatory) Extreme-ultraviolet Imaging Telescope (EIT; Delaboudinière et al. 1995) 195Å and Michelson Doppler Imager (MDI; Scherrer et al. 1995) magnetogram features were used

[1] https://cdaw.gsfc.nasa.gov/CME_list/halo/

for the arcades. This article further explains the usages of these data. To determine the chiralities of the filaments, two methods are employed.

1) Hα method: We use filament barbs by visually analyzing Hα images from KSO/BBSO for the corresponding date of the CME and obtain the filament chirality. An example of a northward directed filament is shown in Fig. 3.1. This is evidenced by the direction of the barbs and the polarity information obtained from the magnetograms. The minority polarities are shown in smaller font (negative and positive signs) in the figure, and the direction of the filament axis is obtained by moving along the barbs from the positive to the negative ends, as viewed from the positive polarity side. As opposed to this, a left bearing filament would have its barbs going towards the left, as seen from the positive polarity side again (Martin, 1998b). Applying this method to the filament in Fig. 3.1, we get an axial field pointing north-eastwards and a vertical component that is northward.

2) Arcade method: In the cases of active regions where the filament barbs are usually not resolved, we use the skew of the post-flare arcade loops with reference to the polarity inversion line (PIL) when seen from the positive polarity side as suggested in Martin (1998b). An example is shown in Fig. 3.2 and Fig. 3.3 shows the corresponding polarities and the overlying arcades. The arcade is skewed to the left making the axis point towards the north-west and thus getting a northward vertical component. The IMF Bz orientation of an ICME, whether it is positive (north) or negative (south), is then compared with this axial field direction of the source region thus obtained, to determine a correlation. The JHelioviewer application (Müller et al., 2017) was used for analysing the arcades using SOHO EIT 195Å images together with the MDI magnetograms for the polarities to determine the directionality of the axis. Similar to AM20, only halo-CMEs are considered for this study. The catalog was examined, and because this study involves visual examination of the surface of the sun, any CMEs from the backside or near the limb (70°-90°) were not used.

3) Several other features such as Hα flare ribbons, coronal dimming and chromospheric fibrils have been used in several of the studies mentioned earlier. We adhere to the methods described in this section as we find them sufficient for our cases of halo-CMEs.

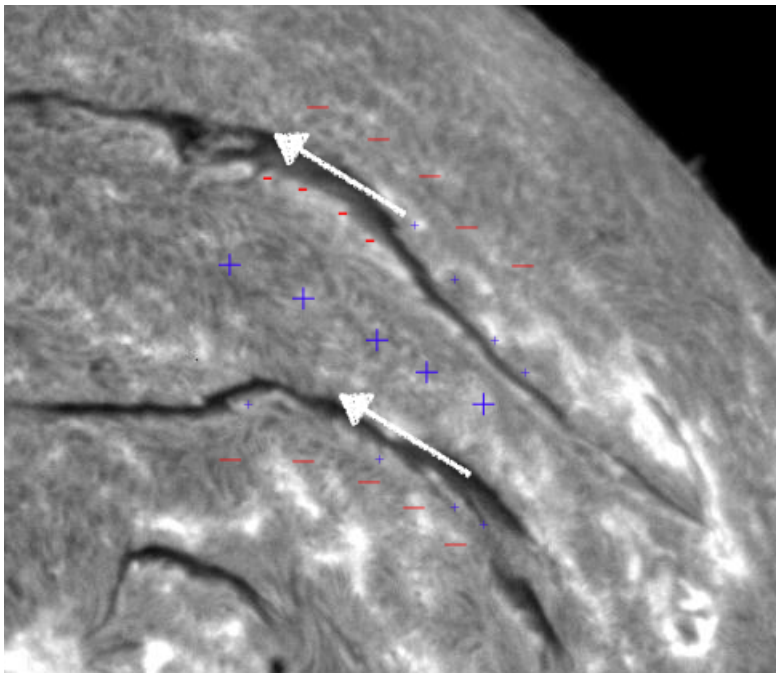

Figure 3.1: Axial field directions of surface filaments in the north-western part of the Sun on 02/09/2001 cutout from the BBSO archive. The positive and negative regions obtained from the MDI magnetogram are shown in blue and red, respectively. The pluses and the minuses in smaller font depict the minority polarities (Martin, 1998b)

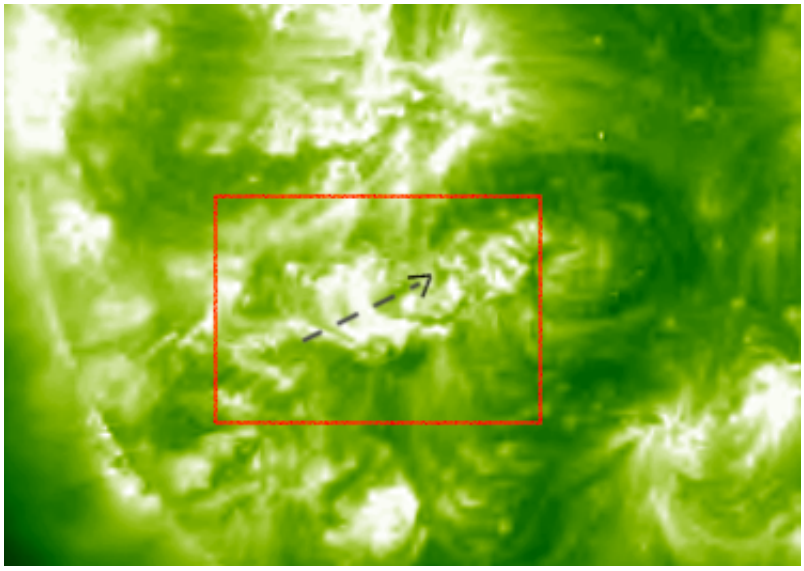

Figure 3.2: A screenshot of the post-flare arcade loops (encased in the red box) for the flare on 2000-11-01 is shown. The black dashed line roughly represents the polarity inversion line. The corresponding magnetogram is shown in Fig. 3.3.

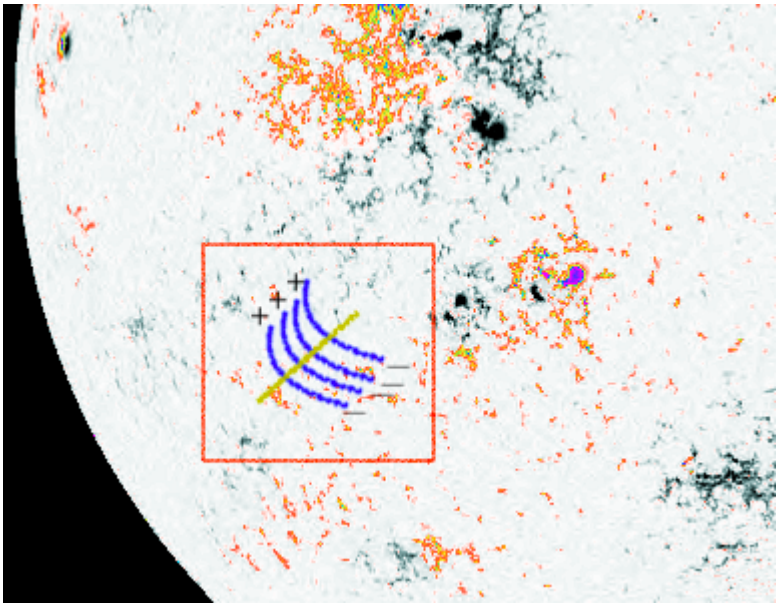

Figure 3.3: MDI magnetogram rendering of the 2000-11-01 Sun. Orange and grey represent negative and positive polarities respectively. The active region shown in Fig. 3.2 has been encased in the red box. The EIT 195Å arcade loops have been drawn in blue over the polarity inversion line (yellow-brown).

On the Sun, the vertical component of the CME source region is northward or southward depending on the axial direction determined from chirality. In the IMF, the positive or negative enhancements seen in the Bz profiles that represent the magnetic cloud region following the jittery sheath region are considered as north or south respectively. Following the work of Nieves-Chinchilla et al. (2019), east-west (or west-east) oriented flux-ropes show signatures in Bz that rotates from positive (negative) to negative (positive), i.e., they show both north and south Bz components, and hence by definition and by observation, they interact with the Earth's magnetosphere to cause a storm (see Fig. 3.4 for example). The east-west cases sometimes show similar duration and strength in both the positive and negative enhancements in the Bz profiles, appearing to be almost symmetric. Such cases are very few in our study (5/102) and are not included in the category of those that will or will not cause a storm, for the sake of simplicity. On the other hand, there are asymmetric cases where one of the signs is over 70% in duration or strength or both than the other sign. In such cases, we assign the respective ICME Bz with the dominant sign and direction (north or south), as also suggested in Nieves-Chinchilla et al. (2019).

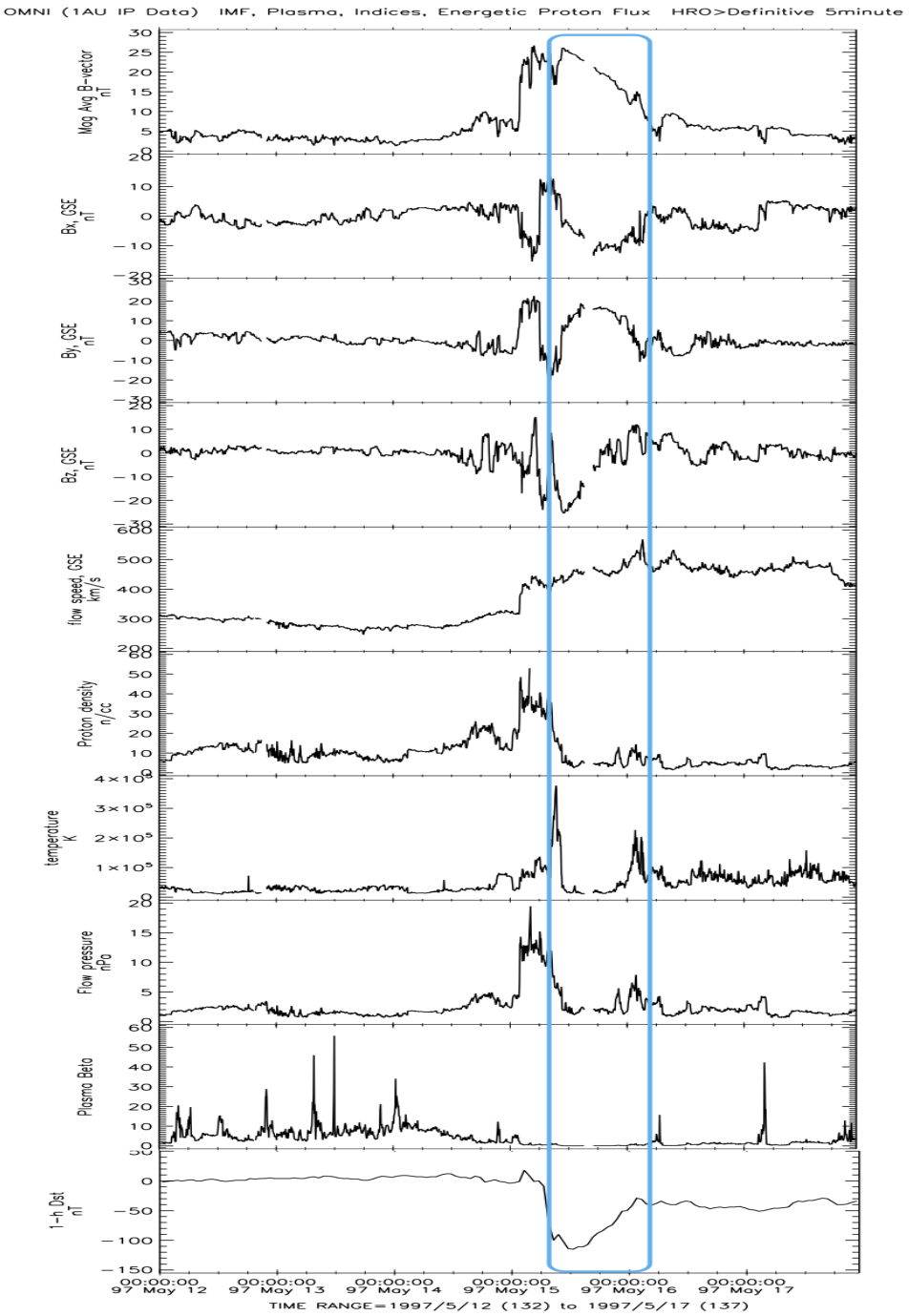

Figure 3.4: Plots showing the variation of the different parameters from ACE (via CDAWeb) used for analysing the IMF. The data is presented in five minute time cadence. This graph in particular is focused on the CME which occurred on May 12th, 1997. The Bz data when the CME reaches Earth shows a south-dominant orientation, so the Bz data for this date has been classified as “south”. The ICME magnetic cloud enclosed by the blue box.

3.3 Analysis

The halo-CME list for the years 1996-2006 has 393 events listed in the CDAW catalog. Figure 3.5 shows the yearly distribution of all the CMEs (in blue) and the halo-CMEs (in red) for both the cycles 23 and 24. The chart is shown to loosely illustrate the progress of Solar Cycles 23 and part of 24 (AM20), which peaked in 2001 and 2014, respectively. The number of halo-CMEs occurring steadily increased until 2001, while the all-CMEs chart shows maxima in the years 2000 and 2002. The CME:halo-CME ratio was about 30:1. The year 2007 in the HALO CMEs chart is an outlier, as a considerably higher-than-average amount of HALO CMEs occurred that year after the solar maximum.

Of the 393 halo-CMEs, 102 cases were able to be determined for both the source region axial field and the orientation of the Bz of the ICMEs near the Earth. Of these 102, 66 CMEs had identical axial field vertical-component and the IMF Bz orientation, while 31 had the opposite orientations. Therefore, 65% of the CMEs' axial directions and IMF Bz orientations agree, while that of 30% do not. The rest 5% (5 events) comprise of the east-west axial flux ropes that show both positive and negative signatures in the Bz profiles (Nieves-Chinchilla et al., 2019). These are categorised as NS; here we point that 'NS' is a nonspecific term, we do not imply that north was leading the south. The results are presented in Table 3.1. The CMEs that have a mismatch between the filament axial field and the IMF Bz are thought to be so because of rotation in the inter-planetary space (Yurchyshyn et al., 2007; Kilpua et al., 2017). This includes the cases where the axial direction was originally mostly horizontal such that a small rotation can cause a change in the vertical component of the axial field from north to south or vice-versa.

The remaining 291 events could not be determined because of various reasons: 27 events had a well determined filament axial field direction but the corresponding IMF Bz was indeterminable because of a multitude of reasons, including the lack of an in-situ ICME signature or the detection of a non-magnetic cloud ICME, which may be due to interaction with other structures (Burlaga et al., 2001; Lugaz & Farrugia, 2014), or a signature being too late or too early outside of a reasonable

arrival time for the CMEs. The CMEs that had no IMF Bz signatures but were visible in terms of filament chirality may have missed detection near Earth for many reasons, one of which could be because of the deflection of the magnetic cloud away from Earth. Wang et al. (2004) give examples for CMEs that can miss the Earth entirely or are deflected. On the other hand, for 24 events, the IMF Bz orientation was determined, but the filament axis direction could not be determined due to reasons such as the images on and around the days of the event being absent from the catalog, low resolution and events being near the limb. Seventy-eight events were completely undetermined in both the axial direction and the Bz, and 93 events were too far out to the east or the west, approaching the limb, to be confidently determined as dextral or sinistral chirality. We note that with current instrumentation, many of these cases would be resolved. Table 3.2 summarizes these numbers accordingly and Table 3.3 gives the details for the determined set of data with a description of the columns in the caption. The analysed data is also available in the Harvard Dataverse (Aparna, 2021). Figure 3.6 shows the distribution of the 102 determined events on the Sun of this study as well as those for AM20. This figure indicates an almost symmetric distribution of the source locations of the halo-CMEs, opposite to that found by Wang et al. (2004). Further investigation into this will help understand possibly the nature of deflections in CMEs but is not within the scope of this paper.

We notice the difference in the match rates between our results and that of AM20. We speculate that the reason for the lower percentage of positively correlated CMEs in our dataset is a combination of factors such as solar maximum and the quality of the images. The lower quality of the chromospheric filament images (which gives the chirality) and the unavailability of EIT images during a flare (used for getting the skew of the overlying post-flare arcades if the filament images are unusable or unavailable) due to its low cadence affect the analysis process in that, some of the filaments may be interpreted incorrectly. There is a higher chance of interpreting them incorrectly during solar maximum when a greater number of active region filaments, which are usually thin and without well-developed barbs and hence difficult to readily obtain the chirality, are associated with CMEs.

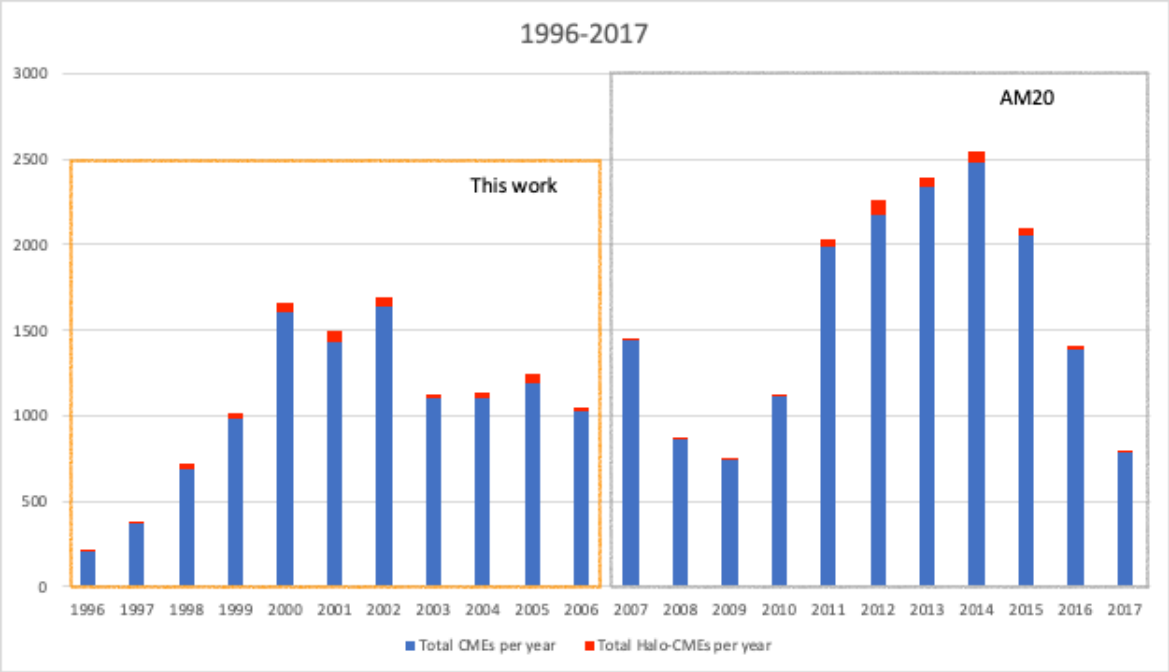

Figure 3.5: CME and halo-CME occurrence during Solar Cycle 23 (peak 2001) and part of Solar Cycle 24 (peak 2014).

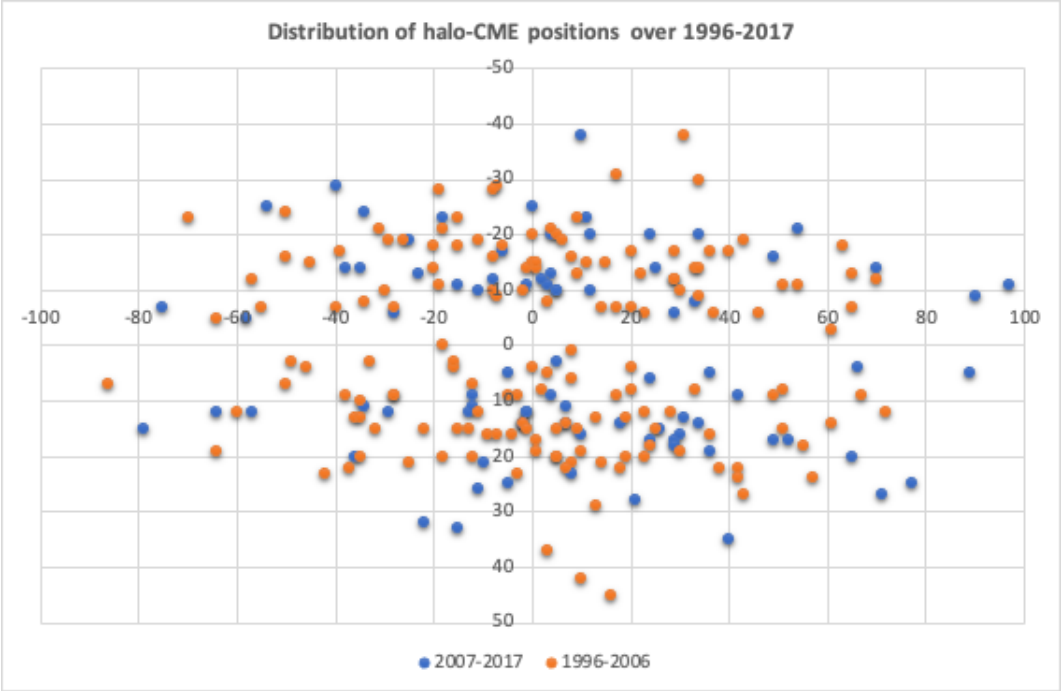

Figure 3.6: Distribution of the CME events analyzed in this paper and the ones in AM20. The graph demonstrates that the vast majority of events fall between 30N and 30S, and 40E and 40W.

3.4 Discussion & Conclusions

Through a thorough investigation of an additional set of data apart from that analysed by Aparna & Martens (2020) who found a match rate of $\sim$85%, we have further fortified the evidence for the correlation between the vertical components of the axial magnetic field direction of eruptive events on the Sun with that of their corresponding IMF measured near the Earth. Further, combining the halo-CME data from AM20 and this work together, we get a match percentage of 75% for the solar cycles 23 and 24 combined. We expect that with good quality data the match percentage would be higher like that seen in AM20.

With a set of 102 CMEs determined in this analysis between the period 1996-2006, a 65% match rate between the correlations of the filament axes and the IMF Bz orientations was found. In this study we prioritize using the north or south component of the field directions of filament axis and positive or negative orientation of the IMF Bz as opposed to some of the other studies such as Palmerio et al. (2018) and Marubashi et al. (2015) to obtain a first degree assessment of a possible space weather impact.

Some assumptions this work has made include assuming that the speed of a CME arriving at the Earth is constant, as this is not entirely true in every case. In this work, the utmost care has been taken to judge each CME with an unbiased approach. However, the quality of the images can limit inspection accuracy to an extent. In some cases, this could be a potential source of error because of low resolution images and the minute nature of the filament structures.

Previous studies such as Yurchyshyn et al. (2007) have utilized methods in which the angle of the axial field directions were determined. However, with this study and Aparna & Martens's earlier study, we can conclude that analyzing the north and south orientation of filaments and Bz signatures is adequate as a first measure in preparing for an impending geomagnetic storm. To favor the north-south approach further, we note that in the case of severe geomagnetic storms in the past, such as the Halloween Storms of 2003, as mentioned in Balch et al. (2004), some of the CMEs that were found to correlate to the disruptions in the Dst (largely negative) arose out of events with

Table 3.1: Results of the comparison of the vertical component of the filament axial magnetic field and its corresponding IMF Bz. North and South in the top row corresponds to the filament field, and those in the first column correspond to the IMF Bz. The NS IMFs (Bz along east-west direction) are not included in the agree or disagree counts between the two and are counted separately (see section 2). Note that the term NS is assigned generically and does not imply that north was leading the south.

	Filament	
IMF Bz	North	South
North	40	13
South	18	26
NS	3	2
Agree	66	65%
Disagree	31	30%
Total	102	

Table 3.2: Categories of the total Halo-CME data based on determined and non-determined events.

Those that have been determined:	102
Cannot be determined due to absence of filament axis (but Bz is present):	22
Cannot be determined due to absence of Bz (but filament is present):	27
That are backside:	71
That have not been determined:	78
Limb 90°:	93
Total	393

filaments with a southward axial field direction. For example, an event that occurred on October 28, 2003 in our catalog was observed to have a southward axial field direction, and several subsequent events originated from the same region. The Bz and Dst dropped to extremely low values a few days after, giving strong evidence that the events that occurred on 28 Oct and henceforth were responsible for the storms. In conclusion, our method of comparing the axial field direction component of CME source regions to corresponding IMF Bzs with about 21 years of data together with AM20, has shown that it can be used as a first step to effectively eliminate those cases that will not cause geomagnetic storms, thus reducing the number of times precautionary measures need to be taken to minimize impact on economic and data losses.

Date	EW IMF	Source Location	Chirality	Barbs	Arcades	Fibrils	Space Speed	Arrival (days)	Bz
1997/02/07		S38W31	sinistral		S		584	3.01	S
1997/05/12		N21W08	dextral	N			749	2.35	S
1997/07/30		N42W10	dextral			N	129	13.6	S
1997/10/21		N16E07	dextral	N			805	2.18	N
1997/11/04	Yes	S14W33	sinistral		N		993	1.77	NS
1998/01/25		N21E25	dextral		N		888	1.98	N
1998/04/29		S18E20	sinistral		S		1655	1.06	S
1998/05/02	(no)	S15W15	sinistral	S			1168	1.51	S
1998/11/05		N19W10	dextral		N		624	2.82	N
1998/11/05		N22W18	dextral		N		1335	1.32	N
1998/11/07		N22W42	dextral		N		733	2.40	S
1998/12/18		N19E64	dextral		N		1799	0.98	N
1999/05/03		N15E32	dextral	N			1824	0.96	S
1999/06/12		N27W43	dextral	N			546	3.22	N
1999/06/23		N23E42	dextral		S		1097	1.60	N
1999/06/24		N29W13	dextral	N	N		1143	1.54	N
1999/06/29		S14E01	sinistral		S		901	1.95	N
1999/06/30		S15E00	sinistral		S		746	2.36	N
1999/09/20		S20W05	sinistral		N		900	1.95	S
2000/02/17		S29E07	sinistral		N		973	1.81	N
2000/04/04	Yes	N18W55	dextral		S		1217	1.44	NS
2000/06/06	Yes	N20E18	sinistral		N		1348	1.30	NS
2000/06/07		N23E03	dextral		N		1208	1.46	N
2000/06/10		N22W38	dextral	N			1228	1.43	N
2000/07/07		N04E00	dextral		S		766	2.30	N
2000/07/25		N06W08	dextral		S		900	1.95	N
2000/08/09	(no)	N20E12	sinistral		S		1007	1.75	S
2000/09/12		S19W06	sinistral	N	N		1946	0.90	N
2000/09/16	(no)	N14W07	dextral	N			1568	1.12	S
2000/11/01		S17E39	sinistral		S		960	1.83	S
2000/11/24		N20W05	dextral	N			1611	1.09	N
2000/11/24		N22W07	dextral		N		1532	1.15	N
2000/11/24		N21W14	sinistral		N		1222	1.44	S
2000/11/25		N18W24	sinistral		N		903	1.95	N

2000/11/25		N20W23	dextral		N		893	1.97	N
2000/12/18		N15E01	sinistral	S			810	2.17	S
2001/01/10		N13E36	dextral	N			1030	1.71	N
2001/01/20		S07E40	sinistral		N		1017	1.73	N
2001/03/19		S20W00	dextral	S			2711	2.69	S
2001/03/24		N15E22	dextral		N		903	1.61	N
2001/03/28	(no)	S10E30	dextral		S		893	2.22	S
2001/04/06		S21E31	sinistral		S		1017	1.73	N
2001/04/09		S21W04	sinistral		S		1089	2.30	N
2001/04/10		S23W09	sinistral	S	S		1233	1.12	S
2001/04/26		N20W05	dextral	N	N		653	1.34	S
2001/08/14		N16W36	dextral	N	N		1093	1.61	N
2001/09/11		N13E35	dextral	N			792	2.22	N
2001/10/09		S28E08	dextral		S		1156	1.52	N
2001/11/03		N04W20	dextral			N	763	2.30	S
2001/11/22		S17W36	sinistral	S			1577	1.12	S
2001/11/28		N04E16	sinistral	N			894	1.97	N
2001/12/13		N16E09	sinistral		S		1315	1.34	N
2002/03/15		S08W03	sinistral		N		1297	1.36	N
2002/03/18		S10W30	sinistral		S		1223	1.44	N
2002/03/20		S17W20	sinistral		N		838	2.10	S
2002/04/15		S15W01	sinistral		N		1143	1.54	N
2002/04/17		S14W34	sinistral		N		1417	1.24	N
2002/05/16	(no)	S23E15	sinistral		N		823	2.14	S
2002/05/22		S30W34	sinistral	S		S	1718	1.02	S
2002/09/05		N09E28	dextral		S		2074	0.85	S
2002/11/09		S12W29	sinistral		S		2159	0.81	N
2002/12/19		N15W09	dextral			N	1392	1.26	N
2003/05/27		S07W14	sinistral		N		802	2.19	N
2003/05/27		S07W17	sinistral		N		1222	1.44	N
2003/05/28		S07W20	dextral		N		1701	1.03	N
2003/05/31		S07W65	dextral		N		1888	0.93	S
2003/08/14	(no)	S10E02	sinistral		S		766	2.30	S
2003/10/28		S16E08	dextral	S			3128	0.56	S
2003/11/18		N00E18	sinistral		S		2109	0.83	S
2004/01/20		S13W09	sinistral		N		1248	1.41	S
2004/01/21		S19E29	sinistral		N		975	1.80	N

2004/04/08		S15W11	dextral		N		1352	1.30	N
2004/07/20	(no)	N10E35	sinistral		S		892	1.97	S
2004/07/25	(no)	N08W33	sinistral		S		1544	1.14	S
2004/09/12		N03E49	sinistral		S		1436	1.22	N
2004/11/04		N09E28	dextral		S		877	2.01	S
2004/11/06	(no)	N09E05	dextral		S		1388	1.27	S
2004/11/07		N09W17	sinistral		S		2218	0.79	S
2004/11/10		N09W49	sinistral	S			3656	0.48	N
2004/12/03		N08W02	dextral		N		1652	1.06	N
2004/12/30		N04E46	dextral		N		1132	1.55	N
2005/01/01		N03E33	dextral		S		1076	1.63	N
2005/01/05	Yes	N15E15	dextral	S			1081	1.63	NS
2005/01/15		N16E04	dextral		N		2701	0.65	N
2005/01/15		N15W05	dextral		N		3682	0.48	N
2005/01/17		N13W19	sinistral		N		2580	0.68	N
2005/01/17		N15W25	dextral		N		3029	0.58	N
2005/01/19		N15W51	sinistral		N		2178	0.81	N
2005/01/20		N14W61	sinistral		N		951	1.85	N
2005/05/06		S07E28	dextral	S			1342	1.31	S
2005/05/13		N12E11	dextral		N		2171	0.81	N
2005/05/26		S11E19	sinistral	N			854	2.06	N
2005/07/07		N09E03	dextral		S		1173	1.50	S
2005/07/09		N12W28	dextral		S		1818	0.97	S
2005/07/12		N09W67	dextral		S		544	3.23	N
2005/08/22		S11W54	sinistral		S		1265	1.39	S
2005/08/23		S12W70	sinistral		S		1929	0.91	N
2005/08/31		N13W13	dextral		S		1283	1.37	N
2005/12/07		N15E13	dextral		S		1006	1.75	S
2006/05/01	Yes	S17W29	sinistral		N		674	2.61	NS
2006/07/06		S09W34	dextral		S		1043	1.69	S
2006/12/13		S06W23	sinistral		S		2184	0.81	S

Table 3.3: The table gives the Bz analysis for the determined set of the data. The first column shows the date of eruption, 2nd column says if it was an east-west (EW) ICME - (no) means that it has both positive and negative Bz in the profile, which is typical of an EW ICME, but one of them is dominant and hence is not classified as an EW ICME, 'Yes' means that the ICME is EW oriented and the corresponding ICME Bz is classified as 'NS' in the last column of the table, blank space means that it was not an EW ICME. The third column gives the chirality of the filament on the Sun; the 4th, 5th and 6th columns give the direction of the vertical component of the axial field of the region of eruption and the feature using which this and chirality were determined. The 7th column gives the speed of the CME which is used to calculate the arrival time given in the 8th column. And the last column gives the direction of the ICME Bz orientation.

Chapter 4

COMPARING CHROMOSPHERIC FILAMENTS AND CORONAL SIGMOIDS

The following work has been conducted in collaboration with Dr. Manolis Georgoulis, Academy of Athens, and will be a coauthor upon publication.

4.1 Introduction

Monitoring coronal mass ejections (CMEs) and solar flares occurring on the Sun is extremely important as humans venture into becoming a multiplanetary species, as a protective measure for astronauts on the spacecrafts on their journey to the Moon and Mars, from high-energy particles and electric grids and oil pipelines on the ground from induction of magnetic fields and overcharging of satellite electronics (Lam et al., 2012). The daily lives of human beings depend on the above said facilities and must be well protected for their uninterrupted functioning. A few methods currently used for CME and flare predictions are mentioned in Chapter 1. There are higher chances of a solar flare or a CME occurring from an active region than from a quiet region (Hazra et al., 2020), hence active regions are the focus of the prediction efforts for most models and observations. In this study, we focus on the sources of strong solar eruptive events - sigmoids, and their relation with their counterparts seen in chromospheric wavelengths - the filaments, to understand if and how they can be used for space weather event predictions.

Sigmoids are found in complex active regions (ARs) consisting of two or more sets of sunspots often containing a flux rope like twisted structure (Titov & Démoulin, 1999; Tripathi et al., 2009) in the corona. They appear to take the shape of a forward ‘S’ or an inverse-S, resembling a ‘Z’. They make large observable features on the disk of the Sun and are usually seen in soft and hard

X-rays, and short extreme ultraviolet (EUV) wavelengths. S and inverse-S shaped sigmoids take their shape based on the twist in their topology, and are often indicated by right and left handedness, respectively. Twisting in magnetic structures often leads to eruptions on the Sun due to development of instabilities (Cheung & Isobe 2014 & references therein) and can be measured by a quantity known as Helicity useful for4 estimating when an eruption might occur. Helicity is a conserved quantity giving a measure of the amount of twist and writhe in the structure. Twist refers to the twisting of the field lines about the axis and writhe refers to the axis coiling around itself (Berger & Field, 1984; Martin et al., 2012). In EUV and soft X-ray observations, sigmoids are also often seen with anti-parallel J-shaped bright structures that converge along and on the opposite sides of the polarity inversion line (PIL) (Kliem et al., 2004; Pan et al., 2022). The J and S shapes of the sigmoids indicate impending eruptive after their formations; some studies have observed the formation of J-shaped loops prior to the formation of S-shaped contiguous structure followed by an eruption (Liu et al., 2010). In McKenzie & Canfield (2008)'s study the S-shape of the sigmoid disappeared after an eruption, however it is known to reform in cases of partial eruptions (Gibson et al., 2006a,b). Sigmoids in simulations are usually represented with a flux-rope morphology with magnetic field lines forming a number of turns with the field lines rising towards the corona, turning and then dipping down close to the photosphere and rising again. An example of a sigmoid in soft X-rays taken using the Hinode spacecraft (Kosugi et al., 2007) is shown in Fig. 4.1. The bright arcs seen in the sigmoids represent hot current sheets of plasma that form among the dipped magnetic field lines. Gibson et al. (2006a) suggest that the observations show the dipped parts of the sigmoid flux ropes as those are the regions that tend to give rise to electric current sheets due to the development of tangential discontinuities in the magnetic field and the plasma reaching high enough temperatures to emit in X-ray wavelengths.

Kusano (2005) suggests that sigmoids spontaneously form in regions where there is a shear inversion layer, via a chain reaction of reconnections between oppositely directed field lines. This reaction is called the resistive tearing mode instability and occurs due to an increase in electric current in the shear layer. Alternatively, Fan & Gibson (2003) suggested the possibility of sigmoids

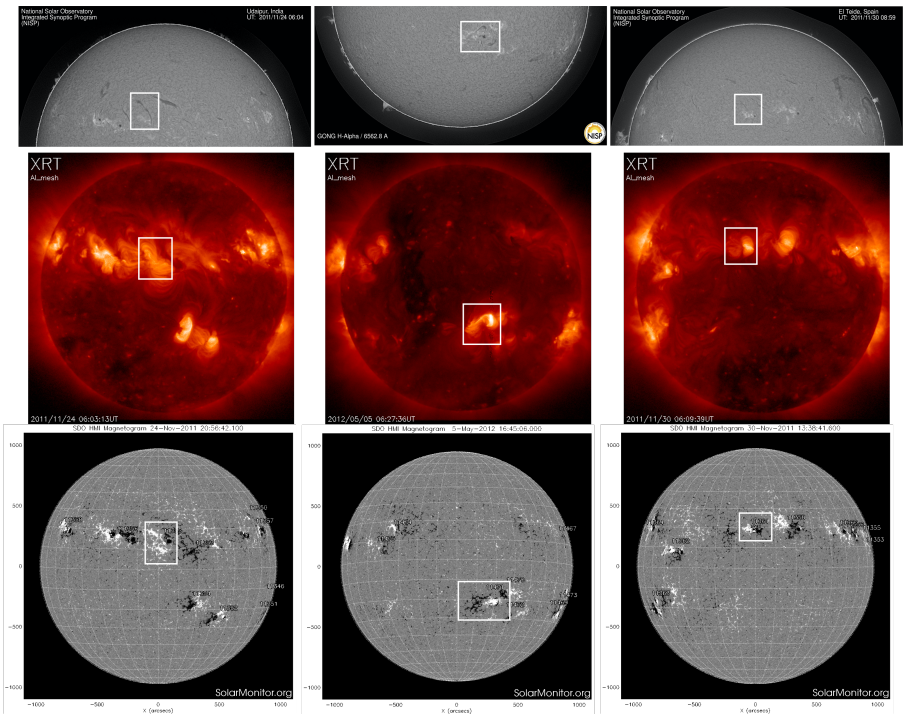

Figure 4.1: Selected sigmoids from the catalog with their filaments and the line of sight magnetogram.

emerging from below the photosphere already having an S or an inverse-S shape. They use this as a starting point in their models to study how the sigmoids evolve and produce eruptive events. Importantly, they show that the structure of the electric current density or the current sheets in their sigmoid region to be concentrated at the PIL taking an inverse-S shape. Although the current sheet is shown to be continuous and the sigmoid emerges as one flux tube in these simulations, high resolution observations show that they are made of multiple hot plasma features (Glover et al., 2000; Archontis et al., 2009) including short J and long S shaped ones.

Sigmoids can be further classified as transient and long-lasting (several days) depending on the duration of their existence. Transient sigmoids are short lived, they often lose their S or Z shape post an eruption commonly developing a cusp like shape as a result of opposite field lines coming close to reconnect leading to an eruption (Glover et al., 2000; Török & Kliem, 2005; Gibson & Fan, 2006). Recently, Vasantharaju et al. (2019) observed the formation of the cusp shape during a CME eruption in Atmospheric Imaging Assembly (AIA) 171Å channel. Sigmoids may retain their S or Z

shapes even after an eruption suggesting that the current sheet still remains and may lead to more eruptions. Long lived sigmoids continue to exist on the solar surface for a few days to almost half a rotation giving out multiple flares during their existence.

Sigmoids have been widely studied because of their complex active region morphology and their propensity to flare (Canfield et al., 1999; Sterling, 2000). A statistical study conducted by Canfield et al. (1999) involved categorizing ARs into sigmoidal and non-sigmoidal types with eruptive and non-eruptive region in each type. Overall, 51% of the 117 ARs they studied are sigmoids and 65% of the total eruptions occurred from sigmoid-eruptive regions. They also categorized the ARs by area and found that small sized sigmoids are non-eruptive compared to larger sized ones, but still they were eruptive compared to non-sigmoid-non-eruptive regions. Glover et al. (2000) utilized higher resolution SOHO/ EIT (Solar and Heliospheric Observatory/ Extreme-ultraviolet Imaging Telescope; Delaboudinière et al. 1995) and LASCO (Large Angle and Spectrometric Coronagraph; Brueckner et al. 1995) data for some of the sigmoids that overlapped with the dataset from Canfield et al. and reclassified their sigmoid-eruptive regions into sigmoid, non-sigmoid and ARs that appeared like sigmoids due to projection effects. After re-classification, their results, although only 17 cases in total, showed that eruptive events were more commonly associated with sigmoid regions in comparison to ARs that looked like sigmoids and non-sigmoidal ARs.

Later on, Canfield et al. (2007) studied 107 ARs determined by them as sigmoids and obtained field directions via potential field extrapolations of the sigmoids at heights of 0.4-0.8 $R_{\odot}$ and that of the overlying arcade field at 2.5 $R_{\odot}$ to observe if they match in their magnetic field directions. They found parallel and anti-parallel configurations between the two heights and found that the ones that had anti-parallel configurations flared almost twice as much as the ones with parallel configurations. They suggest that the higher flaring in anti-parallel configurations is due to the overlying field interacting with the sigmoid field via breakout reconnection (Antiochos, 1998) which is more efficient compared to tether-cutting reconnection (an example is shown in Aparna & Tripathi 2016) which they suggest is the possible mechanism in action in cases with parallel configurations.

More recently, in a statistical analysis of eruptive event occurrence in sigmoids, Kawabata et al. (2018) observed that only a very small number ($\sim$9%) of CMEs were not associated with a sigmoid region and that “sigmoid structures have a stronger dependence on CME occurrence than large X-ray flares". Sigmoids produce a large number of eruptive events (Canfield et al., 1999; Sterling, 2000; Savcheva et al., 2014; Kawabata et al., 2018) which may potentially affect our technology dependent systems. It would be beneficial to understand if they can be utilized in association with solar filaments, for the reasons explained below, for predicting if an eruptive event produced from a sigmoid will affect the Earth’s magnetosphere. Furthermore, if sigmoids were to be as predictive as filaments, the fact that sigmoids are large observable features on the Sun would make it easier to use them for predictions by automated algorithms.

Solar filaments are dark structures seen commonly in absorption in Hα, He 10830Å, Ca II H & K and other chromospheric wavelengths. They are cool plasma of around 10,000 K suspended in magnetic dips at coronal heights, seen in emission when at the limb and are called prominences. Filaments are often situated inside flux ropes, in other words, flux ropes wind around the filaments (van Ballegooijen & Martens, 1989) where the filament mass is supported. In white light limb images of CMEs in the corona, prominences are seen as bright features at the bottom of the “cavity" region (Gibson et al., 2006b), which is a dark region devoid of electrons required for scattering the photons, above which there is an expanding loop of the CME corresponding to the overlying arcade loops seen on the disk with the cavity being the flux rope encompassing the filament/ prominence. The bright prominence, dark cavity and the overlying loops together form what is known as the three-part CME structure (Riley et al., 2008) often seen during CME eruptions at the limb. On the disk, filaments appear to be made of threads of magnetic field lines along which plasma is observed to flow back and forth (Zirker et al., 1998; Litvinenko, 2021). They always form above the neutral line or the PIL. Filaments are categorized into quiet region, intermediate and active region filaments depending on where they occur (Engvold, 1998). Quiet region filaments can be long and long lived compared to active-region (AR) filaments which are often short and eruptive. Quiet region filaments are often found with distinguishing structures known as barbs that extend

out of the central long structure called the spine. In AR filaments, the barb structures are usually absent. However, in all filament kinds, the fibrils that make up the adjacent spaces of the filament neutral line, follow along in a certain direction. Similar to sigmoids having a handedness, filaments also have a twisting direction knows as chirality. Filaments have left or right handed chirality when the adjacent fibrils bend towards the left or right, respectively. Barbs if present also show a similar feature. The chirality of filaments is governed by magnetic field, hence following along the fibrils by knowing the magnetic polarities from where they originate, can be used for obtaining the directionality of magnetic field along the filaments. This is important for space weather prediction purposes because CMEs are commonly seen with filaments in their cavities and the directionality of the filament axial magnetic field plays a determining role in whether the CME will reconnect with the Earth's magnetic field to cause a geomagnetic storm or not. The two previous chapters mainly talk about how filament magnetic field direction prior to an eruption relate to that in CMEs near the Earth. Using data sets from different years, previous works such as Burlaga et al. (1981); Bothmer & Schwenn (1998); Marubashi et al. (2015); Palmerio et al. (2018) and Nieves-Chinchilla et al. (2019) have indicated in essence that the axial field direction is retained during their post eruption travel from the Sun to the Earth. Our previous works - Aparna & Martens (2020) and Mundra, Aparna, & Martens (2021) build up on these and use the largest data set of CME magnetic clouds (MC) near L1 Lagrangian point and filament counterpart of the CMEs on the Sun. Our data sets cover almost two solar cycles from 1996 to 2017. We find that in about 75% of the cases, the axial field direction is retained between the Sun and the Earth indicating that observing the filament magnetic field direction can help predict if a CME from the filament will or will not affect the Earth's magnetosphere. In both our studies, we have used filament chirality to find the axial field directions. The first aim of the current work is to identify if a consistent relation exists between the handedness of the sigmoids and the corresponding filament chirality. If there exists such a relation, sigmoids which are large and relatively easily discernible features as compared to AR filaments, which are often small with unresolvable fibrils, can be utilized for predicting the directionality of CMEs that were to occur from these sigmoids. We also analyse the hemispheric

helicity preference of the sigmoids and filaments. The shape of the sigmoids in general complies with the hemispheric helicity rule. Chromospheric filaments while erupting, also take on a rotational direction in compliance with the hemispheric preference (Green et al., 2007; Zhou et al., 2020).

Our second aim of the paper is motivated by the results of the first part which suggests that there is no consistent correlation between filament chirality and sigmoid handedness. In the second part, we explore how the handedness or helicity sign in the sigmoid structure is different or similar with that at the photosphere and filaments. We use the sigmoid handedness to visually determine the helicity sign in the corona, the chromospheric filament chirality to determine its helicity sign in the chromosphere, and we use calculations performed using the energy-helicity code by Georgoulis et al. (2012), to get the helicity sign of the sigmoid region at the photosphere. We find that the photospheric helicity sign matches sometimes with that of the filament and sometimes with that of the sigmoid. The filament resides over a narrow region called the PIL whereas the sigmoid encompasses the entire active region. We conjecture that due to the proximity of emerging magnetic fields near PILs, there is dominance of opposite helicity compared to that in the volume of the sigmoid and perhaps why sometimes the sigmoid helicity sign is oppoite to that of the filament.

The chapter is organized as follows. We first discuss the data and analysis methods used for two aims of this work in section 4.2. Then we discuss the results from the analysis of the first aim, then we discuss the results of the analysis of the second aim in section 4.3. We conclude with some discussion in section 4.4 .

4.2 Data and Analysis

4.2.1 *Chromospheric Filaments and Coronal Sigmoids*

Out first aim is to identify X-ray sigmoids with their chromospheric filament counterparts and compare their helicity and chirality signs. For quick reference, we give a mapping between chirality and helicity signs in Table 4.1. To compare the two signs, we have built a dataset consisting of chromospheric Hα filaments and coronal soft-Xray sigmoids from 2007 to 2017 containing their chiralities and helicities. A similar analysis was conducted by Martens et al. (2014) for sigmoids

and filaments between Oct 2010 and Mar 2011. Our list of the sigmoids is obtained from Savcheva et al. (2014)[1] and their continued analysis of sigmoid detection and measurements from 2013-2017[2]. Their data is available until 2017. To obtain the chirality of the filaments, we mainly use GONG Hα images and Kanzelhöhe Solar Observatory (KSO, Pötzi et al. 2015) Hα images in a few cases where GONG data was unavailable. Using these images, we visually determine the chirality of filaments and the shape of the corresponding coronal sigmoids using daily images from the Hinode XRT sigmoid calendar[3] obtained from the X-Ray Telescope onboard the Hinode spacecraft (Golub et al., 2007). The chromospheric filaments lie within the region of the coronal sigmoids on the PILS. We use the images of Hinode XRT sigmoids from the days when they are detected in Savcheva et al.'s catalog while the chirality of the filaments is also analysed for the day of the sigmoid detection. We obtain the chirality of filaments using the methods described in Martin (1998b), mainly using filament barbs and fibrils adjacent to the filaments. The method is described in Chapters 2 and 3. Chromospheric filaments from the same region but on a different day are used for obtaining the chirality if the filament features such as barbs and fibrils are not clear on the day the sigmoid feature is observed. Here we make an educated assumption that the field configurations do not reverse and that the filament in the same active region on a different day will have the same chirality as that on the day the data is missing or blurry.

Ouyang et al. (2017) have performed an extensive statistical analysis of filaments and suggest that Martin's chirality method only applies when a region is in the inverse polarity configuration (Kuperus & Raadu, 1974), and while in a normal polarity configuration (Kippenhahn & Schlüter, 1957), they are mainly shear dominated and Martin's rule applied to normal polarities will give a chirality opposite to the actual one. However, it is historically known that normal polarity filaments rarely form on the Sun. In their study, Ouyang et al. (2017) show that almost 89% of the 571 cases comply to inverse polarity. We have performed our analysis on the basis of Martin's chirality rules. According to Ouyang et al. (2017) and Chen et al. (2014), the chirality of filaments in the

[1] aia.cfa.harvard.edu/sigmoid/

[2] aia.cfa.harvard.edu/sigmoid23-24/sigmoid_webpage/

[3] http://solar.physics.montana.edu/HINODE/XRT/SCIA/latest_month.html

Filament Chirality	Helicity Sign	Sigmoid Shape	Overlying Arcade Skew
Dextral	− (Left)	Z	Left
Sinistral	+ (Right)	S	Right

Table 4.1: Quick lookup table to show the sign of filament chirality, corresponding helicity sign, and shape of the arcade overlying the polarity inversion line (see Martin (1998b)).

inverse-polarity models are opposite to that if they have a sheared-arcade configuration. However, we think that they both should give the same configuration and that only the filament-striations in the filament body are oppositely directed in each configuration (Martens & Aparna, in prep). Furthermore, owing to the negligible percentage of normal polarity regions, we do not expect our results to change significantly if we did consider the normal polarity regions in our data. Between 2007 and 2017, we have 85 sigmoids with filaments and the results for the handedness and chirality comparison are given in Table 4.2.

4.2.2 *EnHel*

Our second aim is to understand how the helicity sign of the local magnetic field varies at the photosphere in comparison to that of the filaments that form in narrow filament channels above the polarity inversion lines and in the coronal sigmoids obtained using visual methods described above. Thus we compare helicity signs of the observed sigmoid region using XRT data, chirality of filaments in the region above the PIL which is derived from Hα filament observations and the photospheric helicity sign which is obtained from calculations over the region of the sigmoid AR using photospheric vector-magnetograms. In order to understand how the helicity signs of the features at different heights behave, we use SHARP (Space-Weather HMI Active Region Patch; Bobra et al. 2014) vector magnetograms from the Helioseismic Magnetic Imager (HMI; Scherrer et al. 2012) onboard the Solar Dynamics Observatory (SDO; Pesnell et al. 2012) to obtain the helicity signs of the sigmoid region at the photosphere. We obtain the SHARP data formatted according to the Lambert Cylindrical Equal Area (CEA) projections of the magnetic field vectors from the JSOC database[4]. Using vector magnetograms as inputs we perform non-linear force free

[4]http://jsoc.stanford.edu/

(NLFF) approximations using the numerical code developed by Georgoulis et al. (2012) referred to as EnHel in this chapter, to get the sign and value of the force-free parameter α, for the sigmoid active regions at the photosphere.

EnHel uses all three magnetic field components derived from photospheric vector magnetograms (B_x, B_y and B_z) either in Cartesian or polar coordinate systems as input and calculates the energy and helicity budgets of a magnetically active region. The photospheric magnetic field corresponding to the entire active region corresponding to the coronal sigmoid is provided as input to EnHel. A description of how EnHel performs the energy and helicity calculations is given below. We compare the sign of the weighted-average of the force-free parameter obtained from EnHel with the helicity sign of the filament and that of the sigmoid both of which are obtained visually.

Georgoulis et al. (2012) or EnHel is a connectivity based model that can be used for both linear (Georgoulis & LaBonte, 2007) and non-linear force-free calculations to get the lower limit of the instantaneous energy and helicities of an active region using photospheric magnetic field as the lower boundary. They use a flux tessellation scheme based on Barnes et al. (2005) to build a connectivity matrix between the positive and negative polarity patches. To form the connectivity matrix, a minimum flux threshold, maximum number of pixels in each patch area and a certain vertical magnetic field strength are assigned to choose the patch areas. This is done so that it includes only the strong magnetic fields of the active regions and none from the quiet regions. This forms the flux patches that are connected by flux tubes, that are supposed to be slender, based on flux balancing between positive and negative flux patches. They use simulated annealing to optimize the area of these patches by minimizing the perimeter bounding the area of the patch. A connectivity matrix for the various flux patches is obtained using the force-free parameter α for flux-weighted value of α and its error for each magnetogram are calculated using the flux weighted average of the alpha values found for each connection. The equations for α and error in α are as follows.

$$\alpha = \frac{\sum_k \alpha_k \phi_k}{\sum_k \phi_k} \tag{4.1}$$

$$\delta\alpha = \frac{\sum_k |\alpha - \alpha_k| \phi_k}{\sum_k \phi_k} \tag{4.2}$$

The α_k and ϕ_k are the force-free parameters and the flux of each slender flux tube, respectively, connecting the patches in a magnetogram.

EnHel requires flux patch sizes, minimum flux and the magnetic field thresholds for the flux patches as inputs. We choose the minimum flux to be 5×10^{19} Mx and maximum patch size to be 30 magnetogram pixels per partition, magnetic field threshold as 50 G for B_z and use the NLFF approximations. For the sigmoids in our dataset, we consider the results for only those active regions with a flux balance better than 20%.

The list of our sigmoids with the properties derived visually as well as from EnHel are published at the Harvard Dataverse (Aparna, 2022). To save space, we present only a subset of these properties in the current manuscript in Table 4.4. It starts with the index and we give the date the sigmoid was detected from Savcheva's catalog in the second column, the third column gives the shape of the sigmoid, Z or S, followed by the helicity sign, + or -, respectively. The fifth column gives the chirality of the filament in the sigmoid region, L for left handed and R for right handed chiralities, followed by the helicity sign corresponding to the chiralities in the sixth column. S, N and A in the fifth column refers to small, no and ambiguous (chirality) filaments, respectively. The seventh column gives the flux-weighted α per mega-meter obtained from the EnHel code, followed by the standard deviation and the uncertainty in α measurement in the eighth and ninth columns.

Twist of a flux tube is a self-property showing rotation about its own axis (self-helicity) and mutual helicity is due to the interaction of adjacent, or winding, self-helical flux tubes. To obtain the number of turns in the sigmoids, we use the length of the sigmoid from Savcheva's catalog and multiply by the calculated alpha value, in the tenth column. The eleventh column gives the flux balance percentage. The table contains the list of sigmoids whose flux photospheric imbalance is less than 20%. The last column shows flare-index calculated based on the the number of flares from the respective sigmoid region. The flare records were obtained from the solar monitor[5] and the

[5] solarmonitor.org

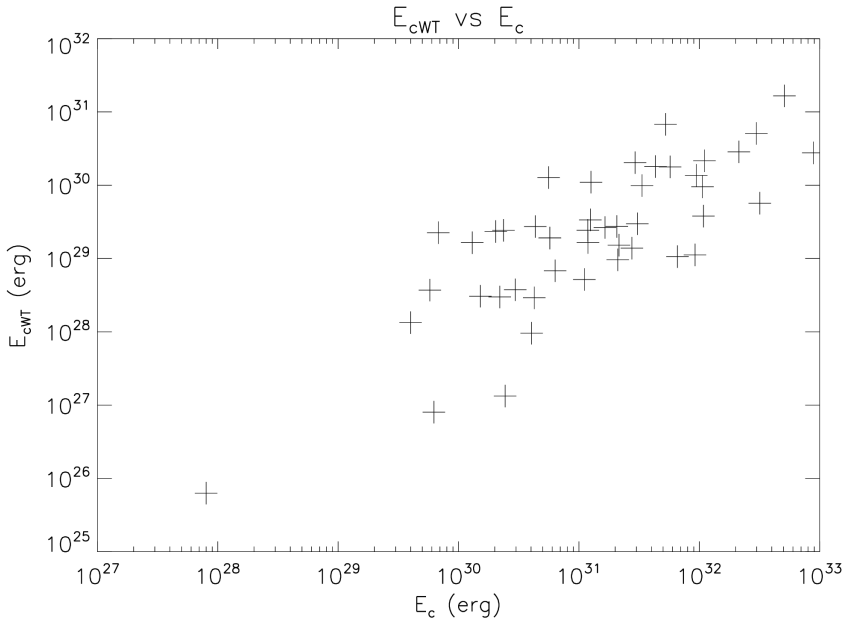

Figure 4.2: Free-energy distribution with reference to the Woltjer-Taylor minimum energy for the set of 46 sigmoids.

occurrences of CMEs were identified visually by overlaying AIA, HMI and LASCO C2 and C3 images using JHelioviewer (Muller et al., 2009) as well as using the CDAW halo-CME catalog[6] (Gopalswamy et al., 2009). Very few halo-CMEs have been recorded from these sigmoids. We have 46 sigmoids in our catalog that also have a chromospheric filament in them, however, five of these had filaments with non-detectable chirality. But we have run EnHel on all 46 of them and use them to show the results pertaining to helicity and energy. It was not feasible to run all the sigmoids for multiple days mainly because of computational time. As a sanity check for the calculations performed, we show a comparison of the calculated free energy with respect to the respecitve Woltjer-Taylor minimum energy in Fig 4.2 for the 46 sigmoids.

We perform EnHel calculations for each sigmoid for a one hour time period which gives us six helicity and energy values from the six SHARP vector magnetograms per hour and consider the maximum helicity and their corresponding energies from these values to conduct our analysis. In order to understand the relation between the sigmoids and their flaring propensity, we analyse the flares and CMEs that each of the 46 sigmoids have produced by obtaining their flare indices

[6]https://cdaw.gsfc.nasa.gov/CME$_list/halo/$

(Abramenko, 2005) using the following formula.

$$FI = \frac{100\sum_i X_i + 10\sum_j M_j + 1\sum_k C_k}{D} \tag{4.3}$$

Here, FI is the flare index, X_i represents the X-class flares, M_j M-class flares and C_k C-class flares that have occurred from a sigmoid region. The values of {1,10,100} are the weights given to {C,M,X} flares such that the flare index is in units of $10^{-6}Wm^{-2}Day^{-1}$. D is the number of days over which the flares are counted. For the sigmoids in our dataset, the flare index is calculated from the day after the sigmoid is detected until the AR remains on the disk. The flare indices are given in the last column of Table 4.4.

Some sigmoids are known to last for several days (Mulay et al., 2021) and some others are transient (Archontis et al., 2009) lasting from a few minutes to a few hours just before eruptions occur (Gibson et al., 2006a). Lastly, we choose one long-lasting sigmoid from Dec 2015 that lived on the disk for almost the entire time between the east and west limbs and perform EnHel calculations. We analyse how the sigmoid configuration may be related to the eruptive events it produces and how it might be related to the force-free values and the flux emergence. Our intention was to perform such calculations for multiple long-lasting sigmoids. However, due to a lack of such sigmoids that lasted for more than a few of days in this dataset, we defer this analysis to a future time. We give the results of the analysis from the two parts of our study in the results section below.

4.3 Results

The two main results of this work are summarized in the following subsections. Followed by the results, we give an account of the evolution of a persistent sigmoid.

4.3.1 *Relation between Filaments and Sigmoids*

1) From the first part of the analysis, we find that the chirality of filaments and the handedness of the sigmoids do not always have the same sign; a dextral filament can be present in an 'S' shaped

sigmoid and a sinistral filament may be present in an 'Z' shaped sigmoid. In other words the helical structures within a large scale sigmoid structure as seen in coronal X-ray and EUV wavelengths, may consist of small scale structures that are of opposite helicity. This implies that the shape of these large scale structures (sigmoids) cannot be used for determining the magnetic field direction and hence the Bz of ICMEs to predict space weather effects on the Earth's magnetosphere (Aparna & Martens, 2020; Mundra et al., 2021). However, this result has implications to monitoring these regions for space weather effects due to their flaring frequency as explained in the next point. This result also has implications for modelling of sigmoids consisting of emerging flux tubes that host prominences. Sigmoids are often depicted as twisted flux tubes models and if prominences are included, they often carry the same sign of the twist (Gibson 2018 and references therein). Although structures of twists with similar signs do exist as expected, and also according to our results, models of prominences with opposite twists must be explored for insights into stability of the magnetic structures and eruptive activities. The results of the filament chirality and the sigmoid helicities between 2007 and 2017 are tabulated in Table 4.2.

- There are 103 sigmoids in total from 2007 to 2017. Of these, 52 are forward sigmoids and 51 are inverse sigmoids. 41 of the forward and 44 of the inverse sigmoids have Hα filaments in them. Of these, 8 dextral filaments reside in forward sigmoids and 16 in inverse sigmoids and, 21 sinistral filaments reside in forward and 14 in inverse sigmoids.

- Of the 85 sigmoid cases with Hα filaments we analysed between 2007 and 2017, we find that 36% and 32% inverse sigmoids have dextral and sinistral filaments in them, respectively; and 20% and 51% of forward sigmoids have dextral and sinistral filaments in them, respectively. While, there is slight preference for dextral (sinistral) filaments to inverse (forward) sigmoids, from a space weather prediction perspective, owing to the lower percentages in either category which could lead to a higher rate of false negatives in predicting space weather effects, we conclude that a filament of either chirality could reside in a sigmoid of either shape. The remainder of the filaments, 29% and 32% in the forward and inverse sigmoids respectively, have ambiguous filament chirality. We note that higher resolution filament images from

Sigmoids → Filaments ↓	Forward (S) (41)	Inverse (Z) (44)
Dextral	8 (20%)	16 (36%)
Sinistral	21 (51%)	14 (32%)
Ambiguous	12 (29%)	14 (32%)

Table 4.2: Distribution of filaments and sigmoids according to chirality and shape respectively for data between 2007 and 2017. Reminding the reader that the expected configuration would be dextral (sinistral) filaments with inverse (forward) sigmoids. Ambiguous refers to the filament cases that were unable to be determined for left and right chiralities.

Goode Solar Telescope and the upcoming Daniel K. Inouye Solar Telescope (DKIST) will potentially improve the statistics of the result.

- 75% of the 85 sigmoids comply with the hemispheric preference while only 54% of the filaments follow the hemispheric preference.

4.3.2 *EnHel Results*

2) From the second part of the analysis involving EnHel, we use 46 of the 55 sigmoids selected for a run with EnHel between 2010 and 2017. Nine of them had a flux balance ratio much higher than 20%.

- Of the 46 sigmoids, 22 cases show a match in the helicity signs between two of the three α signs pertaining to photospheric calculations, chromospheric filaments and coronal sigmoids.
  - Of the 22, 9 cases have helicity signs that match between corona and the photosphere.
  - 13 of them have helicity signs that match between the chromosphere and the photosphere.
- Of the 46 sigmoids, 16 cases match in the helicity sign between the three types - filaments, sigmoids and EnHel calculations.
- Three of the 46 sigmoids have the same helicity sign between the corona and the chromosphere but the calculations show the opposite signs. We exclude these four sigmoids while comparing the flare outputs from the full-match and partial-match categories.

Purple Sigmoids ↓	N. Hem.	S. Hem.
Forward (S)	0	7
Inverse (Z)	7	2

Teal Sigmoids ↓	N. Hem.	S. Hem.
Forward (S)	5	6
Inverse (Z)	8	3

Table 4.3: Tables show the hemispheric preference for the sigmoids where the helicity sign is a match in all three heights (left) and those with that match partially (right). N. and S. refer to Northern and Southern hemispheres, respectively. According to the hemispheric preference, inverse (forward) sigmoids are normally observed in northern (southern) hemispheres.

- Filaments in five cases of the 46 sigmoids had unidentifiable chirality.

- For the cases where there is a match in helicity signs between all three features in the solar atmosphere, the hemispheric helicity preference holds in 14 of the 16 cases (88%). And for the cases where there is a match between any one of the atmospheric helicity signs (filament or sigmoid) and the EnHel calculations (photosphere), the hemispheric helicity rule holds only in 14 out of 22 cases (64%). The hemispheric preferences for these sigmoids are tabulated in Table 4.3.2. The names, Purple and Teal Sigmoids are based on the color coding for the respective sigmoid rows, those that match at all three heights and those that match the calculations with one of the heights, in the online data sheet in Harvard Dataverse (Aparna, 2022).

- From the cases with the matches between all three heights, the total number of flares produced is 57 from 16 regions, and 250 from 22 regions that matched only partially. The average being 3.5 per region from the former and 11.4 per region from the latter. There are considerably more flares when the helicity signs of sigmoids and their filament counterparts are opposite.

- In general, in the cases with all matches, 3 out of 16 ($\sim$19%) regions produced one CME each. In the cases where there is a partial match, 6 out of the 22 cases ($\sim$27%) produced one CME and the rest did not have any CMEs that were cataloged. In these cases in this dataset, the probability of CME production in the partial-match case versus full-match is about 1.5 times and that of flare production is about 3.3 times.

Following Fig. 2 from Tziotziou et al. (2012) we present the energy-helicity (EH) diagram for the sigmoids for our dataset in Fig 4.3. It plots the values of maximum magnetic helicity for the

available free energy in the time series of each sigmoid in logarithmic scale. Our sigmoids agree with the active region EH diagram from Tziotziou et al. in that the helicity and free energy are directly proportional to each other. The colorbar in Fig 4.3 indicates the flare index. There are around 28 sigmoids that produced no flares during the time considered for calculating the flare-index and those are shown with purple dots. The flaring regions are shown with various colors with red dots having the highest flare-indices. And similar to theirs, our EH diagram shows a segregation between flaring and non-flaring sigmoids with most of the flaring ones situated in the top right as opposed to non-flaring sigmoids towards the left. Their free-energy and total helicity cutoff for eruptive and non-eruptive ARs are 4×10^{31} erg and 2×10^{42} Mx^2, respectively. The sigmoids in Fig 4.3 somewhat agree with these cutoffs as well, although the region with the highest flare-index falls below these limits. Based on the distributions of the relative helicities and free-energies of the sigmoids, we obtain a threshold slightly less than the ones mentioned above, with a helicity of $1.1 \times 10^{41} Mx^2$ and an energy of 2.2×10^{31} erg. It is important to note here that the helicity and energy values are only representative as they are calculated at a certain time and flares produced after that are considered. A more accurate helicity-energy diagram would include values at several times over the time of the sigmoid, which will be attempted at a future time.

We also show an alternative energy-Helicity diagram in which the sigmoids are binned according to the number of flares they have produced. Specific to this data set, they have been binned into sigmoids producing zero flares, less than 12 flares, and those that produce more than 20 flares (there are no regions in the set that produce 13-20 flares). This diagram in shown in Fig 4.4 and shows the distinction between flaring and non-flaring sigmoids well. The flaring sigmoids are associated with higher energies compared to the non-flaring sigmoids. However, there are also flaring sigmoids with free energy less than the cutoff energy stated above. This seems to indicate that the helicity balance in the non-flaring sigmoids plays a role in the sigmoid not flaring. Further investigation with more examples or with models is warranted to understand if further increasing the free-energy without inducing helicity will lead to instabilities for the region to erupt.

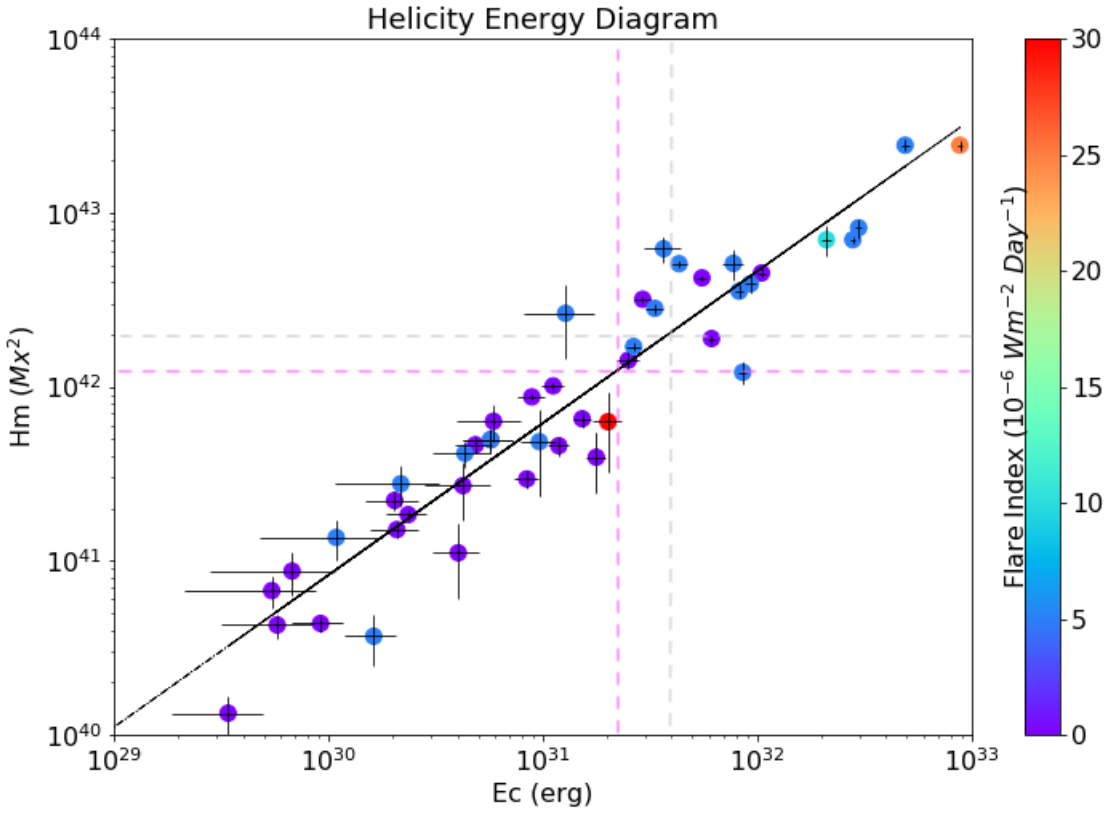

Figure 4.3: Logarithmic representation of the relation between relative magnetic helicity (Hm) and free energy (Ec) for the 46 sigmoids used for this study. The colors represent the flare indices as explained in the text. Grey dashed line correspond to the threshold from). Pink dashed line represents a chi-by-eye threshold for our sigmoids with $\sim 1.1 \times 10^{42} Mx^2$ for relative helicity and $\sim 2.2 \times 10^{31} erg$ for free energy.

Liokati et al. (2022) also studied evolution of energy and helicity in ARs for which they construct an EH diagram by selecting the values arbitrarily during the AR's flux emergence phase. Their cutoff for free energy (E_c) is 5×10^{32} erg and that for H_m is 9×10^{41}. These values are about five times higher than the free-energy cutoff from Tziotziou et al. and that for helicity is similar to the latter. We draw the cutoff lines at the same quantities as Tziotziou et al. in addition to that of our own. We do see that most of the sigmoids that produce more than 20 flares during their lifetimes fall below the cutoffs for E_c and H_m. All the sigmoids producing zero flares fall below either of the cutoffs.

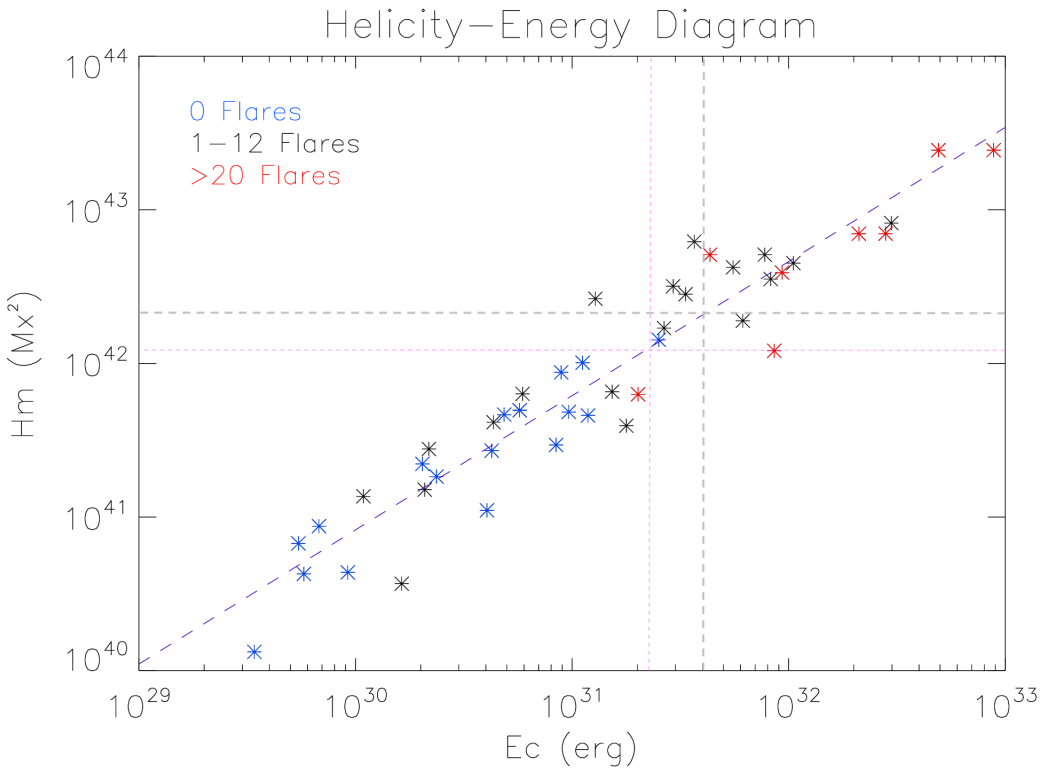

Figure 4.4: Same as Fig 4.3 but colors represent the number of flares each sigmoid region has produced.

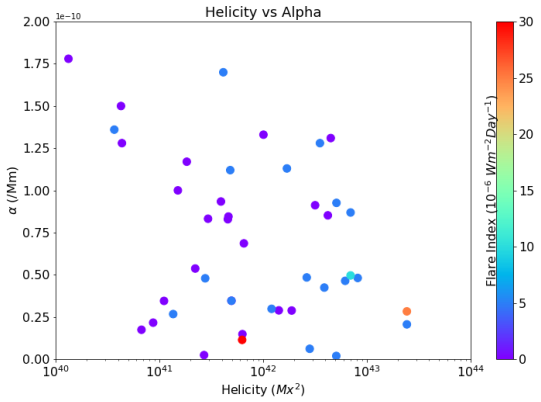

Figure 4.5: Distribution of helicity values for the 46 sigmoids versus their force-free parameters.

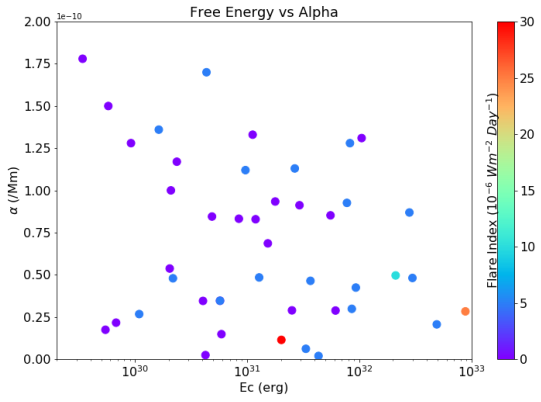

Figure 4.6: Distribution of free energy values for the 46 sigmoids versus their force-free parameters.

In figures 4.5 and 4.6, we show the helicity and energy values against the calculated absolute α values according to the flare index. The α values range between $\pm 2 \times 10^{-10} Mm^{-1}$. The distributions are fairly uniform between the sigmoids that give out different numbers of flares. Hence, the values of force-free parameter α does not indicate any flaring behaviour as zero flaring regions show both higher and lower α values.

Twisting a magnetic field stores energy and increasing the twist or shear will increase the energy which throws the balance by the ambient coronal field off, leading to an eruption. The twist in the field lines can occur because of rotation of sunspots (Török et al., 2004) leading to accumulation of energy in the corona. From modelling efforts, Kazachenko et al. (2009) observed that a 34 degree rotation of a sunspot leads to enough energy accumulation for an M8 flare. In Hu et al. (2014), the twist is larger in smaller flux ropes. They also observed that magnetic clouds associated with prominence eruptions have more twists than those without prominence eruptions. The amount of twist (turns) in the magnetic field lines depends on the magnetic flux or the alpha parameter derived from that and the length of the field line. Based on these and NLFFF extrapolations, Inoue et al. (2011) deduced that about half a turn (π) was sufficient for causing a flare, whereas using kink mode instability, Török et al. (2004) found a turn value of about 3.5π was necessary for triggering a flare. However, other than the twisting of the field lines, the initiation of an eruptive

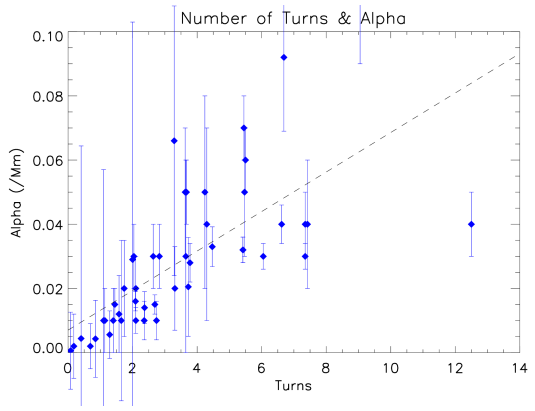

Figure 4.7: Relation between the force-free parameter and the number of turns for the set of 46 sigmoids. Values of α are absolute. The number of turns is a multiple of the force-free parameter and the length of the PIL of the sigmoid. The dashed line is the line fit for the distribution.

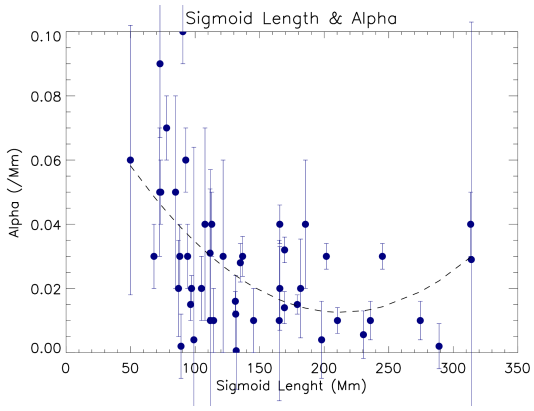

Figure 4.8: Relation between the force-free parameter and sigmoid length for the set of 46 sigmoids. Values of α are absolute. The dashed line is a second degree polynomial fit.

event also depends on conditions such as the presence of a larger-scale, overlying magnetic field that plays a role in the eruption process. For example, Török et al. (2004) showed that in ideal MHD (magnetohydrodynamic) simulations, a slow decrease in the field of the overlying magnetic field with increasing height from the PIL aids in stopping further development of the kink modes that leads to the eruptions.

We show the relation between the calculated number of turns and the sigmoid length with the force-free parameter in Figs 4.7 and 4.8, respectively. Figure 4.7 shows a linear relation between the force-free parameter which indicates how twisted a field line is, and the number of turns which is obtained by multiplying α with the length of the sigmoid (Savcheva et al., 2014). Figure 4.8 suggests that high values of α and high values of sigmoid length together are absent, possibly because increasing twists in long flux-ropes leads to instabilities and eruptions.

4.3.3 *Sigmoid of December 2015*

In order to further understand how eruptive events occur with changes in helicity and energy in the sigmoids, we perform EnHel calculations for one sigmoid from December 2015 that lasted on

the disk from the east limb to almost until the west limb. We give preliminary results from these calculations in this subsection. We expect to perform similar calculations on several long term sigmoids in the future and present it separately.

NOAA AR# 12473 is seen on the east limb first on 22nd of December 2015. It assumes the form of a sigmoid on as early as 23rd and survives almost until it reaches the west limb. It produces as many as 61 flares and six CMEs during this time. We perform EnHel calculations on the sigmoid region from Dec 23, 2015 until Jan 01, 2016 to understand how the changes in the energy and helicity contribute to the eruptive phenomena. The active region in its entirety is not visible outside of these dates. We rely on the CEA data of the Bx, By and Bz fields from SHARP vector magnetograms for all these dates to perform the calculations. The calculations are performed on every hour of each day except on Dec 27 when the data for the entire day is not available. We show the variations of the different parameters pertaining to the Dec 2015 sigmoid over the time of its existence on the disk of the Sun in Figures 4.9-4.13.

Figure 4.9 shows how the α parameter (open diamonds) varies over the period of the time the sigmoid is on the visible disk of the Sun facing the Earth. The purple curve through the diamonds represent the smoothing of the data series. The red lines connecting the abscissa represent the flares that occurred during a day with the number of flares given in the parentheses along the x-axis. Blue boxes represent a CME occurrence on the day, additional blue boxes represent CMEs on that same day from this region. The figure shows a large valley in the middle of the plot of the α series. Fourteen flares occurred prior to the decline of the α values. Eight flares occur during the descent or during the increase in the negative values of α. There is a data gap during Dec 27 after which there is a rise in the positive values of α and it continues to rise until Jan 01, 2016. Seventeen flares occur again during the rise phase of α post Dec 27.

The increase in the number of flares between Dec 25th and Dec 27th and the negative values of the α parameter may suggest emerging flux of opposite helicity or flux cancellation and hence a gradual change in the sign of the α values. Flares occur when opposite helicity structures come in contact with each other. This explains the higher number (8 and 17) of flares during the decline

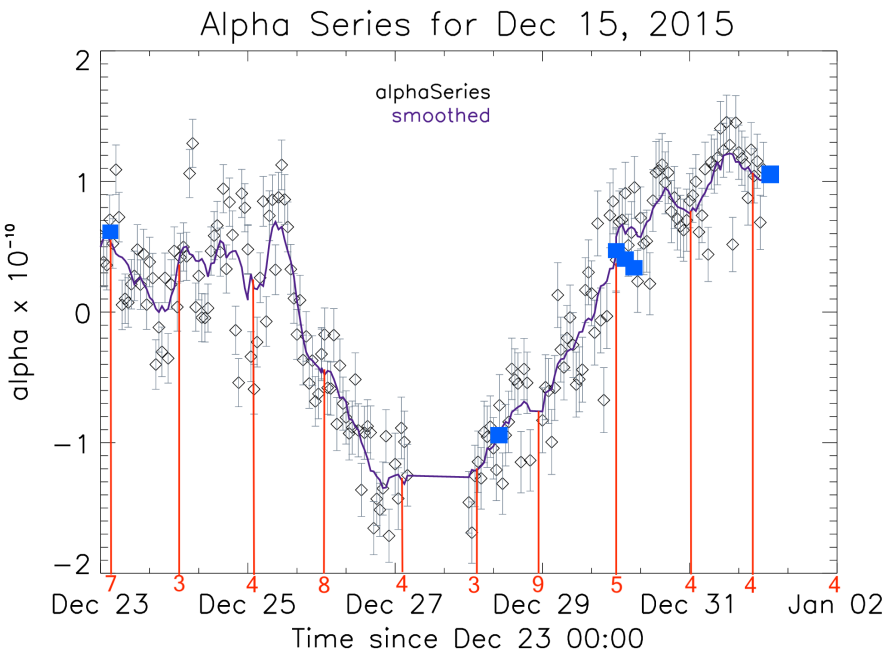

Figure 4.9: α value calculated every hour for the entire time the sigmoid was on the disk side facing the Earth. Red lines and the numbers below the lines represents the occurrence of flares and the number of flares during the respective days, respectively. Blue boxes represent the occurrence of CMEs.

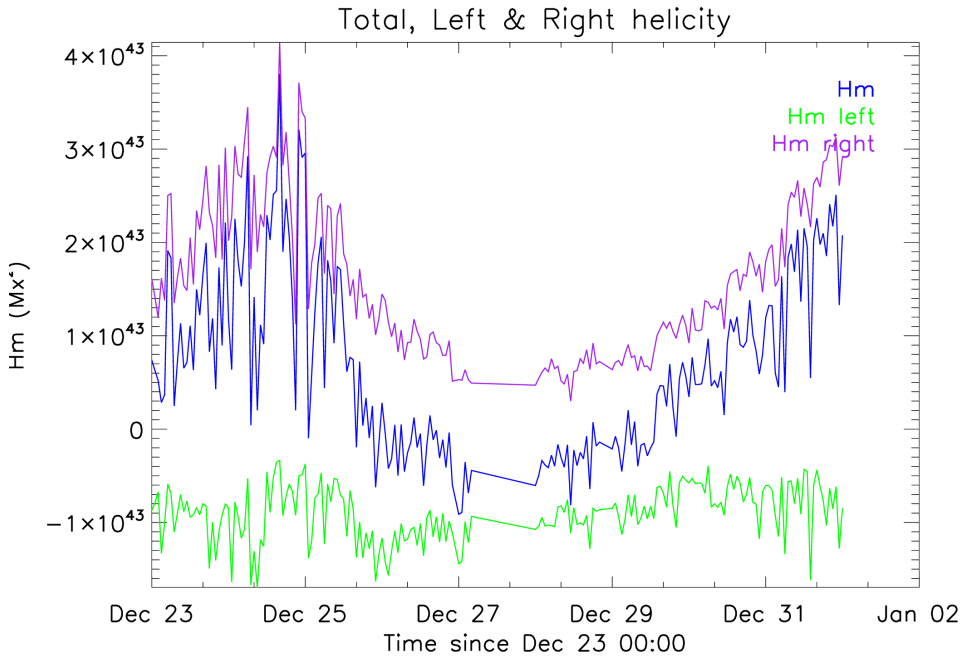

Figure 4.10: The variation of the total, left (negative) and right handed (positive) magnetic helicities over time for the sigmoid of December 2015.

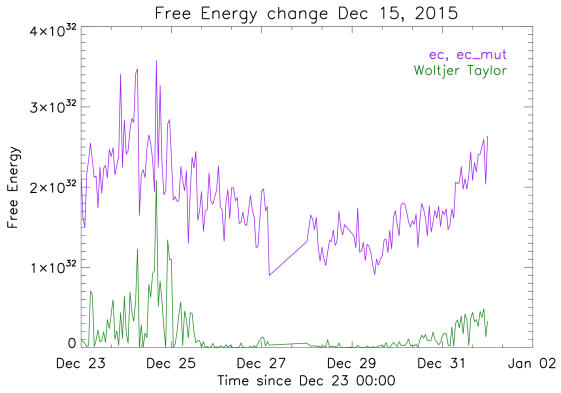

Figure 4.11: Changes in total free energy (purple) in comparison to the Woltjer-Taylor minimum energy (green).

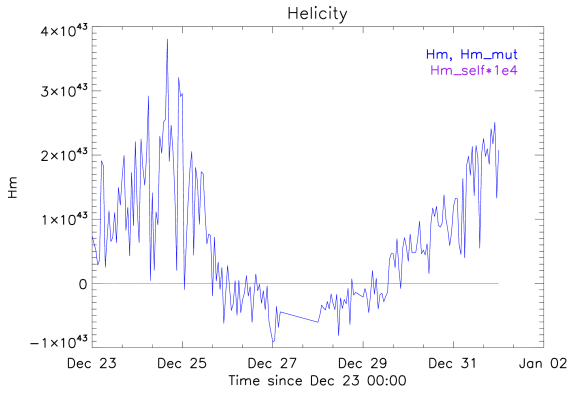

Figure 4.12: Variation of total/ mutual helicity for the sigmoid of Dec 2015.

and rise phases (respectively) of α in the plot. The changes in the negative and positive helicities can be seen in Fig. 4.10. There is an initial increase in positive helicity until Dec 25 followed by a reduction until Dec 27 after which it increases again. The left-handed (negative, green) helicity with variance 0.04 does not vary as much as the right-handed (positive, purple) helicity with a variance of 0.77, suggesting that the positive helicity is being changed rather drastically in the region of the sigmoid. Figures 4.13 shows the changes in the unsigned flux and in the positive and negative fluxes. The unsigned flux (in black) shows a gradual decrease between Dec 23 and Dec 27 and a rise after Dec 29. The negative (in blue) and positive (red) fluxes follow each other well, however, there is a higher rate of reduction in the negative flux compared to the positive flux between Dec 24 and Dec 26, indicating flux cancellation due to a higher rate of increase in the positive fluxes. The flux emergence continues to increase from Dec 28 until the end of the plot-time on Jan 01. The initial reduction in the fluxes, α and helicity indicate helicity annihilation (Kusano et al., 2004; Georgoulis et al., 2019) possibly triggering the flares between Dec 25 and Dec 27. The induction of helicity due to flux emergence in the rise phase between Dec 28 and Jan 01 also causes an increase in the eruptive activity.

Similar to the changes in positive, negative and total helicities in the sigmoid, the changes in energy values are shown in Fig 4.11. The Woltjer-Taylor minimum energy, which is the minimum energy that a magnetic field configuration can hold for a certain helicity (Kusano et al., 1995) and

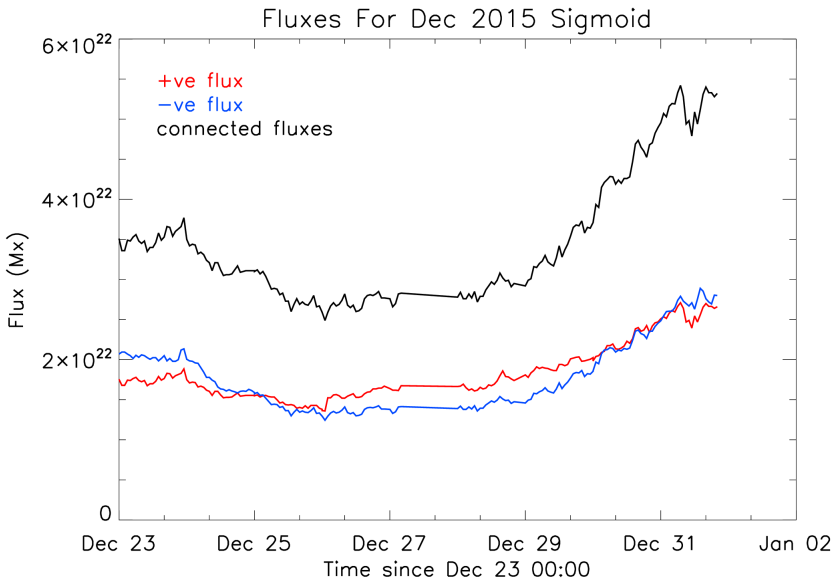

Figure 4.13: Changes in the positive, negative and the unsigned fluxes for the sigmoid of Dec 2015.

the mutual energy are plotted in green and purple, respectively. They have a very small variance compared to the total free energy. The changes in the free energy follows the trend similar to that seen in the changes in helicity.

4.4 Discussion and Conclusions

We have studied sigmoids on the Sun to understand the nature of their magnetic environment. The first part of our work focuses on comparing sigmoid handedness with the chirality of their filament counterparts. Because the polarity inversion lines of filament in the sigmoid is shared by the two features, it is expected that they show the same helicity signs. However, with a set of 85 sigmoids that hosted chromospheric filaments between 2007 and 2017, we show that a forward or an inverse sigmoid can host a filament of either dextral or sinistral chirality. See Table 4.2 for a detailed correlation of these features. Martens et al. (2014) obtain similar percentages for about six months of data. The filaments found in the sigmoids have a lower rate of compliance (54%) compared to their host sigmoids (75%) for the hemispheric preference. This result compares well with previous studies where by studying rotational direction of erupting filaments from sigmoid regions it has been

shown that both filaments and their sigmoids exhibit a forward S shape in the southern hemisphere and a reverse S shape in the northern hemisphere, indicating weak hemispheric preferences (HSP) (Zhou et al., 2020).

With increasing sophistication in numerical simulations that incorporate complex thermodynamic and radiative processes that can include prominences in flux-rope models (Fan 2018 and references there in), we believe that this result will be useful for simulations of emerging or coexisting opposite helicity structures to improve the understanding of eruptive phenomena. Recently, Fan (2017, 2018) have conducted 3D MHD simulations of flux-rope eruptions with prominence material playing the role of essentially stabilising the eruption until there is enough drainage of prominence mass when the upward Lorentz force takes over and the flux rope erupts. In addition to the promience mass, it would be interesting to incorporate the interaction of prominences of similar and opposite helicity to that of the sigmoid flux rope to understand how and when their interaction with the large scale sigmoid field will give rise to eruptions. We note that in the study by Fan (2018), the flux rope eruption in the absence of a prominence occurs rather quickly compared to when one is present. It would be of interest to study the flare productivity of sigmoids without a filament in the sigmoid catalogs to compare to those that do in this context.

In the second part of our study, we perform energy-helicity type surface calculations using the code developed by Georgoulis et al. (2012) and compare the calculated helicity signs of the photospheric sigmoid AR with that of the observed helicity signs from chromospheric filaments and X-ray sigmoids. We find that the helicity signs from filaments, sigmoids and the photospheric calculations from EnHel either match between all three cases (43% of the 37) and those that match either between sigmoid and EnHel or filaments and EnHel (57% of the 37). Altogether, the cases where there is a partial match produce about 3.5 times more flares than the cases with full match. The number of CMEs produced by the cases of partial match is about 1.5 times that produced by the cases of full-match. According to the HSP (Martin et al., 1994; Rust & Kumar, 1996; Liu et al., 2014), forward sigmoids are commonly seen in the southern hemisphere and inverse in the northern hemisphere of the Sun. From our results, in the latter case of mismatch, 8 out of 22 (38%) sigmoids

are observed to not follow the hemispheric rule and in the former case, 2 out of 16 (13%) do not follow this rule. Thus sigmoid active regions associated less with the HSP tend to flare more. This is perhaps because the twists of the emerging fields is opposite to that of the already existing field leading to magnetic reconnections causing eruptions (van Ballegooijen & Martens, 1989; Fan & Gibson, 2004).

We also obtain helicity and energies for 46 sigmoid regions using EnHel calculations. The distributions of these are shown in Figs 4.3 to 4.8. The energy-helicity diagrams shown in Figs 4.3 and 4.4 suggest a distinction between flaring and non-flaring sigmoid regions similar to that found by Tziotziou et al. (2012). Energy and helicity budgets are important quantities that determine whether an eruption will occur. Several authors consider CMEs as a way of removing helicity from the Sun (Rust & Kumar, 1994; Low, 1996; Pariat et al., 2006). Helicity accumulation is thought to occur with increase in twist which occurs as a result of flux emergence that injects helicity (Yang et al., 2009) or due to the dynamo and the Coriolis effect on an emerging flux-tube through the convection-zone of the Sun (Liu et al., 2016), which is released after a certain threshold is reached at which point the flux tube becomes unstable via kink instability or breakout model (Fan & Gibson, 2007; Priest et al., 2016). Various authors have calculated this threshold for active regions on the Sun. Nindos & Andrews (2004) using linear force-free models suggest that the force-free parameter α, prior to eruptions, to be lower in flares without CMEs as opposed to flares with CMEs. We do not however observe a trend in α with reference to the number of flares produced in the 46 sigmoids of our dataset.

Tziotziou et al. (2012) and Liokati et al. (2022) performed similar calculations as this work for active regions and found a threshold of 4×10^{31} erg, 2×10^{42} Mx^2 and 5×10^{32} erg and $9 \times 10^{41} Mx^2$ for energy and helicity, respectively. Our values for the sigmoids compare well with the former with a slightly lower thresholds of $2.2 \times 10^{31} erg$ and $1.1 \times 10^{42} Mx^2$ for energy and helicity, respectively. The regions that produce most flares fall on the higher ends of the helicity and energy range in the helicity-energy diagram (Fig. 4.3) and the ones that produce no flares fall on the lower ends.

We also perform EnHel calculations for the sigmoid of December 2015 (AR# 12473) that survives from east limb to west limb. In total, this region produced 61 flares and 6 CMEs. We observe the changes of flux, helicity and energy along with the twist factor for the sigmoid of Dec 2015, and correlate with the occurrence of the eruptive events. Helicity is thought to be transferred between magnetic structures in the form of twists and braids (Knizhnik et al., 2017) or bulk transfer via the Coriolis force that causes kinking (Liu et al., 2014); smaller field lines in the region can twist among themselves (Pevtsov et al., 2014) and can have opposite signs of helicities compared to the larger overall region. Kusano et al. (2004) suggested via modelling efforts that in regions of sharp reversal of helicities, which may occur due to new emergence of fluxes or due to twisting caused by footpoint motion of the magnetic fields, can get explosively cancelled due to resistive tearing mode instabilities and give rise to solar flares (Yokoyama et al., 2003), thus releasing the stored energy. From Figs 4.9 to 4.13 we observe that flux emergence occurs which introduces an opposite helicity to the already existing helicity and consequently a large number of flares occur. After this, the flux, helicity and the twist factors increase due to an increase in the flux emergence and produce more eruptive events and then gradually return to their previous states. Helicity induction followed by its cancellation indicates mechanisms such as the resistive tearing instabilities or helicity annihilation (Kusano et al., 2004; Georgoulis et al., 2019), might be in action. Further analysis using observations in EUV and X-ray at smaller scales near the PILs to verify these claims are warranted and will be partaken in the future.

From the results of part 1 of this study, we see that the chirality of filaments in our data does not correlate with the handedness of the sigmoids in the corona, suggesting that the helicity sign near the polarity inversion line is different from that at the outer regions. It is known that both positive and negative helicities are injected into the atmosphere from the convection zone (Gosain & Brandenburg, 2019) and the overall helicity is due to the summation of these helicities. However, any region has a dominant helicity and the observed structure (filament or sigmoid) usually depicts this dominant helicity via right or left handed curvatures or twists along the field lines, such as the S or Z shaped coronal sigmoids. Active region models developed by Bourdin et al. (2018) to study

how helicity changes occur with height suggest that helicity reverses going from the photosphere into the corona. Singh et al. (2018) used snapshots of coronal flux ropes to show that magnetic helicity reversal occurs within the corona due to the formation of bihelical field lines with opposite signs at different length scales. We believe that the sigmoid cases with partial match between the photospheric, chromospheric and coronal helicity signs conform to these models and the emergence of opposite helicity structures possibly the reason for higher eruptive activity compared to the cases with full match. Multi-height observations of filaments and flux ropes or loops at coronal heights and their magnetospheric counterparts using DKIST, Parker Solar Probe (PSP) and Solar Orbiter (SolO) to verify our results would be beneficial.

In conclusion, we think it is worth understanding the difference in the helicity and energy budgets for flares and CMEs separately and together. The occurrence of flares and CMEs is directly related to the amount of energy and helicity stored in them and each of these phenomena affect the Earth's magnetosphere somewhat differently, with flares contributing to particle effects on satellites in space and flights with trajectories near polar latitudes, and CMEs disturbing the magnetosphere causing induced currents in electric grids and oil pipelines. Flares and CMEs do occur together and knowing the trends in energy, helicity and other magnetic parameters in active regions will help in improving predictive capability of space weather effects. From our results from comparing the sigmoid handedness and filament chirality with each other and with the photospheric values, it is clear that features with opposite helicities existing together are prone to high eruptive activity and must be continuously monitored for improved space weather predictions.

#	Date	Sigmoid Shape	Helicity Sign	Filament Chirality	Helicity Sign	Alpha α/Mm	Std. Dev.	Uncertainty $\delta\,\alpha$	No. of Turns	Flux Balance %	Flare Index
1	5/4/10	Z	-	R	-	-0.09	0.02	0.09	6.69	9.2	0.0
2	7/15/10	S	+	L	+	-0.06	0.04	0.07	3.3	6.11	0.0
3	8/4/10	Z	-	R	-	-0.004	0.01	0.02	0.8	0.72	0.0
4	8/7/10	Z	-	R	-	0.03	0.006	0.02	2.7	11.8	0.0
5	12/1/10	S	+	N		0.004	0.06	0.02	0.4	4.3	0.0
6	12/10/10	Z	-	R	-	-0.02	0.01	0.02	3.7	0.61	0.33
7	4/10/11	S	+	N		0.02	0.01	0.03	1.7	1.57	0.0
8	9/13/11	Z	-	L	+	-0.0056	0.0074	0.04	1.3	6.21	0.73
9	11/24/11	Z		L	+	0.01	0.04	0.046	2.7	3.6	0.0
10	5/5/12	S	+	L	+	0.04	0.04	0.059	6.6	3.65	3.9
11	5/8/12	Z		L	+	-0.031	0.01	0.041	3.4	6.53	0.0
12	6/15/12	Z		L	+	-0.01	0.08	0.077	2.1	5.6	2.76
13	7/1/12	Z		R		-0.032	0.05	0.083	5.4	0.88	1.97
14	7/12/12	S	+	R		-0.016	0.05	0.067	2.1	3.9	20.1
15	10/21/12	S		R		-0.028	0.02	0.043	3.8	7.83	0.0
16	11/9/12	S	+	L	+	0.012	0.03	0.04	1.6	9.43	1.0
17	11/30/12	Z		R		-0.02	0.02	0.032	3.3	9.01	0.56
18	1/29/13	S	+	R	-	0.06	0.03	0.01	5.5	10.6	0.18
19	7/1/13	S	+	L	+	0.04	0.02	0.03	4.3	2.2	0.0
20	7/16/13	Z	-	N		0.03	0.05	0.01	2.04	8.7	0.0
21	8/8/13	S	+	R	-	-0.1	0.04	0.01	9.05	3.8	2.34
22	10/16/13	S	+	L	+	0.04	0.03	0.01	4.5	6.05	0.8
23	11/17/13	S	+	R	-	-0.03	0.05	0.004	7.35	12.25	5.0
24	11/20/13	Z	-	L	-	0.04	0.05	0.01	12.5	10.8	0.0
25	1/15/14	S	+	L	+	0.01	0.04	0.01	1.14	3.1	0.0

Table 4.4—*Continued*

#	Date	Sigmoid Shape	Helicity Sign	Filament Chirality	Helicity Sign	Alpha α/Mm	Std. Dev.	Uncertainty $\delta\,\alpha$	No. of Turns	Flux Balance %	Flare Index
26	3/26/14	S	+	R	-	0.002	0.04	0.01	0.18	3.6	29.33
27	5/1/14	Z	-	L	+	0.01	0.04	0.01	1.4	5.8	0.0
28	6/24/14	S	+	L	+	0.03	0.03	0.01	3.65	15.1	0.0
29	10/2/14	Z	-	R	-	-0.02	0.06	0.01	2.1	13.4	0.0
30	11/3/14	Z	-	L	+	0.07	2.34	0.01	5.45	7.6	0.0
31	11/12/14	S	+	L	+	-0.01	0.05	0.006	2.36	17.16	1.84
32	12/15/14	Z	-	L	+	0.04	0.04	0.02	7.42	15.3	0.26
33	2/22/15	Z	-	S		-0.03	0.05	0.01	2.83	17.1	0.0
34	9/1/15	Z	-	L	+	-0.05	0.02	0.02	3.63	3.87	0.0
35	10/21/15	S	+	R	-	-0.002	0.04	0.007	0.69	2.89	1.72
36	11/5/15	S	+	R	-	0.014	0.04	0.005	2.37	4.1	1.2
37	1/10/16	S	+	R	-	0.015	0.03	0.005	1.45	9.94	0.73
38	8/28/16	Z	-	R	-	0.03	0.04	0.01	2.64	9.79	0.0
39	9/19/16	Z	-	N		0.05	0.01	0.01	3.67	1.78	0.0
40	10/8/16	S	+	R		0.01	0.04	0.047	1.1	7.52	0.14
41	1/22/17	S	+	R		-0.029	0.03	0.074	2	7.8	0.4
42	7/11/17	Z	-	L	+	0.015	0.05	0.003	2.69	4.62	8.18
43	7/23/17	Z	-	L	+	0.05	0.05	0.03	4.24	0.86	0.0
44	8/20/17	Z	-	R	-	-0.03	0.08	0.004	6.05	16.13	2.775
45	9/26/17	S	+	A		-0.0006	0.024	0.012	0.08	1.16	0.0
46	10/29/17	Z	-	R	-	-0.01	0.027	0.025	1.65	13.9	0.0

Table 4.4: Helicity signs of chromospheric filaments, coronal sigmoids and EnHel calculations.

Chapter 5

TRAVEL TIMES OF ACOUSTIC WAVES IN FLARING REGIONS OF THE SUN

The following work has been done under the guidance of Dr. Stuart Jefferies, GSU and will be a coauthor upon publication.

5.1 Introduction

Solar Flares are energetic bursts of events on the Sun whenever oppositely signed magnetic field lines come close to each other. It causes the field lines to reconnect, energising the particles in the vicinity to give intense bursts of ultra-violet (UV) and X-ray radiation and sometimes gamma-rays (Ackermann et al., 2014; Linden et al., 2018). The causes of these bursts of energetic particles and photons are of interest to us because it can potentially damage our communication satellites, be hazardous to astronauts in the International Space Station (ISS) and those on extra-vehicular activities. An increase in UV rays can affect the outer atmosphere of the Earth by expanding it due to heating increasing the drag on low earth satellites, sometimes causing them to de-orbit and burn up in the atmosphere (Doornbos & Klinkrad, 2006). Human exposure to particle events from the Sun can increase the chances of cellular mutation that may lead to cancer. There are low exposure compartments on the ISS to contain the astronauts during such events. However, an accurate prediction of these events is necessary to know when they should seek rescue in these compartments and when to switch satellites into safe-mode so that they are not affected by over-charging and short-circuiting. To this end there have been several attempts to predict and forecast solar energetic events as briefly reviewed in Chapter 1, with the best lead time of about one hour.

In the current work, we use atmospheric helioseismology (Finsterle et al., 2004a), i.e. studying acoustic-wave properties in the solar atmosphere, using observations of the Sun at two heights - the formation heights of potassium (K) and sodium (Na) are in the photosphere and low chromosphere, respectively. The technique of using atmospheric helioseismology by measuring at multiple heights is advantageous in understanding the behaviour of waves in the atmosphere (Finsterle et al., 2004a,b), and in this work in magnetic and non-magnetic conditions. By making Dopplergrams of these images and cross-correlating them, we use the phase lag of the acoustic waves in different frequencies to understand if they can be used as a diagnostic for predicting solar flares.

Solar flares cause large scale excitation events in the plasma (Thompson, 2004). Seismic waves called sun-quakes (Donea & Lindsey, 2005) and EIT waves have been commonly observed during flares (Long et al., 2017). Power spectrum enhancements in the flaring sites have been observed in flaring regions during the occurrence of the flares. Ambastha et al. (2003) observed that p-mode oscillation power in the 3 mHz range is higher in active regions during flares compared to non-flaring regions of similar strength. Kumar & Ravindra (2006) reported the enhancement of power during flares in the 5 mHz to 6.5 mHz and depression in the 2 mHz to 4 mHz ranges. More recently, Wiśniewska et al. (2019) also showed that post-flare loops and the change in conditions of the plasma during the eruption reduces the power outside the flaring region but enhances it inside in frequencies greater than 5mHz.

The above mentioned analysis and results have been reported mostly during the flare time. In this work, we study active regions on the Sun to observe any changes occurring in the travel time of acoustic waves before a flare occurs. Acoustic waves have been used as a diagnostic to understand the interior of the Sun ever since surface oscillations of five minutes were discovered (Leighton et al., 1962; Ulrich, 1970). Some of the main discoveries about the interior of the Sun using acoustic waves are the location of the boundary between the radiative and the convection zones (Christensen-Dalsgaard et al., 1991), the sound speed, temperature and density gradient towards the interior, opacity of the plasma in the interior which is important for estimating metal abundances, mixing of elements, modelling interiors of other stars, rotation rate with depth and

slow rotation of the core (Chaplin et al., 1999), etc. Acoustic oscillations are mainly excited due to the turbulent motion of plasma overshooting from the convection zone onto the photosphere (Uchida, 1967) giving rise to pressure-mode (p-mode), gravity mode (g-mode) and fundamental modes (f-mode) of oscillations. Acoustic p-mode and f-mode are high amplitude oscillations that are readily observed on the surface of the Sun while g-modes have a very low amplitude at the surface and hence are difficult to detect (Thompson, 2004).

There are several methods that have been used for analysing the acoustic properties in local regions on the Sun. Time-distance helioseismology, helioseismic holography, ring diagram and power spectrum analysis are some of the main local helioseismology techniques (Gizon & Birch, 2005). In this work we use Fourier cross-correlation and phase difference techniques to obtain travel-times of p-mode acoustic waves in the atmosphere to understand if they can be used as a diagnostic precursor of solar flares. The ubiquitous five minute oscillations at the photosphere of the Sun correspond to a frequency of 3 mHz. Other low frequency waves up to $\sim$5.5mHz get reflected back into the Sun and are evanescent in the solar atmosphere (Finsterle et al., 2004a). Frequencies above $\sim$5.5 mHz are free to travel into the atmosphere. The waves that get reflected back into the Sun are refracted in the convection zone due to increase in the sound speed with increase in temperature causing it to bend towards the surface and get reflected there again, leading to the formation of standing waves. The signatures of these waves are seen through their evanescent “tails" in the atmosphere. The waves above 5.5mHz that are free to travel in the atmosphere are called propagating or travelling waves and may later get reflected at the plasma β = 1 surface or continue to travel along magnetic field lines and dissipate at chromospheric or coronal heights heating these layers (Wedemeyer-Böhm et al., 2009). The frequency of 5.5 mHz, waves below and above which are trapped and travelling waves, respectively, is called the acoustic cutoff frequency (ν_{ac}) and is unique to the solar quiet-Sun regions (Jefferies et al., 1994; Wiśniewska et al., 2016; Kayshap et al., 2018). It derives from the fact that there is an abrupt drop in the gas density at the photosphere (Worrall, 1991; Kumar, 1993).

In a magnetized atmosphere this cutoff frequency changes depending on the magnetic field strength and the inclination angle of the magnetic field lines emanating from the magnetic regions (Bel & Leroy, 1977; Jefferies et al., 2006; McIntosh & Jefferies, 2006). Here acoustic waves are magnetoacoustic, and waves with frequency less than the cutoff frequency are thought to become travelling waves in the atmosphere through what are known as magnetoacoustic portals (Jefferies et al., 2006) because of the changes in the angle that the magnetic field makes with the normal as hypothesized by Bel & Leroy (1977). These portals are found in active regions where there are strong and inclined magnetic fields and in the network regions of the “quiet" Sun. Jefferies et al. (2006) created travel-time maps of a large patch of the Sun that includes active and quiet regions. They observe significant signal in frequencies lower than the acoustic cutoff frequency in regions of high magnetic field inclination and in network boundaries. In order to confirm that low frequency magnetoacoustic waves become travelling waves in inclined magnetic fields, McIntosh & Jefferies (2006) performed field extrapolations to juxtapose inclined field lines on phase travel-time maps of a sunspot region for frequencies lower than ν_{ac} for quiet Sun. They show the lowering of ν_{ac} at high field inclinations and low plasma-β, in sunspot penumbra regions.

The propagation of acoustic waves also depends on the location of the magnetic canopy where the plasma β is $\sim$1 (Gary, 2001; Bogdan et al., 2003; Wedemeyer-Böhm et al., 2009). This is the location where the gas pressure and the magnetic pressure are in equilibrium and the sound speed is the same as the Alfvén speed. Upon reaching this layer, fast acoustic waves, such as the waves with frequencies above ν_{ac}, mode-convert to become fast magnetic and slow acoustic waves, while the latter continue to travel along the field lines, the former are refracted and reflected (Cally & Moradi, 2013). We use waves of frequencies 2 mHz - 8 mHz to do our analysis mainly focusing on 4.5 mHz and 6.5 mHz, as they are just adjacent to ν_{ac} and would be most sensitive to the changes in the magnetic conditions such as, increase in the inclination angle of field lines, which is thought to occur prior to reconnection with other field lines, would shift ν_{ac} to a lower value ($\nu \approx \nu_{ac} cos\theta$; Bel & Leroy 1977) making them travelling waves. And the travel-time curve (Finsterle et al., 2004b) at 6.5 mHz has almost maximum gradient which makes it sensitive to changes caused by the inclined

fields. The text in this chapter is organized as follows. Section 5.2 describes the Doppler data from the two heights above the photosphere and the methods used to conduct the analysis. We explain the data analysis in section 5.3. Section 5.4 gives a summary and the conclusion of our results.

5.2 Data and methods

5.2.1 *Dopplergrams*

We use multi-height Doppler images of the Sun obtained during the austral summer of 2003 from the South Pole observing station in Antarctica, using an instrument called Magneto Optical filters at Two Heights (MOTH; see Finsterle et al. 2004a for details about the instrument). The images are taken using K and Na magneto-optical filters (MOFs) in their red and blue wings, at a cadence of 10 seconds. The mean formation heights of potassium (K, 7699) and sodium (Na, 5890) are 420 km and 790 km above the solar photosphere respectively (Finsterle et al., 2004a).

The red (R) and blue (B) wing images in each wavelength are dark subtracted, flat fielded and smear removed. The images are then made into Dopplergrams using $\frac{R-B}{R+B}$. An example image of K and Na is shown in Fig 5.1. The images are 512 $\times$ 512 and the pixelscale is $\sim$5.4"/pixel. An initial analysis performed to obtain the diameter of the MOTH images using parabolic fitting to identify the edge of the solar disc gave a diameter of about 356 pixels. We use this measurement to resize magnetogram images to identify the locations of the flaring and non-flaring regions, as explained in subsection 5.2.2.

The MOTH data used for this work were obtained in four runs. We analyse the data from second and third runs and the ones from the fourth run will be utilized at a later time. The data from the first run is unavailable. The start time and the length of the three available observing runs are given in Table 5.1. Among these, the Jan 01 run contains two C-class flares, the Jan 06 run about 29 C & M class flares and the Jan 17 run about four C-class towards the end of the observation time. For the work presented here, we have utilized data from Jan 01 and Jan 06 runs. The NOAA Active Region number associated with the flare locations along with the start and peak times along with

their Geostationary Operational Environmental Satellite (GOES) flare-classes (Garcia, 1994) for these runs are given in Table 5.2.

The reduced data is processed as follows. The regions where the flares occur are identified and large cutouts in both K and Na around this region are made. The cutouts are derotated using *fshift* program in SOLARSOFT IDL[1] to correct for solar rotation considering the Sun as a solid body with the solar north pointing up. We find that the rotation rate for the Sun in K and Na is about 4.828×10^{-3} pixels per frame at the disk center. Images with large difference in timestamps are blinked to verify tracking of the features after performing the derotation. Figure 5.2 shows the areas of some of the cutouts used for the analysis. The cutouts include flaring (green boxes), non-flaring (blue boxes) and quiet regions (not marked). Non-flaring regions are defined as magnetic regions of similar strengths as that of the flaring regions without any “flickering" or loop-brightening seen in Solar and Heliospheric Observatory (SOHO; Scherrer et al. 1995) Extreme Ultraviolet Telescope (EIT; Delaboudinière et al. 1995) movies in 171Å in these locations. Quiet regions are defined as non-magnetic regions or regions with very low magnetic strengths between 2 and 32 G.

Test plots of time series by picking a few (4-6) random pixels are made to check for spurious spikes, often caused due to loss in telescope guidance due to the presence of clouds. Such images are replaced via interpolation using 2-3 adjacent images on each side. In some cases where an image or two are not clear, they are replaced by the average of its adjacent images. The 2003 MOTH CCD (Charged Coupled Device) camera also had a time integration issue, every fifth image dropped a frame while performing the time integration. Normally, each image was made of 20 frames and the fifth image had only 19 frames. This was corrected by multiplying the fifth image with a factor by which it differed by the previous four images. Doppler images have a velocity trend due to solar rotation. The trends in K and Na Dopplergrams are removed by fitting a polynomial to the time series of each pixel in the cutouts, using the *poly_fit* program in SolarSoft for IDL.

The data are ready to be used after all the above corrections. The cleaned and detrended cutouts of K and Na are passed through a pipeline to produce the cross-spectra of the images. The time

[1] https://www.lmsal.com/solarsoft/

series is divided into three hour windows and moved by five minutes after each three hour window. A previously performed phase travel-time map of a flaring region showed acoustic signatures more than two hours prior to a solar-flare (communication with S.J.). In order to avoid flare signatures influencing any acoustic wave signatures which may be present prior to flares, we choose a sufficient but not too large a window of three hours for our cross-spectra analysis. Time series corresponding to each pixel in the cutouts of K and Na are apodized by 10% to gradually smooth the ends of the time-string to zero to avoid spectral leakage while performing Fourier transformations. We treat the data in a similar manner as in Finsterle et al. (2004a) and Jefferies et al. (2019). The cross-spectrum (C) of the each pixel in K and Na Dopplergrams, in time is obtained using,

$$C = \mathcal{F}_{\nu 1}(K) * \mathcal{F}^{*}_{\nu 2}(Na) \tag{5.1}$$

where $\mathcal{F}$ represents the Fast Fourier Transform and $\mathcal{F}^{*}$ refers to its conjugate function. The cross spectra are smoothed by convolving with a Gaussian function of full-width at half maximum of 0.5 mHz to remove stochastic noise.

We obtain the cross spectra of K and Na that contain x and y dimensions of the image-cutout and 540 frequencies corresponding to the three hour windows (half of the frequency array is considered because performing an FFT gives two symmetric halves) with the Nyquist frequency being 50 mHz. Thus we have a moving window of an array sized *[nwind, xsize, ysize, nfreq]* where *nwind* is the number of windows over which cross spectra have been obtained, *xsize* and *ysize* are the sizes of the flaring and non-flaring boxes and *nfreq* is the total number of frequencies up to 50 mHz. We average the cross-spectra array thus obtained over the x and y sizes and obtain phase difference between the two heights. The analysis is limited to between 2 mHz and 8 mHz as the signal-to-noise ratio beyond these frequencies is low.

We conduct two sets of analysis using the resulting cross-spectra array which is of the form *[nwind, nfreq]*. First, we analyse the phase travel-time obtained from *nwind* cross-spectra against frequencies between 2 mHz and 8 mHz for various flaring and non-flaring regions. This is labeled

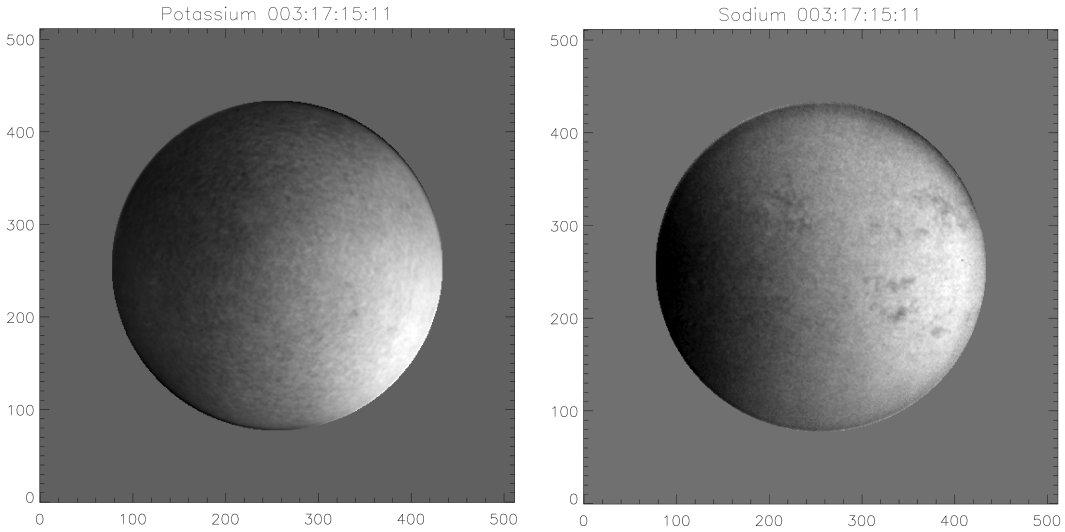

Figure 5.1: Potassium and Sodium Doppler images obtained from MOTH K and Na red wing and blue wing images. The magnetic regions can be clearly seen in the sodium image (right) as dark diffuse regions.

as “Travel-Time against Frequency (TTF)". Second, we average *nwind* over a bandwidth of 0.4 mHz with central frequencies (f) of f+0.5 mHz and calculate the travel-time to observe how each frequency evolves with time for the various regions and any change before, during and after the flare are observed. This analysis is labeled as “Evolution of Travel-Time (ETT)" and are presented in section 5.3. We mainly focus on 4.5 mHz and 6.5 mHz. The phase difference, ϕ and travel time τ corresponding to the phase differences are obtained using the following equations.

$$\Delta\phi = tan^{-1}\frac{B}{A} \tag{5.2}$$

where A and B are the real and imaginary parts of the complex cross-spectrum of the form $A+iB$. Phase travel-time, τ is obtained using

$$\tau = \frac{\Delta\phi}{\omega} \tag{5.3}$$

where $\Delta\phi$ is the calculated phase difference and $\omega = 2\pi f$. Phase wrapping which commonly occurs in frequencies beyond $\sim$5 mHz is corrected for by adding or subtracting 2π to the phases that have a phase jump of over $\mp\pi$ radians.

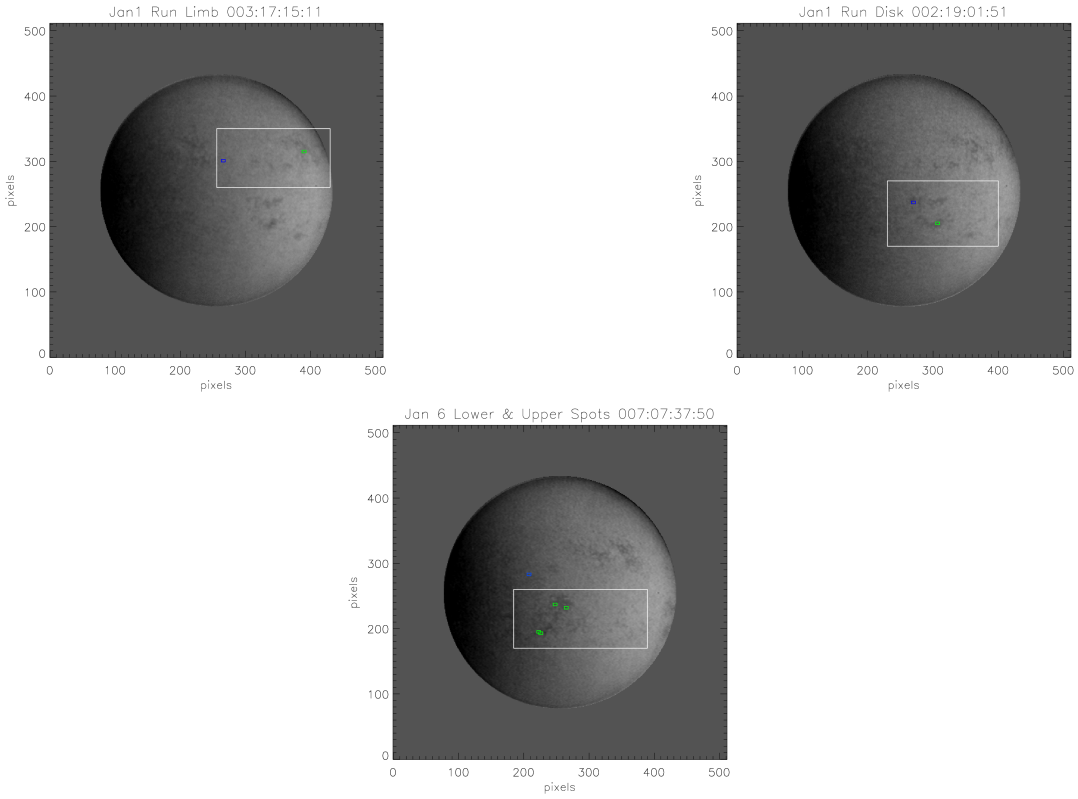

Figure 5.2: The white boxes overlayed on the full disk images represent the regions of the cutout containing the flaring (green) and non-flaring (blue) regions used in the plots shown in Figure 5.9. Top two full disk images belong to the Jan01 run with the left image showing the region of the limb flare and the right image showing the region of the disk flare. Bottom Sun image gives the region for the Jan06 flare. The 002, 003 and 007 in the titles of the images correspond to the respective number of day of the year. The times are in UT. The zoomed-in regions of each of the cutouts are shown in Figure 5.3.

Runs	Start Time	No. of Hours
Jan 01	20:48	45:45
Jan 06	16:59	106:44
Jan 17	22:41	68:06

Table 5.1: MOTH 2003 observing runs with start date, time and length of the runs.

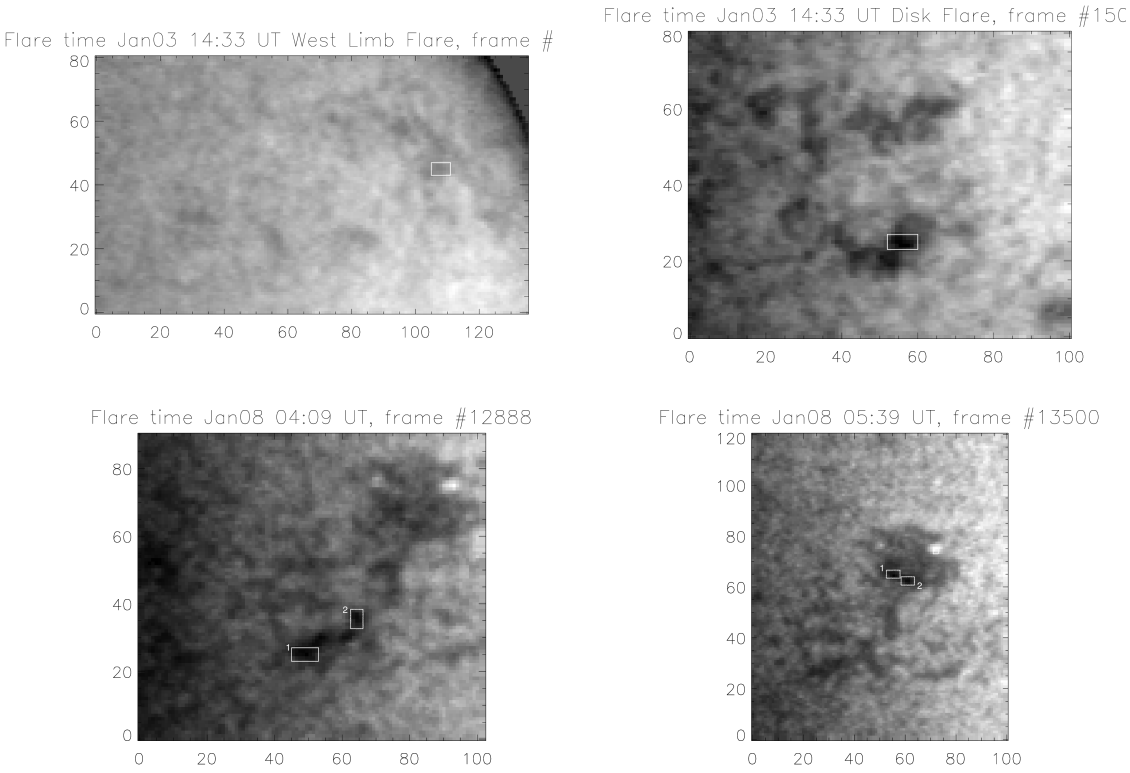

Figure 5.3: The zoomed-in active regions corresponding to the Jan 01 Limb and Disk flare shown in top left and right panels respectively and Jan 06 lower and upper sunspots shown in the bottom left and right panels respectively. The white boxes mark the exact regions of the flares whose characteristics in 4.5 mHz and 6.5 mHz frequencies in time are plotted in Figure 5.9. The x and y axis are plotted in pixels.

5.2.2 *Magnetograms*

The flaring area usually appears darker compared to its surrounding pixels in sodium Dopplergrams; this feature is used to first identify the exact locations of flare occurrence. The flaring regions are small, about 7×5 pixels in area and appear like spots. Box-cutouts to include only the flaring pixels are made and the TTF and ETT analysis are conducted. Figure 5.3 shows the flaring regions marked

with boxes from the cutouts shown in Fig 5.2. Cutouts of the same regions from MDI magnetograms are made to observe evolution of the magnetic flux during the time of the runs. Although GONG images had better coverage than MDI, they had issues with calibration and alignment due to which only MDI images are used at the moment. MDI cutouts of similar areas as the MOTH cutouts are obtained using IDL subroutines *index2map* and *submap* and derotated using *derot_map*. Flaring regions are also similarly obtained by scaling down the MDI images (pixelscale 1.98"/pix) to match MOTH pixelscale of 5.4"/pix. Figure 5.4 shows the time evolution of the average magnetic field for each flaring region along with markers for flare occurrence in each region. MDI data is intermittent and has many data gaps, but no drastic changes in the fields are seen.

The frequency behaviour of the flaring regions is compared with that of the non-flaring regions identified using EIT movies. This is important in order to compare flaring and non-flaring regions to understand how the acoustic waves behave in each category. We try to identify magnetic regions of similar strengths as that of the flaring regions which also satisfy the above criterion, and draw a 7 $\times$ 5 pixels sized box over the non-flaring regions. We find that our flaring regions are of field strengths between 150 and 600 G (see Fig 5.4). We could only identify non-flaring regions up to 250 G beyond which all of them had bright flickering in 171Å loops indicating reconnecting field lines (flares). As field strength increases, the regions become complicated which is a characteristic of flaring magnetic areas (Hazra et al., 2020). This makes it difficult to find strong magnetic non-flaring regions in order to have a good comparison between the two. However, meaningful comparisons can be made for Jan 01 disk and limb flares, and Jan 06 left-lower-spot (L1) flare where the field strengths in flaring and corresponding non-flaring regions are similar. At this time, we do not have an alternative arrangement to make the best comparison for flaring regions with field strengths greater than 250G. We perform similar steps on the non-flaring regions as explained in the previous subsection, by cutting out the boxes from the maps of cross-spectra obtained, taking the average of the cross-spectra of all the pixels and getting the phase of the region.

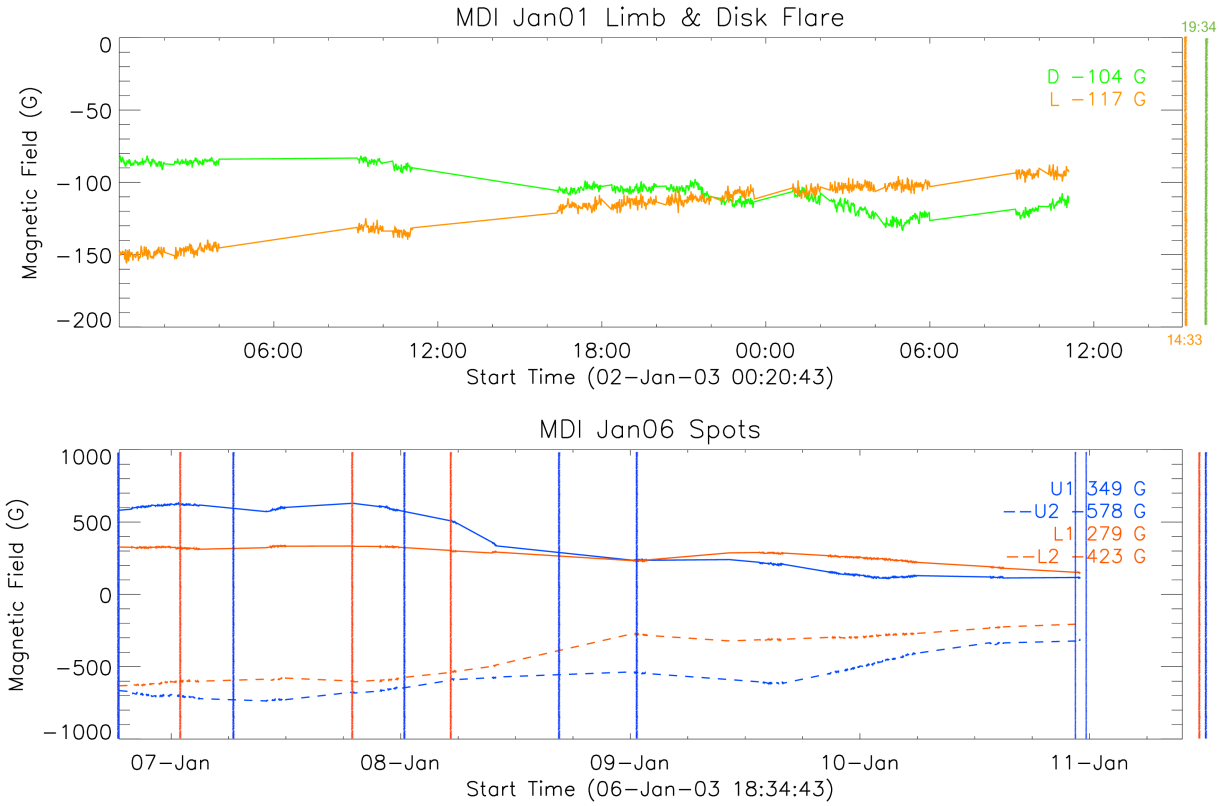

Figure 5.4: Magnetic field evolution of each flaring region from MDI magnetograms. The top panel shows the variations in Jan 01 Disk (green) and Limb (orange) magnetic fields. The bottom panel shows upper (blue) and lower (brick red) spots from the Jan 06 run. Dashed lines correspond to the second spot in the upper and lower spot pairs. Green, orange, blue and red lines correspond to the flares occurred in the respective regions.

5.3 Analysis

5.3.1 *Flaring Regions*

All the analyses are conducted on two of the three observing runs shown in Table 5.1 - Jan 01 and Jan 06. The Jan 01 dataset contains two flares, one that originated from the Limb (AR# 10234) and one on the Disk (AR# 10324). These are labeled as 'Jan01 Limb' and 'Jan01 Disk' flares throughout this chapter. The 106 hours data from Jan 06 could not all be analysed at once because of computer memory issues, hence they are split into two parts - Part1 and Part2. There is a three hour overlap between the end of Part1 and beginning of Part2 while creating the moving windows so that no points in time are omitted in the moving window analysis. The curves for the flaring and the non-flaring regions for Jan 06 are shown continuously in the ETT analysis. However, in the TTF analysis, the Phase Travel-Time (PTT) against frequency for the two parts of the Jan 06 data are shown separately. This is because they are shown against a background of all the pixels of certain magnetic field strength from the whole cutout region which could not be operated upon together. Similarly, quiet region TTFs are also given separately for Jan 06 Parts 1 & 2. The Jan 01 Limb and Disk flaring regions each contain one spot where we have conducted the analysis. The Jan 06 flaring regions have upper and lower flaring regions, containing two "spots" each. They are named as U1, U2, L1 and L2, respectively. We call them spots as they appear to be spot like features in sodium images during flare time. This is not to be confused with sunspots as these regions do not host sunspots.

5.3.2 *Travel-Time with Frequency (TTF) Analysis*

PTT diagrams for frequencies between 2 mHz and 8 mHz are made for quiet region cutouts of magnetic strengths 2-12 G, 12-22 G, 22-32 G and magnetic regions of strengths 100-200 G, 200-300 G, 300-400 G and 100-400 G using all the pixels of corresponding strengths from the regions shown in Fig 5.2. Fig 5.5 shows the PTT curve behaviour of quiet region pixels in orange diamonds corresponding to the cutouts of Jan01 Disk, Jan01 Limb and Jan06 parts 1 & 2. These curves shown

in diamonds are created using the entire length of the runs. The black curve shows the travel-time corresponding to a quiet region of size 7×5 pixels of corresponding strength shown in the respective panels in the figure. Jefferies et al. (2019) showed that the phase difference for Fe-Fe and Fe-Na in quiet regions at 6.5 mHz to be ∼10 and ∼100 degrees respectively. This translates to a travel time of ∼4.27 s and 42.73 s, respectively. We verify that in the quiet region PTT shown in Fig 5.5, the average travel-time at 6.5 mHz is ∼19s between K-Na heights which falls between their values for Fe-Na heights and similar to that found by Finsterle et al. (2004b).

Figure 5.6 shows the PTT curves for flaring and non-flaring 7×5 region in blue and green respectively. The dashed line represents the curves for the second spot in each of the upper and lower flaring regions. The black curves in Fig 5.5 and blue and green curves in Fig 5.6 are the mean of the running averages of the PTTs calculated using the three hour moving window technique where the cross spectrum of K and Na is obtained every three hours and moving them by five minutes. Pink diamonds represent the travel time for all the magnetic pixels of the respective strengths in the respective cutout regions.

For the Jan01 Limb flare occurring at 14:33 UT, the PTT curve starts getting influenced by the flare at ∼12:58 UT as a result of performing the running averaging of consecutive cross spectra. For the Jan01 Disk flare that starts at 19:34 UT, the flare occurs more than three hours after the observing run is complete, hence the PTT curve is not influenced by the flare. In both these cases, a flare occurs close to the end or after the observing run. As seen in the top two panels of Fig 5.6, the mean shape of the PTT curve for the flaring region (green) is quite different from that of the non-flaring region (blue). The ramp that is commonly seen after ν_{ac} in the non-flaring PTT is not seen in the flaring PTT.

The Jan 06 flaring scenario is quite different from that of Jan 01. There are multiple flares during the observing run with a few that occur before and after the run as well. Hence most of the curves generated during the first half of the observing run contain flares and possibly flare signatures. However, similar behaviour in the flaring and non-flaring PTT curves as that seen with the Jan 01 flares is seen for the upper and lower spots for Jan 06 data.

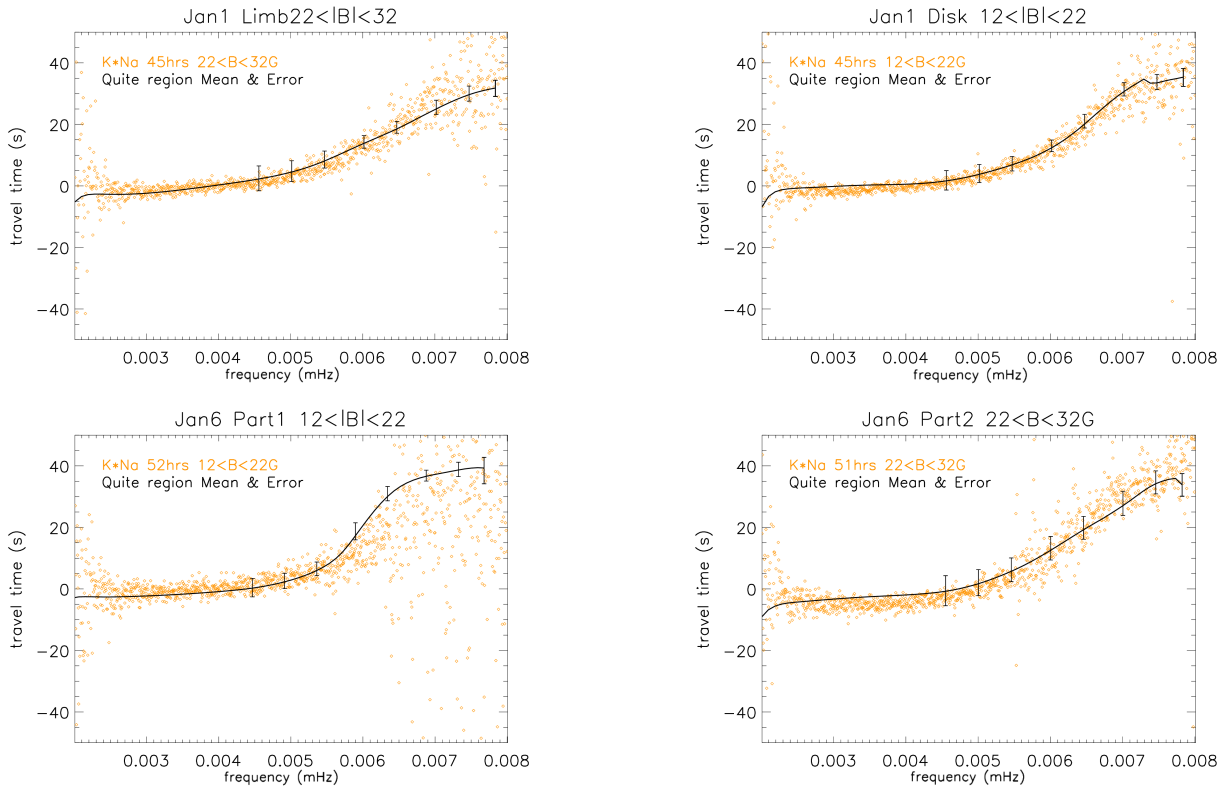

Figure 5.5: Quiet Region PTTs. Top panel are quiet regions close to the Jan 01 Limb and Disk flaring regions, respectively. Lower panels show quiet regions corresponding to Jan 06 Par1 and Part2 of the data. Only two of these are shown because both upper and lower spots are within the same cutout region.

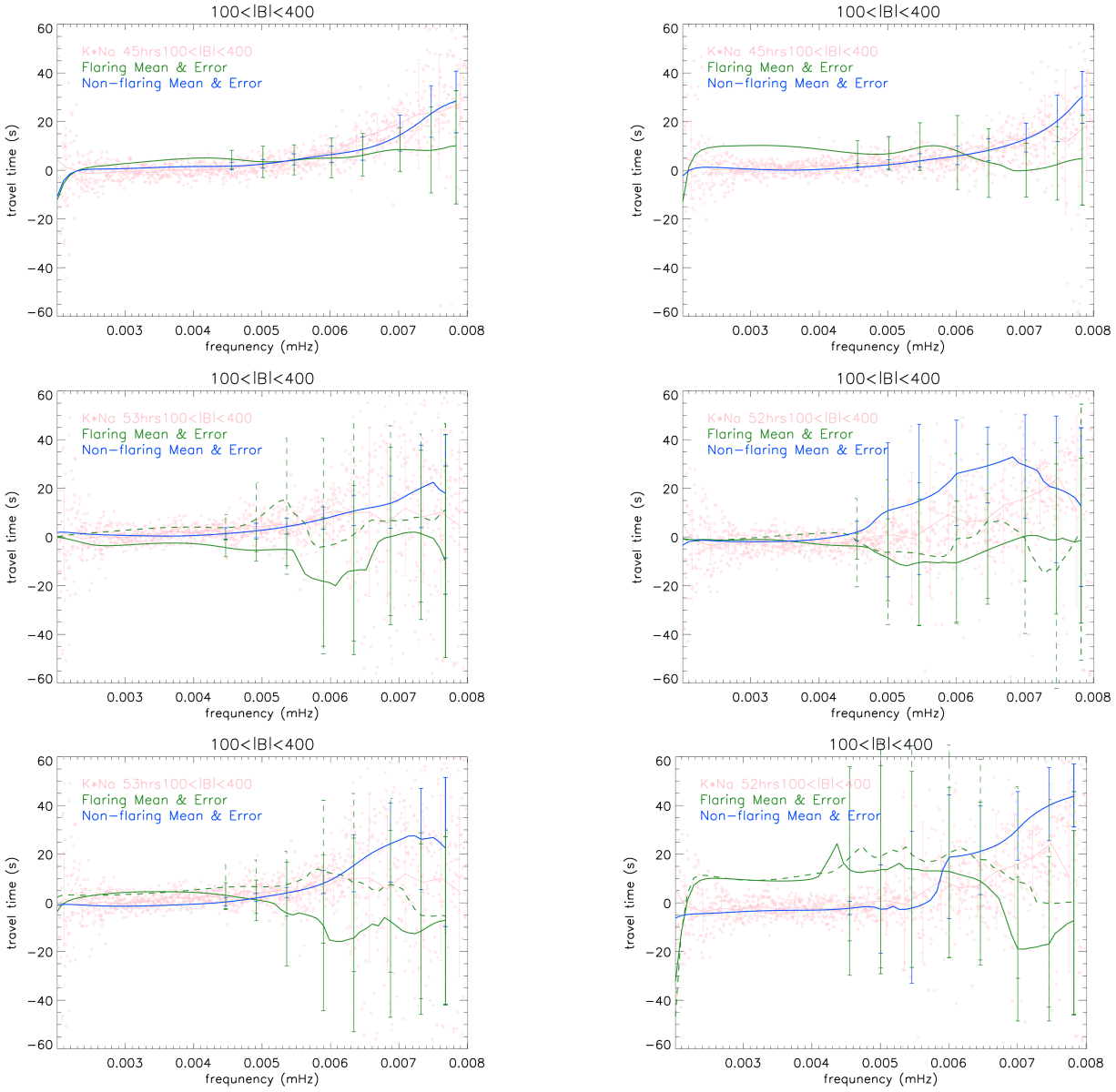

Figure 5.6: Flaring & Non-Flaring Region PTTs. PTTs for Jan 01 Limb and Disk regions are showed in the top panel. The middle panel shows the PTT for Lower Spots from Part1 & Part2 of the Jan 06 data on the left and right, respectively. The lower panel shows the PTT for Upper Spots from Part1 & Part2 of the Jan 06 data on the left and right respectively.

It would be useful to know if the PTTs of a flaring region fundamentally differs from that of a non-flaring region. To understand this, we calculate the PTTs for the duration of the time-series not including a flare or anomalous travel-times. For Jan 01 data, PTTs for the times since the start of the run until 3, 6, 9 and 12 hours before the flare or flare signatures are calculated. For the Jan 06 data, we choose the time when the “spots" are relatively quiet, between Jan 08, 07:12 UT to Jan 10, 12:00 UT for the lower spots, and Jan 08, 00:00 to Jan 09, 04:48 UT for the upper spots. Half the amount of time from both ends of this time string is reduced to get the PTTs of 3, 6, 9 and 12 hours away from the flare and anomalous travel-times. These curves for flaring and non-flaring regions are shown in Fig 5.7 and 5.8, respectively. The non-flaring averages behave the same way as seen in Fig. 1 of Jefferies et al. (2019) whereas the flaring region curves that do not include the flaring data behave starkly differently, and behaves similar to the PTTs calculated with the time-strings that contain the flares in them (Fig 5.6). This possibly is an indicative feature that an active region will produce a flare sometime in its lifetime. However, further investigation is required with examples of more flaring and non-flaring regions of similar strengths.

5.3.3 *Evolution of Travel-Time (ETT)*

It is beneficial to know if an active region will produce a flare. It is also important to know when an active region is going to produce a flare. In this work, deviations in travel-time are observed specifically in 6.5 mHz and are shown in Fig 5.9 for Jan01 Limb, Jan01 Disk, Jan06 Lower spots and Jan06 Upper spots. The curves for the second spot in the latter two are shown using dashed lines. The blue curve represents the non-flaring regions in each case. These regions are same as those used for the PTT curves. As seen in the first panel of the figure, travel-time becomes negative around 08:24 UT, about six hours prior to the occurrence of the flare (red line). Grey dashed lines indicate when the flaring window starts influencing the travel-time curve. In the second panel of Fig 5.9, the Jan 01 Disk flare occurs at 19:34 UT, a little more than three hours after the observing run ends. The change in the travel time from the mean values is seen starting near 04:48 UT, about 15 hours prior to that flare. The Jan 06 6.5 mHz travel-time curves for the two lower spots are

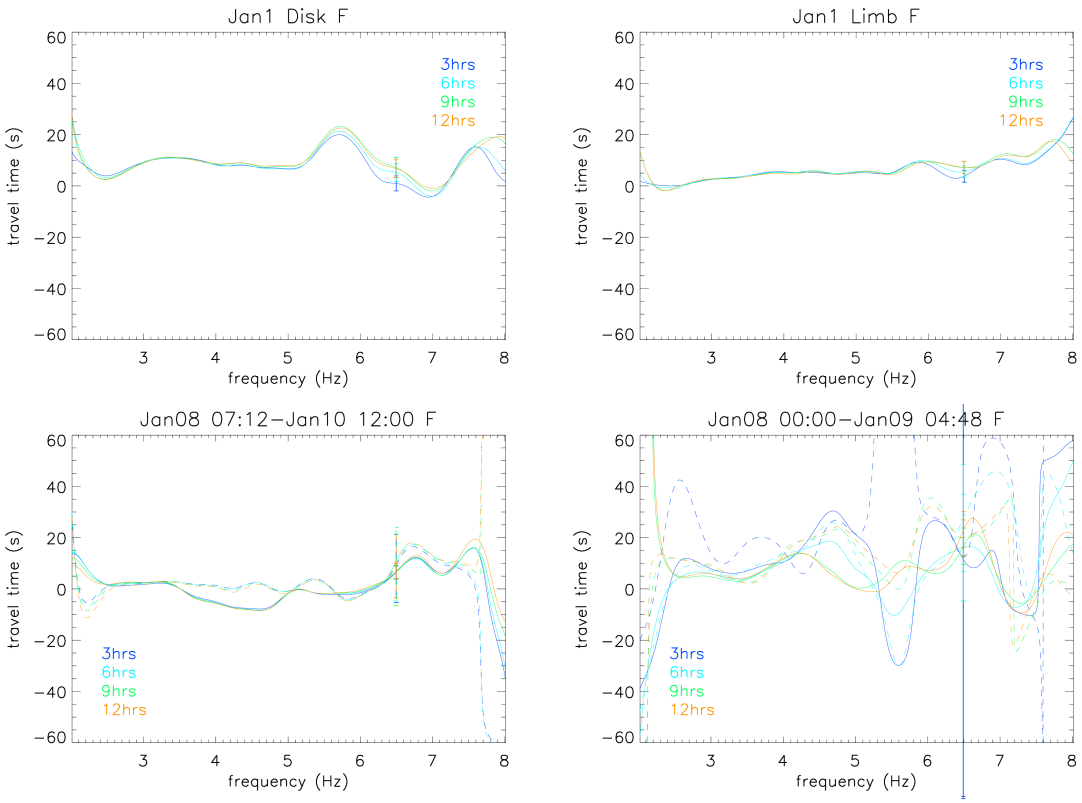

Figure 5.7: Phase travel times for the flaring regions from Jan 01 (Disk and Limb in the top row) and Jan 06 (lower and upper spots shown in the bottom left and right panels) runs. Dashed curves are for spot#2 in each of the plots for upper and lower ones. Error bars represent the standard deviation and are only shown for 6.5 mHz to make the plots legible.

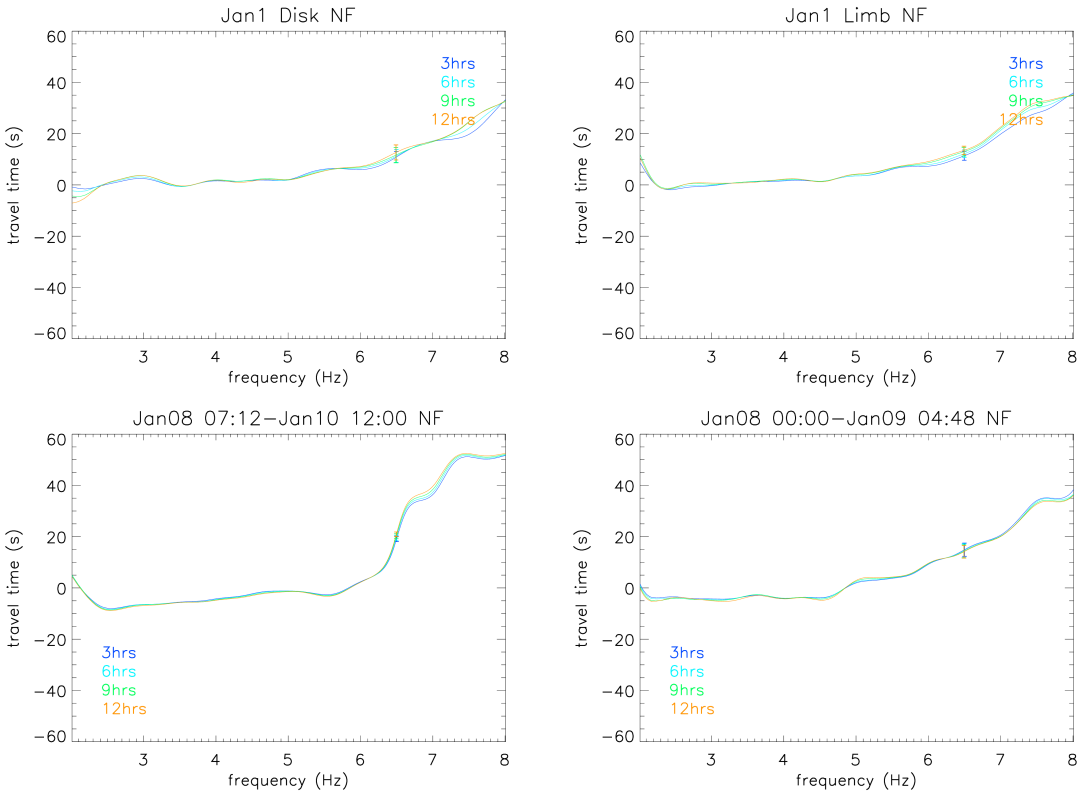

Figure 5.8: Phase travel time curves with frequencies for non-flaring regions. Details same as in Fig 5.7 with the standard deviation much lower than that in the previous figure.

shown in the third panel of the figure. There are three flares in the first part. And deviations in travel-times are seen prior to all these flares. However, the signal in spot2 is positive and that in spot1 is negative prior to the first flare. This is the first flare during the observing run. There was, however, one flare that occurred on Jan 06 at 20:24 UT prior to the beginning of the observations. Similar to the negative travel times prior to Jan 01 limb and disk flares, the negative and positive travel times prior to the second, fourth and third flares, respectively in the Jan 06 run, also appear to indicate signatures prior to flares. The fourth panel shows two green curves for the two upper spots in the Jan 06 data. This region is busy with flares. However, careful observation shows that flare signatures are seen prior to six out of seven flares. Both spots show such signatures prior to the first three flares. There are negative (solid curve) and positive (dashed curve) travel-time signatures in the 4th and 5th flares, respectively. And negative (solid curve) prior to the fifth flare. These signatures appear about 2-7 hours prior the flare start time. Negative travel-times in the above signatures correspond to waves travelling against the line-of-sight or towards the photosphere. More data must be observed at multi-heights between the photosphere and the chromosphere to see if this behaviour is common prior to every flare and in particular, if an active region is “born bad" that will definitely produce a flare by using the TTF analysis.

5.4 Discussions & Conclusions

In this study, we have used Doppler data at two heights in K and Na wavelengths to understand the behaviour of acoustic waves prior to the occurrence of solar flares. We create cross-spectra of K and Na and obtain the phase difference between the two and calculate the travel-time. We make phase travel-time (PTT) curves to compare flaring, non-flaring and quiet regions. We analyse the evolution of travel-times (ETT) in frequencies close to the acoustic cutoff frequency (ν_{ac}), mainly at 4.5 mHz and 6.5 mHz, as these frequencies would be the first to respond to the changes in inclination angles of the magnetic field causing magnetic portals (Jefferies et al., 2006) and changes in the gradient of the travel-time curve would affect that at 6.5 mHz (Finsterle et al., 2004b). 4.5 mHz travel-time curves do not show any interesting changes prior to flares so we only present the 6.5

mHz ones where we do see some significant changes. We also conduct travel-time with frequency (TTF) analysis where we notice that the flaring region PTTs behave differently from those for the non-flaring and quiet regions, in frequencies beyond ν_{ac}. Non-flaring and quiet regions exhibit stable PTT curves whereas the flaring region has a higher standard deviation at each of the frequencies compared to the non-flaring PTTs (standard deviations are only shown at 6.5 mHz in Figs 5.7 and 5.8 to avoid clutter) and unsmooth variations between 5 mHz and 8 mHz.

Acoustic wave propagation in a magnetic field region is a complex phenomenon. It involves the plasma $\beta = 1$ layer (magnetic canopy) where the sound speed and the Alfvén speed are equal, and acts as a boundary where the acoustic waves can get refracted and reflected apart from mode converting into magneto-acoustic waves (Rosenthal et al., 2002; Cally & Moradi, 2013). Rijs et al. (2015) via models and Jefferies et al. (2019) via observations showed the presence of power halos around magnetic regions in frequencies higher than ν_{ac} due to reflected waves. They suggest that the fast acoustic waves ($\nu > \nu_{ac}$) interact with the $\beta = 1$ layer and convert into slow acoustic and fast magnetic waves; the slow waves travel further along the magnetic field lines. And the fast magnetic waves travelling along the field lines refract and reflect at a layer where $2\pi\nu/k_x$ (ν is the frequency and k_x is the horizontal wavenumber) is the same as the Alfvén speed and convert into slow magnetic and fast acoustic waves. We use 6.5 ± 0.2 mHz waves to do our analysis. As seen in Fig 5.9, most of the flare “signatures" show a negative travel time and some increased positive travel times. The case of the plasma beta is intricate in that, waves interacting with it in regions of different magnetic field strength, plasma temperature, field line orientation etc (Schunker et al., 2008; Rijs et al., 2015) behave differently. Finsterle et al. (2004b) showed in the case of a decaying active region and a sunspot, using power spectrum at 7 mHz that the travel-time decreases with an increase in magnetic field lowering the plasma $\beta = 1$ layer (Rosenthal et al., 2002; Bogdan et al., 2003). It is possible that the emerging flux lowers the $\beta = 1$ layer causing the above mentioned processes and that the negative travel time we observe correspond to the refracted fast acoustic waves from the second layer, and perhaps the mode-converted slow acoustic waves in the case of

increased positive travel-time signatures. However, this is just a conjecture and we do not have a convincing mechanism that explains the observations at present.

Finsterle et al. (2004b) showed with power maps of magnetic regions that the acoustic wave travel-time decreases with increasing magnetic field, as also shown with dispersion diagrams by Jefferies et al. (2019). In these cases, the travel time at 7mHz in strong magnetic field regions of strengths greater than 100 G tended to zero. In the current study, the flaring regions all have magnetic fields stronger than 100 G. It is possible that the phase travel-time curves in green shown in Fig 5.6 are because of the decrease in travel-time due to the lowering of the height of the magnetic canopy in strong field regions. However,

1. as seen in Fig 5.7, the unsmooth travel-time curves unlike those seen in Figs 5.5 and 5.8 indicate abnormal behaviour in active regions. This may be indicative of flares, but further investigation is needed.

2. The change in 6.5 mHz phase travel-time curves occurs prior to the flare after a long “quiet" time for the Jan 01 limb flare which lasts from Jan01_20:00 UT to Jan03_07:12 UT. In the Jan 01 disk flare, the quiet time is from Jan02_02:24 UT to Jan03_02:30 UT. Similarly, the quiet times in the Jan06 data in the lower spots is from Jan08_07:12 UT to Jan10_12:00 UT and in upper spots from Jan08_00:00 to Jan09_04:48 UT. The PTT curves during quiet times show similar behaviour as seen in PTT curves that include flare times (Fig 5.7), and are different from the behaviour seen in PTTs of non-flaring regions made using the same time ranges.

3. In addition to the above, deviations from the mean travel-time in the 6.5 mHz travel-time plot shown in Fig.5.9 prior to flares in eleven out of thirteen of them, are another possible indication of future flaring activity.

It would be beneficial to test with other multi-height Doppler datasets on the behaviour in terms of changes to 6.5 mHz travel-time as well as for the phase travel-time against frequency curves for active regions of lesser field strengths. Further investigation of the PTT curves in the locations of magnetic regions of different strengths would help us understand if they are actually variable in flaring active regions versus others. Also, we recently found that the data from the Jan 17 observing

run, which contains a few flares that occurred on Jan 20 towards the end of the observing run after a long quiet time and is well suited for conducting the PTT and TTF analyses. This will be conducted in the near future. This may also answer the question about whether the PTT curves only represent the dispersion relation for a given magnetic region or if it can be used as an indicative measure to distinguish between a flaring and a non-flaring active region. It would further be beneficial to find strong active regions that do not flare and compare their PTTs with the ones that do flare. However, as one might guess, this might not be practical as most strong active regions usually produce one or more flares.

In conclusion, our TTF analysis on flaring and non-flaring regions shows that there is inconsistency in the behaviour of the PTT curves above ν_{ac} with large standard-deviations at 6.5mHz as compared to those of the non-flaring regions. Our ETT analysis for flaring regions show large variations in travel-time signatures prior to the flare occurrence. We believe that these analyses, respectively, possibly indicates that a region will produce one or more flares, and that a flare might occur in about 3-15 hours time, providing a better lead time as compared to the currently existing methods which give a best lead time of about one hour. We also note that solar flares may be stochastic and any amount of prediction efforts may not predict all of them with precision (Leka et al., 2019). However, using various physics based methods help us understand the processes governing solar activity while empirical methods help us understand the statistics both of which are important for successful predictions and forecasting of most eruptive activity if not all. We believe that this work contributes to one small step in this direction.

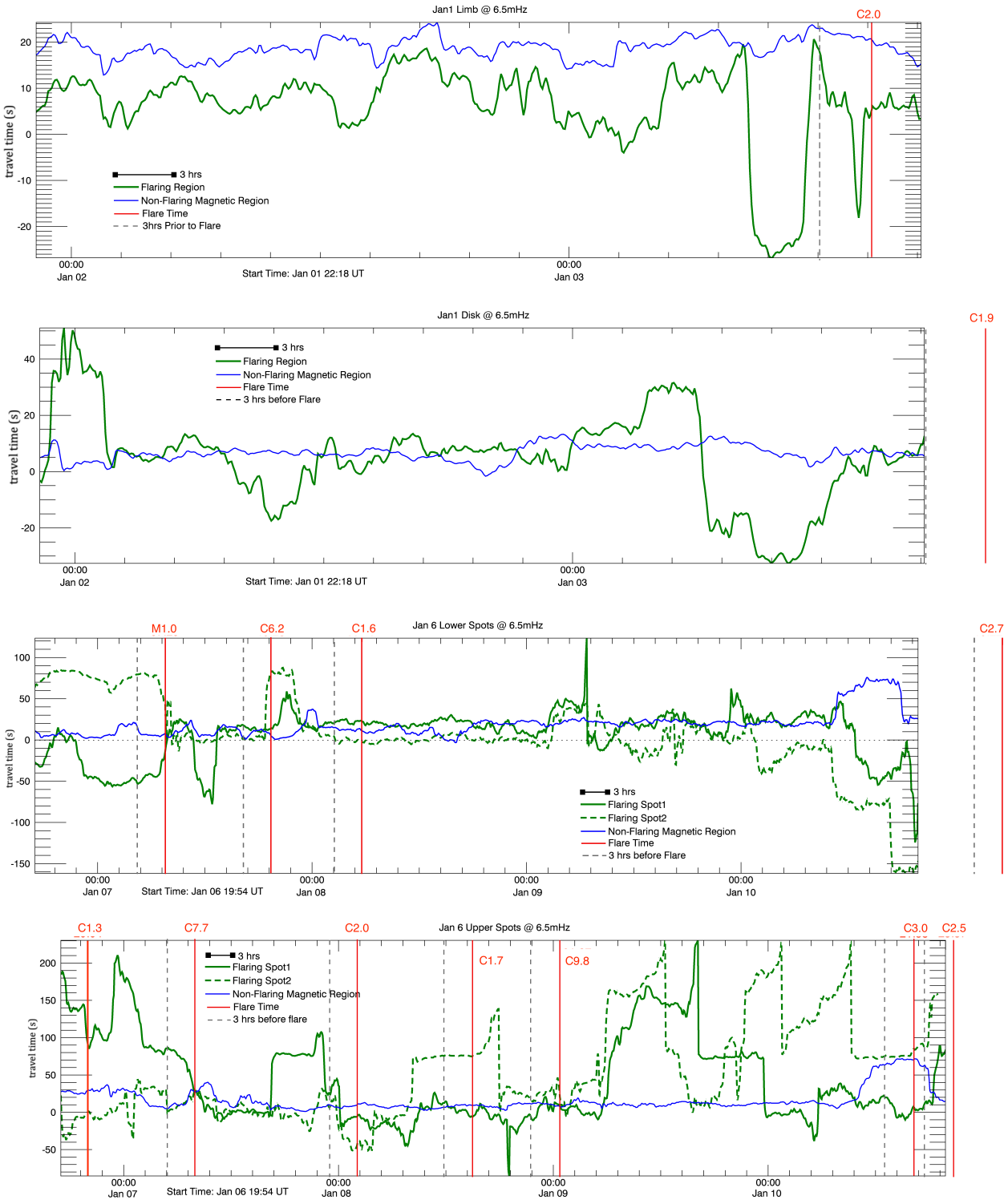

Figure 5.9: Travel-time evolution in 6.5mHz for the four flaring regions. Top two panels show the phase travel-time variation for the Jan 01 Limb and Disk flaring regions (green) and their nearby non-flaring regions (blue). The third and fourth panels from the top show the travel time variation for Jan 06 lower and upper spots in green, respectively. Solid and dashed lines represent the 1st and 2nd spots, respectively.

Start Time	Peak Time	End Time	AR Number	X arcsec	Y arcsec	GOES Class	Flare Position
01/03/03 14:33	01/03/03 14:45	01/03/03 15:00	10234	746	375.6	C2.0	Limb
01/03/03 19:34	01/03/03 19:38	01/03/03 19:40	10243	474.9	-227.9	C1.9	Disk
01/07/03 07:29	01/07/03 07:50	01/07/03 8:11	10244	-140.4	-276.2	M1.0	Lower
01/07/03 19:23	01/07/03 19:36	01/07/03 19:42	10244	-15.7	-275.0	C1.6	Lower
01/08/03 05:40	01/08/03 05:52	01/08/03 6:20	10244	62.6	-274.2	C6.2	Lower
01/11/03 10:22	01/11/03 10:29	01/11/03 10:41	10244	682.4	-291.9	C2.7	Lower
01/11/03 10:50	01/11/03 10:55	01/11/03 11:01	10244			C3.0	Lower
01/11/03 11:09	01/11/03 11:11	01/11/03 11:12	10244			C2.3	Lower
01/11/03 19:25	01/11/03 19:33	01/11/03 19:51	10244	722	-297.8	C2.4	Lower
01/07/03 08:28	01/07/03 08:33	01/07/03 08:38	10242	16.9	-23.5	C7.7	Upper
01/08/03 02:31	01/08/03 02:38	01/08/03 02:45	10242			C2.0	Upper
01/08/03 16:21	01/08/03 16:27	01/08/03 16:31	10242	282.3	-27.4	C1.7	Upper
01/09/03 01:27	01/09/03 01:39	01/09/03 02:03	10242	361.8	-29.7	C9.8	Upper
01/10/03 21:58	01/10/03 22:07	01/10/03 22:12	10242	694.6	-55.4	C3.0	Upper
01/10/03 23:37	01/10/03 23:41	01/10/03 23:50	10242	706.2	-56.9	C2.5	Upper
01/11/03 00:06	01/11/03 00:42	01/11/03 00:52	10242	717.6	-57.7	C2.5	Upper
01/11/03 13:09	01/11/03 13:15	01/11/03 13:34	10242	792.8	-51.8	C1.9	Upper
01/11/03 16:01	01/11/03 16:11	01/11/03 16:42	10242	802.4	-53.5	C2.3	Upper
01/11/03 22:45	01/11/03 22:51	01/11/03 22:58	10242	838.2	-60.3	C1.6	Upper

Table 5.2: Table gives the flare timing, location and the GOES class of the flares encompassed in the MOTH 2003 data.

Chapter 6

SUMMARY AND FUTURE WORK

In this dissertation work, I have discussed how solar features such as filaments and sigmoids can be used for space weather prediction purposes. I have also investigated if acoustic waves can be used for predicting solar flares. Firstly, I have utilized on-disk chromospheric Hα filaments to obtain the axial magnetic field directions of filaments and correlate those with the axial field directions of inter-planetary CMEs near Earth that result from the eruption of these filaments. The analysis was done in two stages. First for data between 2007 and 2017, second for those between 1996 and 2007. Altogether, there are 173 eruptive filaments analysed between 1996 and 2017, for which we obtain axial field directions with the help of Martin's chirality detection method using Hα and corresponding magnetogram images. From putting together both cycles 23 and 24 data, we find that in $\sim 75\%$ of the cases, the axial field direction is retained between ICMEs observed at L1 and their filament counterparts on the Sun before eruption. The results from these analyses have been published in ApJ and ApJS. The results have direct implications to predicting if CMEs originating from these filaments will have an effect on the Earth's magnetosphere several days in advance. Indeed, CMEs whose filaments are determined to have a north pointing axial magnetic field will not have an effect on Earth's magnetic field and those with a south pointing axial field will reconnect with the Earth's magnetic field to cause space weather effects on the ground and for satellites in space. Our filament-ICME dataset is the largest in existence as far as I know, and consists of active-region filaments as well as quiet region filaments. CMEs are known to occur from both types of regions, although active regions tend to produce more frequent and stronger eruptive events (Toriumi & Wang, 2019). Hence monitoring these regions and filaments is necessary for

proper predictions. I note that, cycles 23 and 24 individually show 65% and 85% retention of axial field direction between the source regions on the Sun and near the Earth. The potential cause of this difference may be attributed to the shape of the heliospheric current sheet and locations of coronal holes which can deflect or rotate CMEs changing their field configuration to rotate Kay et al. (2017). Further investigation on the conditions of the inner heliosphere affecting individual cases in which the field configuration differed from that of the source region will be conducted in the future to narrow the possible cause of this difference.

In our filament dataset there are several filaments whose axial field directions could not be determined because the determined chirality was ambiguous. Active region filaments tend to be small and thin with the lack of resolvable features such as barbs and adjacent fibrils that are important for determining the chirality. This in addition to the unavailability of regular high resolution Hα images of filaments leads to ambiguous determination of chiralities in our study. Frequent and regular observations with high resolution instruments such as the Goode Solar Telescope (GST) and the Daniel K. Inouye Solar Telescope (DKIST), will help improve such predictive studies in the future. To establish that high resolution images can be successfully utilized for space weather predictions, I plan to propose observing one or more filaments, depending on observing time availability, using GST and DKIST to exploit the high resolution to obtain field direction using chirality. Furthermore, I am interested in using these high resolution images to gain a deeper understanding of active region filaments, in that how mass motion occurs and where the mass is injected into the filament body.

Also, Martin's method of chirality assumes the presence of minority polarities amongst the majority polarities (Martin, 1998a). While analytical models such as van Ballegooijen & Martens (1989) can explain the presence of minority polarities for the filament barbs to exist and have been observed in quiet region filaments in lower resolution magnetogram images, they have not been observed in active regions which are usually densely magnetic. It would be fruitful to observe high resolution magnetogram images from the above mentioned instruments for this purpose. Moreover, Chen et al. (2014) suggested that chirality obtained via Martin's method only applies for flux ropes

and not when for sheared arcade configurations. It will be beneficial to understand if this is actually the case, because as explained in chapter 4, the same axial field direction must derive from using both Martin's and Chen et al.'s methods.

The instruments mentioned above also provide spectropolarimetric images in multiple wavelengths that form at different heights in the atmosphere. I plan to utilize few of these wavelengths to understand the nature of the endpoints of filaments and barbs, where they are rooted and what roles they play in injecting mass into the filaments. I plan to use spectropolarimetric observations of filaments to understand the nature of the magnetic fields that support the filaments. Wang et al. (2020) via spectropolarimetric inversions of He 10830Å found that a flux rope structure winds about the filament. In their case, it was a quiescent filament, it is however necessary to conduct more observations to understand if active regions filaments have similar structures or they are mainly shear dominated.

I also intend to develop on the approach of using filament chirality detection using machine learning algorithms. Sara Martin, from her backyard observatory at Helio Research, has kindly provided me with the Hα filament data-set obtained for over ten years. I have so far completed labeling these images for left and right chirality filaments along with other features such as prominences and sunspots. I have trained a basic convolutional neural network model using an open-source code-base that does feature detection. The results are preliminary and are still in research phase, hence is not incorporated into this dissertation. I plan to attend to it and release this work in the near future.

In the second part of the dissertation, I investigate the relationship between coronal sigmoids and their counterpart chromospheric Hα filaments. I found that even though the filaments share the polarity inversion lines with the sigmoids, they may not have the same helicity sign as that of the sigmoid. Furthermore, I evaluated how the photospheric helicity signs of the sigmoids compare with those found by observing the filament chirality and the sigmoid handedness. I find that there are cases of partial-match and full-match between the three signs. Partial-match where the photospheric helicity sign matches either with that of the filament or the sigmoid, meaning that the filament and sigmoid are of opposite helicity signs, and full-match where the photospheric sign matches with

that of both the filament and the sigmoid. Altogether, the cases of partial-match produce almost 3.5 times the number of flares produced by the cases of full-match and are deemed to be watch-worthy for prediction purposes. I infer that helicity cancellation might be the reason for flares in cases of partial-match. I also conducted analysis for one persistent sigmoid that was visible on the disk for about 12 days to understand if the changes in the calculated helicity and energy values relate to the flares produced. The analyses are presented in Chapter 4 and is ready for submission and will be submitted to The Astrophysical Journal in the near future. I further plan to make similar analysis for several persistent sigmoids to further understand the relation between magnetic changes and the occurrence of flares.

In the third part of our work, I study acoustic waves using Dopplergrams obtained at two heights - K and Na forming at the heights of $\sim$420 km and $\sim$800 km above the photosphere, respectively. The data was obtained using the MOTH instrument located at the Amundsen-Scott South Pole Station in 2003 (Finsterle et al., 2004a). I observe flaring and non-flaring regions on the Sun, cross-correlate K and Na in those regions and obtain their phase differences to get the travel-times of these waves. I study waves at frequencies 4.5 mHz and 6.5 mHz, closest to the acoustic-cutoff frequency ($\nu_{ac} \sim 5.5$ mHz). These frequencies are chosen for diagnostics for flare precursor studies as these would be most sensitive to any changes to ν_{ac}, for example, an increase in the magnetic field line inclination would reduce ν_{ac} to a lower value and changes to the plasma properties would affect ν_{ac} because of a sensitive gradient around 6.5 mHz in the travel-time against frequency curve. Any changes to the field or temperature would affect the region where the plasma $\beta = 1$, thus affecting where acoustic waves mode-convert into magnetic waves which may later get reflected giving rise to downward travelling waves or waves with a negative travel-time.

The main result from this study is that waves with negative travel-time are observed at 6.5 mHz frequency, suggesting possible flare precursors, about 3-15 hours prior to the occurrence of flares in 11 out of the 13 flares in our dataset. This amount of lead time is useful for protecting satellites and astronauts from radiation storms, although there are possibilities of false alarms with some flares occurring without an acoustic signature. Similar studies need to be conducted to further understand

the statistical significance of these precursors. Furthermore, it is important to reproduce these results with more data. In the near future, I plan to conduct the same analysis on MOTH data from the Jan 17 observing run to see if the few flares that it contains show any flare signatures prior to their occurrence. The dataset has a long quiet time until the flares occur at the end of the observing run on Jan 20. I expect the data to show similar behaviour as that of our Jan 01 Limb and Disk flares as they are also single flares after long quiet times. Additionally, I plan to estimate the height of $\beta = 1$ layer during the time-series of all the observing runs to understand any indications of mode-conversions and reflections due to plasma changes during the precursor signatures. It would be further beneficial to use data from other instruments such as multi-height DKIST observations to further verify this behaviour. I am also interested in using 2003 multi-height Dopplergrams or other MOTH datasets to see if emerging active regions or sunspot regions can be predicted using phase difference analysis. Using phase travel time (PTT) curves of flaring and non-flaring regions, it is seen that PTT curves of flaring regions behave somewhat differently from that of non-flaring regions. I plan to build this analysis using more non-flaring regions to observe if this behaviour is consistent. If it is, then emerging active regions can possibly be predicted to be flaring or non-flaring as early as they are born.

In conclusion, in this dissertation, I have presented new results using novel techniques that can potentially add to and improve existing space-weather prediction and forecasting methods. The methods presented here may be used on a standalone basis or together with these or other existing methods which can then potentially provide predictions with improved accuracy.

REFERENCES

Abramenko, V. I. 2005, The Astrophysical Journal, 629, 1141

Ackermann, M. et al. 2014, The Astrophysical Journal, 787, 15

Aggarwal, A., Schanche, N., Reeves, K. K., Kempton, D., & Angryk, R. 2018, The Astrophysical Journal Supplement Series, 236, 15

Alipour, N., Mohammadi, F., & Safari, H. 2019, The Astrophysical Journal Supplement Series, 243, 20

Ambastha, A., Basu, S., & Antia, H. M. 2003, , 218, 151

Antiochos, S. K. 1998, The Astrophysical Journal Letters, 502, L181

Aparna, V. 2019, Data for Bz Analysis of Halo CMEs between 2007-2017

——. 2021, Filament IMF Bz - Final Dataset

——. 2022, Sigmoid Filament Analysis

Aparna, V., & Martens, P. C. 2020, The Astrophysical Journal, 897, 68

Aparna, V., & Tripathi, D. 2016, The Astrophysical Journal, 819, 71

Archontis, V., Hood, A. W., Savcheva, A., Golub, L., & Deluca, E. 2009, The Astrophysical Journal, 691, 1276

Balch, C. C., Crown, M. D., & Viereck, R. 2004, in American Astronomical Society Meeting Abstracts, Vol. 204, American Astronomical Society Meeting Abstracts #204, 02.19

Barnes, G., Longcope, D. W., & Leka, K. D. 2005, The Astrophysical Journal, 629, 561

Bel, N., & Leroy, B. 1977, Astronomy and Astrophysics, 55, 239

Berger, M. A., & Field, G. B. 1984, Journal of Fluid Mechanics, 147, 133

Bobra, M. G., Sun, X., Hoeksema, J. T., Turmon, M., Liu, Y., Hayashi, K., Barnes, G., & Leka, K. D. 2014, , 289, 3549

Bogdan, T. J. et al. 2003, The Astrophysical Journal, 599, 626

Boteler, D. H. 2019, Space Weather, 17, 1427

Bothmer, V., & Schwenn, R. 1998, Annales Geophysicae, 16, 1

Bourdin, P., Singh, N. K., & Brandenburg, A. 2018, The Astrophysical Journal, 869, 2

Brueckner, G. E. et al. 1995, , 162, 357

Burlaga, L., Sittler, E., Mariani, F., & Schwenn, R. 1981, , 86, 6673

Burlaga, L. F., Skoug, R. M., Smith, C. W., Webb, D. F., Zurbuchen, T. H., & Reinard, A. 2001, , 106, 20957

Burton, R. K., McPherron, R. L., & Russell, C. T. 1975, , 80, 4204

Cally, P. S., & Moradi, H. 2013, Monthly Notices of the Royal Astronomical Society, 435, 2589

Canfield, R. C., Hudson, H. S., & McKenzie, D. E. 1999, , 26, 627

Canfield, R. C., Kazachenko, M. D., Acton, L. W., Mackay, D. H., Son, J., & Freeman, T. L. 2007, The Astrophysical Journal Letters, 671, L81

Carrington, R. C. 1859, Monthly Notices of the Royal Astronomical Society, 20, 13

Chaplin, W. J. et al. 1999, Monthly Notices of the Royal Astronomical Society, 308, 405

Chen, P. F., Harra, L. K., & Fang, C. 2014, The Astrophysical Journal, 784, 50

Cheung, M. C. M., & Isobe, H. 2014, Living Reviews in Solar Physics, 11, 3

Christensen-Dalsgaard, J., Gough, D. O., & Thompson, M. J. 1991, The Astrophysical Journal, 378, 413

Delaboudinière, J. P. et al. 1995, , 162, 291

Donea, A. C., & Lindsey, C. 2005, The Astrophysical Journal, 630, 1168

Doornbos, E., & Klinkrad, H. 2006, Advances in Space Research, 37, 1229

Dungey, J. W. 1962, Journal of the Physical Society of Japan Supplement, 17, 15

Dziembowski, W. A., & Soszyński, I. 2010, Astronomy and Astrophysics, 524, A88

Engvold, O. 1998, in Astronomical Society of the Pacific Conference Series, Vol. 150, IAU Colloq. 167: New Perspectives on Solar Prominences, ed. D. F. Webb, B. Schmieder, & D. M. Rust, 23

Fan, Y. 2017, The Astrophysical Journal, 844, 26

——. 2018, The Astrophysical Journal, 862, 54

Fan, Y., & Gibson, S. E. 2003, The Astrophysical Journal Letters, 589, L105

——. 2004, The Astrophysical Journal, 609, 1123

——. 2007, The Astrophysical Journal, 668, 1232

Finsterle, W., Jefferies, S. M., Cacciani, A., Rapex, P., Giebink, C., Knox, A., & DiMartino, V. 2004a, , 220, 317

Finsterle, W., Jefferies, S. M., Cacciani, A., Rapex, P., & McIntosh, S. W. 2004b, The Astrophysical Journal Letters, 613, L185

Forsyth, R. J., & Marsch, E. 1999, , 89, 7

Garcia, H. A. 1994, , 154, 275

Gary, G. A. 2001, , 203, 71

Georgoulis, M. K. et al. 2021, Journal of Space Weather and Space Climate, 11, 39

Georgoulis, M. K., & LaBonte, B. J. 2007, The Astrophysical Journal, 671, 1034

Georgoulis, M. K., Nindos, A., & Zhang, H. 2019, Philosophical Transactions of the Royal Society of London Series A, 377, 20180094

Georgoulis, M. K., Tziotziou, K., & Raouafi, N.-E. 2012, The Astrophysical Journal, 759, 1

Gibson, S. E. 2018, Living Reviews in Solar Physics, 15, 7

Gibson, S. E., & Fan, Y. 2006, Journal of Geophysical Research (Space Physics), 111, A12103

Gibson, S. E., Fan, Y., Török, T., & Kliem, B. 2006a, , 124, 131

Gibson, S. E., Foster, D., Burkepile, J., de Toma, G., & Stanger, A. 2006b, The Astrophysical Journal, 641, 590

Gizon, L., & Birch, A. C. 2005, Living Reviews in Solar Physics, 2, 6

Glover, A., Ranns, N. D. R., Harra, L. K., & Culhane, J. L. 2000, , 27, 2161

Golub, L. et al. 2007, , 243, 63

Gonzalez, W. D., & Tsurutani, B. T. 1987, , 35, 1101

Gopalswamy, N. 2009, in Climate and Weather of the Sun-Earth System (CAWSES): Selected Papers from the 2007 Kyoto Symposium, 77–120

Gopalswamy, N., Akiyama, S., Yashiro, S., Michalek, G., & Lepping, R. P. 2008, Journal of Atmospheric and Solar-Terrestrial Physics, 70, 245

Gopalswamy, N. et al. 2011, Journal of Atmospheric and Solar-Terrestrial Physics, 73, 658

Gopalswamy, N., Yashiro, S., Michalek, G., Stenborg, G., Vourlidas, A., Freeland, S., & Howard, R. 2009, Earth Moon and Planets, 104, 295

Gosain, S., & Brandenburg, A. 2019, The Astrophysical Journal, 882, 80

Gough, D., & Toomre, J. 1991, , 29, 627

Green, L. M., Kliem, B., Török, T., van Driel-Gesztelyi, L., & Attrill, G. D. R. 2007, , 246, 365

Hapgood, M. A. 1992, , 40, 711

Harvey, J. W. et al. 2011, in AAS/Solar Physics Division Meeting, Vol. 42, AAS/Solar Physics Division Abstracts #42, 17.45

Hazra, S., Sardar, G., & Chowdhury, P. 2020, Astronomy and Astrophysics, 639, A44

Howell, E., & Whalen, D. 2015, Space Policy, 32, 32

Hu, Q., Qiu, J., Dasgupta, B., Khare, A., & Webb, G. M. 2014, The Astrophysical Journal, 793, 53

Huang, Z. W., Cheng, X., Su, Y. N., Liu, T., & Ding, M. D. 2019, The Astrophysical Journal, 887, 130

Inoue, S., Kusano, K., Magara, T., Shiota, D., & Yamamoto, T. T. 2011, The Astrophysical Journal, 738, 161

Jefferies, S. M., Fleck, B., Murphy, N., & Berrilli, F. 2019, The Astrophysical Journal Letters, 884, L8

Jefferies, S. M., McIntosh, S. W., Armstrong, J. D., Bogdan, T. J., Cacciani, A., & Fleck, B. 2006, The Astrophysical Journal Letters, 648, L151

Jefferies, S. M., Osaki, Y., Shibahashi, H., Duvall, T. L., J., Harvey, J. W., & Pomerantz, M. A. 1994, The Astrophysical Journal, 434, 795

Joshi, N. C., Magara, T., & Inoue, S. 2014, The Astrophysical Journal, 795, 4

Kawabata, Y., Iida, Y., Doi, T., Akiyama, S., Yashiro, S., & Shimizu, T. 2018, The Astrophysical Journal, 869, 99

Kay, C., Gopalswamy, N., Xie, H., & Yashiro, S. 2017, , 292, 78

Kayshap, P., Murawski, K., Srivastava, A. K., Musielak, Z. E., & Dwivedi, B. N. 2018, Monthly Notices of the Royal Astronomical Society, 479, 5512

Kazachenko, M. D., Canfield, R. C., Longcope, D. W., Qiu, J., Des Jardins, A., & Nightingale, R. W. 2009, The Astrophysical Journal, 704, 1146

Kilpua, E., Koskinen, H. E. J., & Pulkkinen, T. I. 2017, Living Reviews in Solar Physics, 14, 5

Kippenhahn, R., & Schlüter, A. 1957, , 43, 36

Kliem, B., Titov, V. S., & Török, T. 2004, Astronomy and Astrophysics, 413, L23

Knizhnik, K. J., Antiochos, S. K., & DeVore, C. R. 2017, The Astrophysical Journal, 835, 85

Kosugi, T. et al. 2007, , 243, 3

Krista, L. D., & Chih, M. 2021, The Astrophysical Journal, 922, 218

Kubo, Y., Den, M., & Ishii, M. 2017, Journal of Space Weather and Space Climate, 7, A20

Kuckein, C., Verma, M., & Denker, C. 2016, Astronomy and Astrophysics, 589, A84

Kumar, B., & Ravindra, B. 2006, Journal of Astrophysics and Astronomy, 27, 425

Kumar, P. 1993, in Astronomical Society of the Pacific Conference Series, Vol. 42, GONG 1992. Seismic Investigation of the Sun and Stars, ed. T. M. Brown, 15

Kuperus, M., & Raadu, M. A. 1974, Astronomy and Astrophysics, 31, 189

Kurtz, D. 2022

Kusano, K. 2005, The Astrophysical Journal, 631, 1260

Kusano, K., Maeshiro, T., Yokoyama, T., & Sakurai, T. 2004, The Astrophysical Journal, 610, 537

Kusano, K., Suzuki, Y., & Nishikawa, K. 1995, The Astrophysical Journal, 441, 942

Lam, H. L., Boteler, D. H., Burlton, B., & Evans, J. 2012, Space Weather, 10, S10003

Leighton, R. B., Noyes, R. W., & Simon, G. W. 1962, The Astrophysical Journal, 135, 474

Leka, K. D. et al. 2019, The Astrophysical Journal Supplement Series, 243, 36

Lemen, J. R. et al. 2012, , 275, 17

Lin, Y., Engvold, O., der Voort, L. R. v., Wiik, J. E., & Berger, T. E. 2005, , 226, 239

Linden, T., Zhou, B., Beacom, J. F., Peter, A. H. G., Ng, K. C. Y., & Tang, Q.-W. 2018, , 121, 131103

Liokati, E., Nindos, A., & Liu, Y. 2022, Astronomy and Astrophysics, 662, A6

Litvinenko, Y. E. 2021, Physics, 3, 1046

Liu, L. et al. 2016, The Astrophysical Journal, 826, 119

Liu, R., Liu, C., Wang, S., Deng, N., & Wang, H. 2010, The Astrophysical Journal Letters, 725, L84

Liu, Y., Hoeksema, J. T., & Sun, X. 2014, The Astrophysical Journal Letters, 783, L1

Long, D. M. et al. 2017, , 292, 7

Low, B. C. 1996, , 167, 217

Lugaz, N., & Farrugia, C. J. 2014, , 41, 769

Mackay, D. H., Karpen, J. T., Ballester, J. L., Schmieder, B., & Aulanier, G. 2010, , 151, 333

MacQueen, R. M., Csoeke-Poeckh, A., Hildner, E., House, L., Reynolds, R., Stanger, A., Tepoel, H., & Wagner, W. 1980, , 65, 91

Martens, P. C., Yeates, A. R., & Pillai, K. G. 2014, in Nature of Prominences and their Role in Space Weather, ed. B. Schmieder, J.-M. Malherbe, & S. T. Wu, Vol. 300, 135–138

Martens, P. C. H. et al. 2012, , 275, 79

Martin, S. F. 1998a, , 182, 107

Martin, S. F. 1998b, in Astronomical Society of the Pacific Conference Series, Vol. 150, IAU Colloq. 167: New Perspectives on Solar Prominences, ed. D. F. Webb, B. Schmieder, & D. M. Rust, 419

Martin, S. F. 2015, in Astrophysics and Space Science Library, Vol. 415, Solar Prominences, ed. J.-C. Vial & O. Engvold, 205

Martin, S. F., Bilimoria, R., & Tracadas, P. W. 1994, in NATO Advanced Study Institute (ASI) Series C, Vol. 433, Solar Surface Magnetism, ed. R. J. Rutten & C. J. Schrijver, 303

Martin, S. F., & Echols, C. R. 1994, in NATO Advanced Study Institute (ASI) Series C, Vol. 433, Solar Surface Magnetism, ed. R. J. Rutten & C. J. Schrijver, 339

Martin, S. F., Lin, Y., & Engvold, O. 2008, , 250, 31

Martin, S. F., Panasenco, O., Berger, M. A., Engvold, O., Lin, Y., Pevtsov, A. A., & Srivastava, N. 2012, in Astronomical Society of the Pacific Conference Series, Vol. 463, Second ATST-EAST Meeting: Magnetic Fields from the Photosphere to the Corona., ed. T. R. Rimmele, A. Tritschler, F. Wöger, M. Collados Vera, H. Socas-Navarro, R. Schlichenmaier, M. Carlsson, T. Berger, A. Cadavid, P. R. Gilbert, P. R. Goode, & M. Knölker, 157

Marubashi, K. 1997, Washington DC American Geophysical Union Geophysical Monograph Series, 99, 147

Marubashi, K., Akiyama, S., Yashiro, S., Gopalswamy, N., Cho, K. S., & Park, Y. D. 2015, , 290, 1371

McComas, D. J., Bame, S. J., Barker, P., Feldman, W. C., Phillips, J. L., Riley, P., & Griffee, J. W. 1998, , 86, 563

McIntosh, P. S. 1990, , 125, 251

McIntosh, S. W., & Jefferies, S. M. 2006, The Astrophysical Journal Letters, 647, L77

McKenzie, D. E., & Canfield, R. C. 2008, Astronomy and Astrophysics, 481, L65

Mulay, S. M., Tripathi, D., & Mason, H. 2021, Monthly Notices of the Royal Astronomical Society, 504, 1201

Muller, D. et al. 2009, Computing in Science and Engineering, 11, 38

Müller, D. et al. 2017, Astronomy and Astrophysics, 606, A10

Mundra, K., Aparna, V., & Martens, P. 2021, The Astrophysical Journal Supplement Series, 257, 33

NASA CDAWeb Development Team. 2019, CDAWeb: Coordinated Data Analysis Web, Astrophysics Source Code Library, record ascl:1904.006

Nieves-Chinchilla, T., Jian, L. K., Balmaceda, L., Vourlidas, A., dos Santos, L. F. G., & Szabo, A. 2019, , 294, 89

Nindos, A., & Andrews, M. D. 2004, The Astrophysical Journal Letters, 616, L175

Ouyang, Y., Zhou, Y. H., Chen, P. F., & Fang, C. 2017, The Astrophysical Journal, 835, 94

Palmerio, E. et al. 2018, Space Weather, 16, 442

Pan, H., Gou, T., & Liu, R. 2022, The Astrophysical Journal, 937, 77

Pariat, E., Nindos, A., Démoulin, P., & Berger, M. A. 2006, Astronomy and Astrophysics, 452, 623

Pesnell, W. D., Thompson, B. J., & Chamberlin, P. C. 2012, , 275, 3

Pevtsov, A. A., Berger, M. A., Nindos, A., Norton, A. A., & van Driel-Gesztelyi, L. 2014, , 186, 285

Pizzo, V., Millward, G., Parsons, A., Biesecker, D., Hill, S., & Odstrcil, D. 2011, Space Weather, 9, 03004

Pötzi, W., Veronig, A. M., Riegler, G., Amerstorfer, U., Pock, T., Temmer, M., Polanec, W., & Baumgartner, D. J. 2015, , 290, 951

Priest, E. 2017, Annales Geophysicae, 35, 805

Priest, E. R., Longcope, D. W., & Janvier, M. 2016, , 291, 2017

Rijs, C., Moradi, H., Przybylski, D., & Cally, P. S. 2015, The Astrophysical Journal, 801, 27

Riley, P., Lionello, R., Mikić, Z., & Linker, J. 2008, The Astrophysical Journal, 672, 1221

Riley, P. et al. 2018, Space Weather, 16, 1245

Rosenthal, C. S. et al. 2002, The Astrophysical Journal, 564, 508

Russell, H. N. 1914, Popular Astronomy, 22, 275

Rust, D. M., & Kumar, A. 1994, , 155, 69

——. 1996, The Astrophysical Journal Letters, 464, L199

Savani, N. P. et al. 2015, Space Weather, 13, 374

Savcheva, A. S., McKillop, S. C., McCauley, P. I., Hanson, E. M., & DeLuca, E. E. 2014, , 289, 3297

Scherrer, P. H. et al. 1995, , 162, 129

——. 2012, , 275, 207

Schunker, H., Braun, D. C., Lindsey, C., & Cally, P. S. 2008, , 251, 341

Shetye, J., Doyle, J. G., Scullion, E., Nelson, C. J., Kuridze, D., Henriques, V., Woeger, F., & Ray, T. 2016, Astronomy and Astrophysics, 589, A3

Singh, N. K., Käpylä, M. J., Brandenburg, A., Käpylä, P. J., Lagg, A., & Virtanen, I. 2018, The Astrophysical Journal, 863, 182

Sterling, A. C. 2000, Journal of Atmospheric and Solar-Terrestrial Physics, 62, 1427

Stone, E. C., Frandsen, A. M., Mewaldt, R. A., Christian, E. R., Margolies, D., Ormes, J. F., & Snow, F. 1998, , 86, 1

Temmer, M. 2021, Living Reviews in Solar Physics, 18, 4

Thompson, M. J. 2004, Astronomy and Geophysics, 45, 4.21

Titov, V. S., & Démoulin, P. 1999, Astronomy and Astrophysics, 351, 707

Toriumi, S., & Wang, H. 2019, Living Reviews in Solar Physics, 16, 3

Török, T., & Kliem, B. 2005, The Astrophysical Journal Letters, 630, L97

Török, T., Kliem, B., & Titov, V. S. 2004, Astronomy and Astrophysics, 413, L27

Tripathi, D., Kliem, B., Mason, H. E., Young, P. R., & Green, L. M. 2009, The Astrophysical Journal Letters, 698, L27

Tritschler, A. et al. 2016, Astronomische Nachrichten, 337, 1064

Tziotziou, K., Georgoulis, M. K., & Raouafi, N.-E. 2012, The Astrophysical Journal Letters, 759, L4

Uchida, Y. 1967, The Astrophysical Journal, 147, 181

Ulrich, R. K. 1970, The Astrophysical Journal, 162, 993

Vaiana, G. S., Davis, J. M., Giacconi, R., Krieger, A. S., Silk, J. K., Timothy, A. F., & Zombeck, M. 1973, The Astrophysical Journal Letters, 185, L47

van Ballegooijen, A. A., & Martens, P. C. H. 1989, The Astrophysical Journal, 343, 971

Vasantharaju, N., Vemareddy, P., Ravindra, B., & Doddamani, V. H. 2019, The Astrophysical Journal, 874, 182

Vourlidas, A., Lynch, B. J., Howard, R. A., & Li, Y. 2013, , 284, 179

Wang, S., Jenkins, J. M., Martinez Pillet, V., Beck, C., Long, D. M., Prasad Choudhary, D., Muglach, K., & McAteer, J. 2020, The Astrophysical Journal, 892, 75

Wang, Y., Shen, C., Wang, S., & Ye, P. 2004, , 222, 329

Webb, D. F., & Howard, T. A. 2012, Living Reviews in Solar Physics, 9, 3

Wedemeyer-Böhm, S., Lagg, A., & Nordlund, A. 2009, , 144, 317

Whitman, K. et al. 2022, Advances in Space Research

Wiśniewska, A., Chmielewska, E., Radziszewski, K., Roth, M., & Staiger, J. 2019, The Astrophysical Journal, 886, 32

Wiśniewska, A., Musielak, Z. E., Staiger, J., & Roth, M. 2016, The Astrophysical Journal Letters, 819, L23

Worrall, G. 1991, Monthly Notices of the Royal Astronomical Society, 251, 427

Xu, H., Gao, Y., & Zhang, H. 2009, Science in China: Physics, Mechanics and Astronomy, 52, 1749

Yang, S., Zhang, H., & Büchner, J. 2009, Astronomy and Astrophysics, 502, 333

Yokoyama, T., Kusano, K., Maeshiro, T., & Sakurai, T. 2003, Advances in Space Research, 32, 1949

Yurchyshyn, V. 2008, The Astrophysical Journal Letters, 675, L49

Yurchyshyn, V., Hu, Q., Lepping, R. P., Lynch, B. J., & Krall, J. 2007, Advances in Space Research, 40, 1821

Yurchyshyn, V. B., Wang, H., Goode, P. R., & Deng, Y. 2001, The Astrophysical Journal, 563, 381

Zhou, Z., Liu, R., Cheng, X., Jiang, C., Wang, Y., Liu, L., & Cui, J. 2020, The Astrophysical Journal, 891, 180

Zirker, J. B., Engvold, O., & Martin, S. F. 1998, Nature, 396, 440

Zurbuchen, T. H., & Richardson, I. G. 2006, , 123, 31